Gran Sasso Science Institute
Scuola Internazionale Superiore di Studi Avanzati

Low-mass dark matter and neutrino-less double beta decay searches with the DarkSide technology

PhD thesis

Submitted in date April 25, 2019
Revised in date June 19, 2019

PhD Candidate
Maria Bossa

Advisor: Prof. Cristiano Galbiati

Co-Advisor: Dr. Claudio Savarese

Co-Advisor: Dr. Masayuki Wada

Gran Sasso Science Institute
Ciclo XXIX – A.A. 2013-2016

CONTENTS

LIST OF FIGURES

LIST OF TABLES

I. ABSTRACT

The DarkSide program has delivered the first results on searches for dark matter with a target of ultra-pure low-radioactivity argon from underground sources (UAr) with the DarkSide-50 experiment, in operation at LNGS since 2013. The key element provided by the use of UAr is the strong reduction in activity of ^{39}Ar relative to the atmospheric argon, which avoids the pile-up of events that would otherwise plague any argon-based events at the tonne scale and beyond. Thus the use of UAr enables the construction of very large scale dark matter detectors, able to combine the advantages of the unsegmented design and very strong rejection of electron recoils afforded by the pulse shape discrimination of liquid argon, thus able to probe the entire discovery space at high masses ($>100\,\mathrm{GeV}/c^2$) prior to and through the onset of background from atmospheric neutrinos (the so called "neutrino floor") in absence of any background from instrumental sources.

The DarkSide Collaboration, which launched the DarkSide-50 program at LNGS, morphed to become the "Global Argon Dark Matter Collaboration" (GADMC). The GADMC started a program for the complete exploration of the discovery space of high-mass dark matter consisting of the DarkSide-20k experiment, at the scale of a few tens of tonnes, that is going to be constructed at LNGS and expected in operation by 2023, and Argo, at the scale of a few hundred tonnes, and proposed for installation at SNOLAB.

The full exploitation of the UAr target for high-mass dark matter searches required the development of very special technologies. The GADMC developed special photodetector modules (PDMs) made of assemblies of silicon photomultipliers (SiPMs) and characterized by very high photon detection efficiency, background much lower than traditional photomultiplier tubes (PMTs), and dark noise lower than that of PMTs when operated near a temperature of 87 K. The GADMC also developed a special plan for the high-throughput extraction of UAr at special gas wells in Colorado, USA, with the Urania plant and for its purification in the novel cryogenic distillation column Aria, characterized by the presence of thousands of equilibrium stages and currently under installation in a mine shaft in Sardinia, Italy. The Aria column with its unprecedented height may be able to provide further isotopic depletion in ^{39}Ar of the UAr target.

Exploration of high-mass dark matter is one of the main thrusts for the discovery of new physics beyond the standard model. In this dissertation, I will focus on the possible use of the DarkSide technology to tackle two different but equally crucial problems, which may also lead to new discoveries: the search for low-mass ($<10\,\mathrm{GeV}/c^2$) dark matter and the search for the neutrinoless double beta decay.

II. THEORETICAL OVERVIEW OF DARK MATTER

Astronomical observations indicate the presence of a large amount of invisible matter in our Universe, called for this reason *dark matter*. More than one fifth of the total matter-energy density of the Universe consists of dark matter, which manifests itself mainly via gravitational influence on visible structures such as galaxies and galaxy clusters. The leading hypothesis on its nature is that it is made of particles that may interact weakly with ordinary matter. Many experiments have been built to detect these elusive particles.

In this chapter I will illustrate the astronomical evidence for the existence of dark matter, and will explain its crucial role in the formation of the large-scale structures of the Universe. I will also illustrate the main detection techniques developed for the discovery of dark matter.

II.A. Evidence of Dark Matter

A first evidence of the existence of invisible matter in the Universe was produced in 1933 by Fritz Zwicky, in the course of its study of the Coma and Virgo cluster [1, 2]. Zwicky measured the dispersion velocity of the clusters and found it to be much larger than what warranted by the mass calculated form their luminosity. He concluded that the mass of the clusters must be dominated by a non luminous form of matter.

In the 1970's, Vera Rubin firmly established the need for a dark matter component by measuring the rotation curves of galaxies [3, 4]. Using the virial theorem it is possible to correlate the orbital velocity of the stars as function of their radius in the galaxy with the mass of the galaxy included within the same radius. In regions outside the optical disk, where the mass of the stars goes to zero, the velocity should rapidly decrease as $1/\sqrt{r}$. Rubin's observations instead determined that the rotation curve stayed constant well beyond the limit of the optical disk, as shown in Fig. 1: this suggested the presence of a dark matter halo extending beyond the traditional limit of the galaxy.

Fig. 1 shows the rotation curve for spiral galaxy NGC 3198 from the original measurement of Rubin and Ford of 1970 [3]. Data points with error bars are compared with the curve detailing the expectation from the measurement of the mass of the stars. Also shown are the contribution of the dark matter halo and the curve detailing the expectation from the joint masses of stars and dark matter. The conclusion is that the mass of the visible matter cannot explain the orbital velocity of the stars. It is necessary to add a dark matter halo component to account for a large portion of mass and obtain a good match to the measured orbital velocity.

The rotation curves of galaxies provide one of the most relevant proofs for the existence of dark matter. The role of more recent and relevant cosmological observations will be discussed in the next paragraphs.

II.B. Gravitational Lensing and the Bullet Cluster

Gravitational lensing arises from the presence of a large mass concentration in a region of space-time, deflecting the path of photons and potential modifying the apparent position and shape of astronomical sources in the background. The presence of this effect allows to probe the distribution of large sources of gravitation.

The most spectacular results in support of dark matter come from the observation in various bands of the cluster 1E 0657-558 [5, 7], the so-called *Bullet Cluster*, see Fig. 2. It is composed by two clusters of galaxies that have collided. The dominant mass distribution, reconstructed using gravitational lensing, is found to coincide with the centroid of the luminous galaxies; the dominant baryon distribution, due to hot gas and independently inferred X-ray observation by the Chandra telescope, is in a different position; there is a net shift between the barycenter of the dominant mass distribution and the hot gas distributions. This complex phenomenology can be interpreted by assuming that the original clusters included galaxies, gas clouds, and dark matter and that they were moving towards each other; during the collision, galaxies and stars, expected to act as collisionless particles, were not severely affected and passed right through each other; the hot gas, on the other hand, was slowed down by the collisions between molecules, and separated from the stars and galaxies; the lensing is strongest in two separate regions centered around the centroid of the galaxies, supporting the idea that most of the mass in the cluster is in the form of dark matter, different from the gas that dominates the baryonic matter.

The whole set of observations is in agreement with the hypothesis of dark matter. The Bullet Cluster is short of being a proof of dark matter because the same phenomenology could be obtained under the hypothesis that dark matter in the cluster be made of massive compact halo objects [8, 9].

The recent discovery of cluster MACS J0025.4-1222 further compounds the evidence for dark matter from collision of clusters [10].

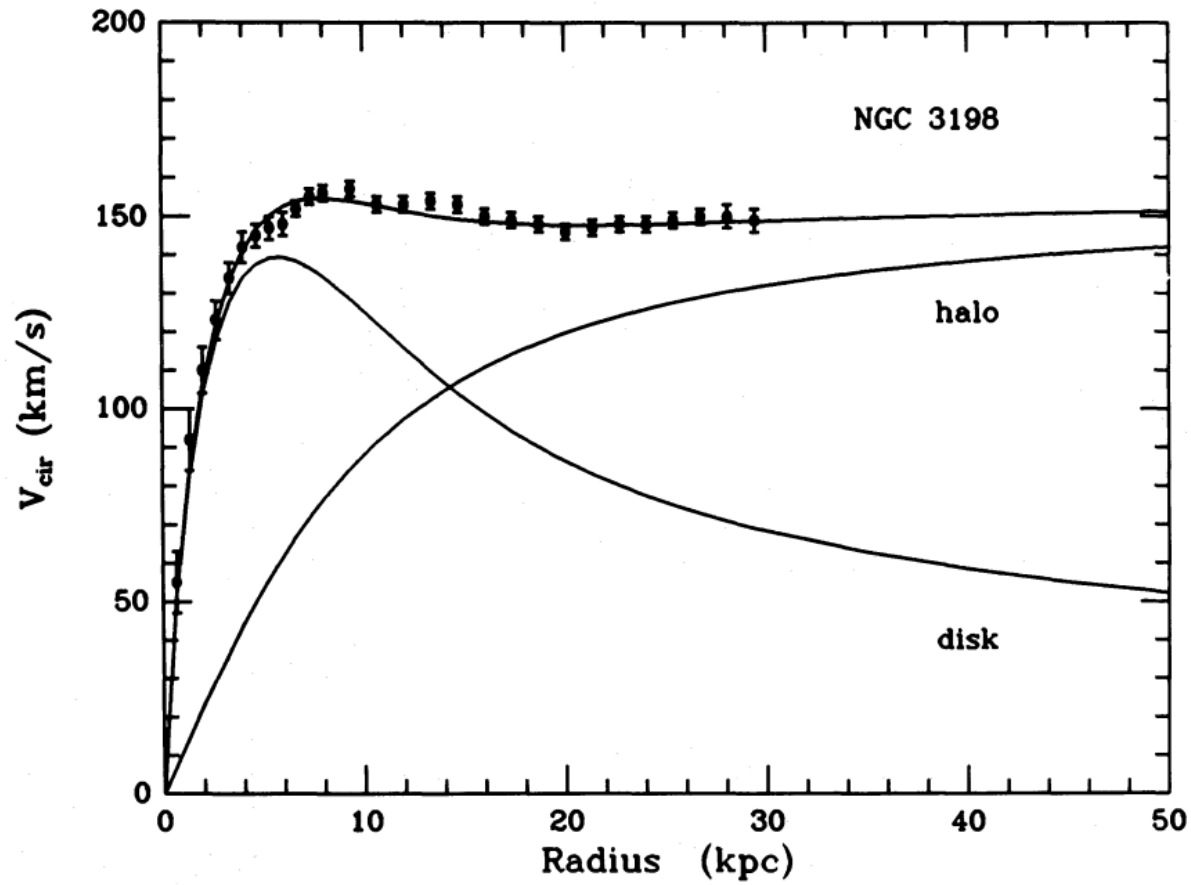

FIG. 1. Rotation curve of spiral galaxy NGC 3198, from the original 1970 measurement of Rubin and Ford [3]. See text for details.

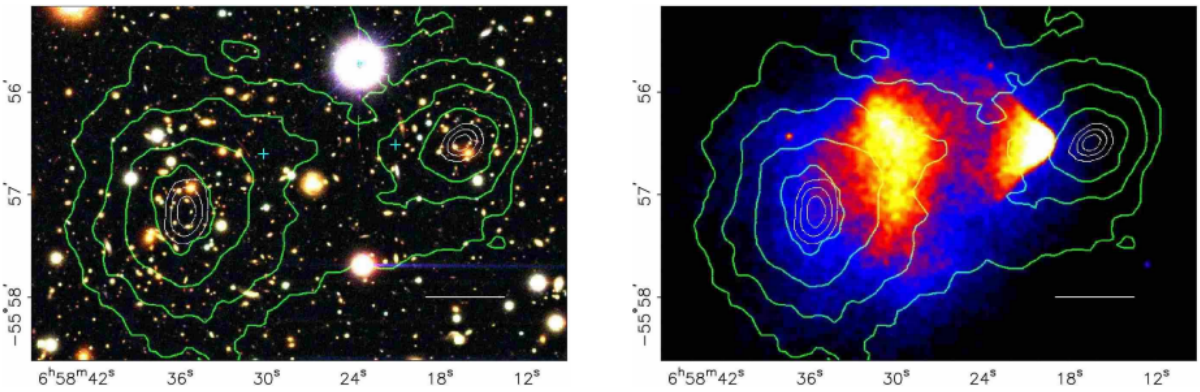

FIG. 2. Left: optical image of the the "Bullet Cluster" (1E 0657-558), from Ref. [5]. The mass distribution was determined with gravitational lensing observations, and it is shown with green contours. Right: image of X-ray light in yellow and red, in blue the gravitational lensing map from the Chandra X-ray mission [6].

II.C. Cosmic Microwave Background

Proofs of the existence of Dark Matter also come from studies of the Cosmic Microwave Background (CMB), an ensemble of non-interacting photons that permeates the entire Universe, predicted by the Big Bang theory and discovered in 1964 [11]. The present CMB temperature is $T_0 = (2.7260 \pm 0.0013)\,\mathrm{K}$ [12].

The temperature of photons coming from different directions on celestial sphere is the same at the level

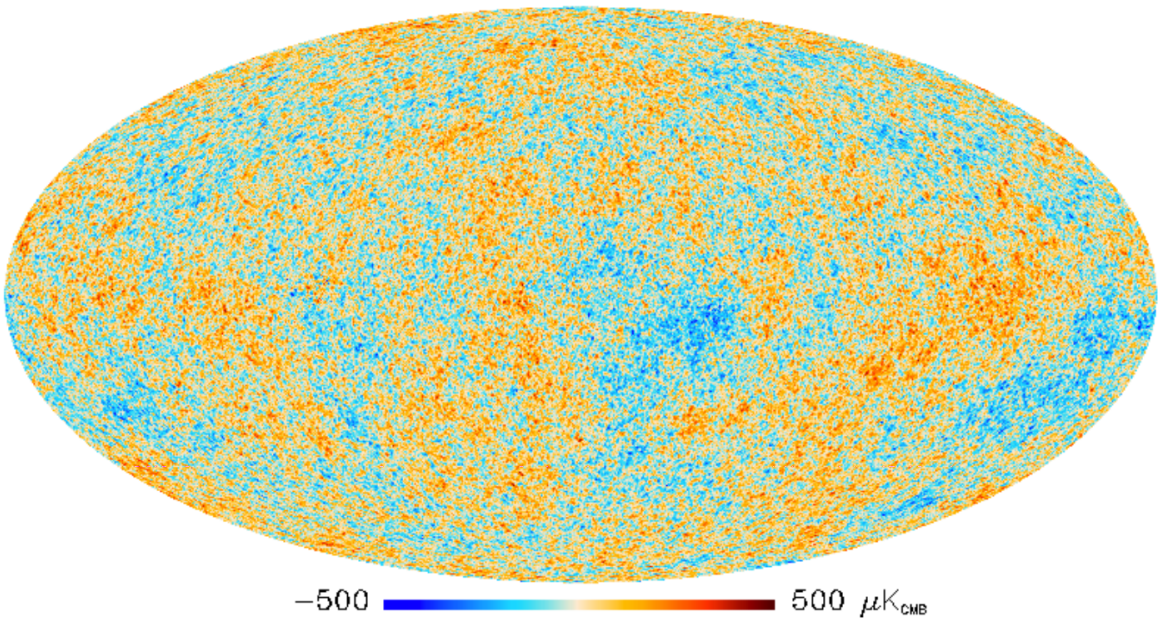

FIG. 3. CMB full sky temperature map highlighting its anisotropy, as measured by the PLANCK satellite [13].

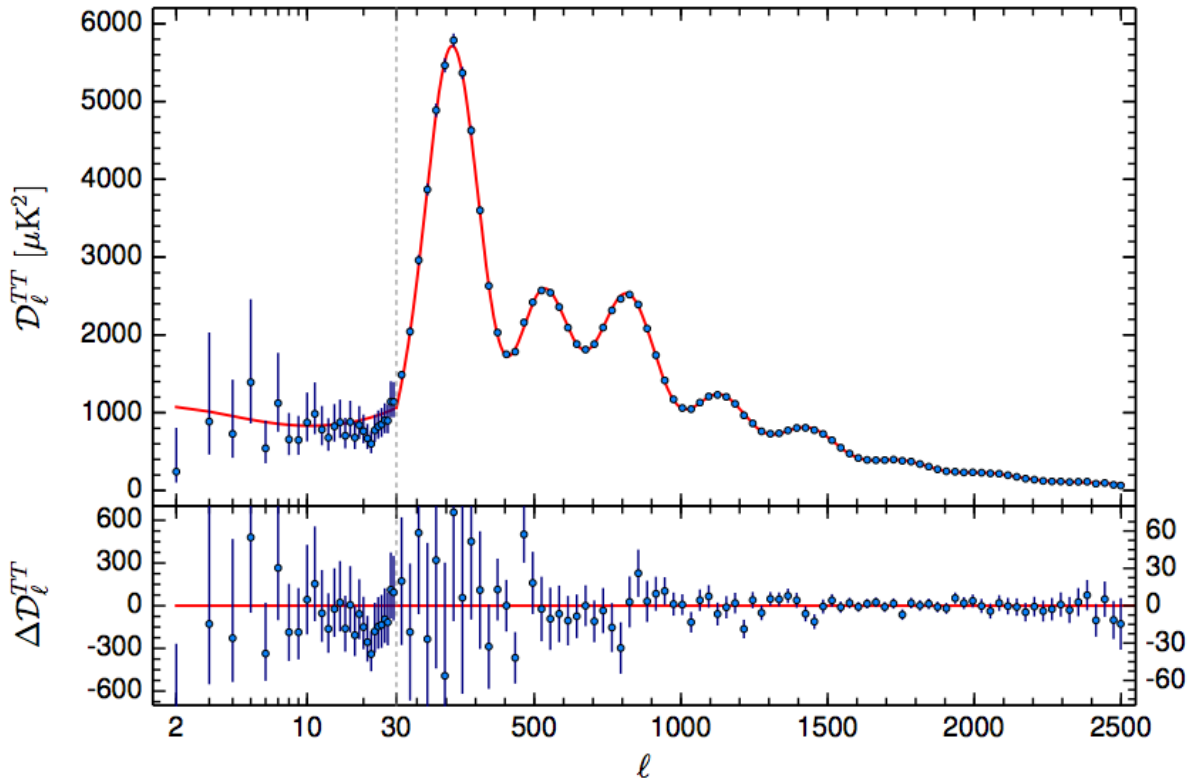

FIG. 4. CMB temperature multipole power spectrum as measured by the PLANCK satellite [13].

of better than 10^{-4}, a testimony to the homogeneity and isotropy of the Universe at large scale; the anisotropies of the CMB temperature encodes a lot of informations about the present and early Universe. These anisotropies has been measured by PLANCK satellite [13], and are shown in Fig. 4.

The variations in the CMB temperature maps are interpreted as the result of perturbations in the density of the early Universe: the shape of the power spectrum is determined by oscillations in the hot gas of the early Universe, the resonant frequencies and amplitudes of these oscillations are determined by its composition: figure Fig. 5 represents the different heights of the peaks obtained by varying the abundance of baryonic matter and of cold dark matter at the epoch of the last scattering of CMB photons. In Fig. 5, the abundance of the species are defined by the dimensionless density parameters $\Omega_i = \rho_i/\rho_c$, where ρ_c is the critical density. By studying the positions and relative sizes of these peaks we can infer information on the curvature of the Universe, and hence how much total matter there is in it, and how much of the matter is baryonic (ordinary matter). The informations extracted by the CMB are reported in Table I.

The result on the abundance of baryonic matter obtained from the study of the CMB spectrum can be compared with the abundances of baryonic matter obtained by the theory of Big Bang nucleosynthesis, which provides further incontrovertible evidence that baryonic matter constitutes about 4 % of the Universe. A brief description of the Big Bang nucleosynthesis is given below.

II.D. Big Bang Nucleosynthesis

The abundance of baryonic matter in the Universe can be understood by the process that led to the formation of light nuclei, the big bang nucleosynthesis. In the following discussions I will adopt the convention $k_B = c = 1$. Until 1 s after the Big Bang at $T \gg 1\,\text{MeV}$ photons, electrons and positrons are in equilibrium, neutrinos are about to decouple. Baryons are non-relativistic and therefore much fewer in number than the relativistic species. The total number of nucleons stays constant due to baryon number conservation. This baryon number can be in the form of protons and neutrons or heavier nuclei. Weak nuclear reactions may convert neutrons and protons into each other and strong nuclear reactions may build nuclei with them.

The neutron-to-proton ratio is:

$$\left(\frac{n_n}{n_p}\right)_{eq} = \left(\frac{m_n}{m_p}\right)^{3/2} e^{-(m_n - m_p)/T}. \tag{1}$$

The small difference between the proton and neutron mass can be ignored in the first factor, but crucially has to be kept in the exponential. Hence:

$$\left(\frac{n_n}{n_p}\right)_{eq} e^{-Q/T}, \tag{2}$$

where $Q \equiv m_n - m_p = 1.30\,\text{MeV}$. For $T \gg 1\,\text{MeV}$, there are therefore as many neutrons as protons. However, for $T < 1\,\text{MeV}$, the neutron fraction gets smaller. The primordial ratio of neutrons to protons is of particular importance to the outcome of BBN, since essentially all the neutrons become incorporated into ^{4}He; weak interactions keep neutrons and protons in equilibrium until $T \sim 1\,\text{MeV}$.

Neutrons follow this abundance until neutrinos decouple at $T_f \sim T_{\text{dec}} \sim 0.8\,\text{MeV}$, hence $(n_n/n_p)_{T_{\text{dec}}} = e^{-Q/T_{\text{dec}}} \sim \frac{1}{6}$.

At this point, the Universe is mostly protons and neutrons, the first nucleus to form is therefore deuterium:

$$p + n \leftrightarrow D + \gamma. \tag{3}$$

Only when deuterium is available helium can be formed,

$$D + p \leftrightarrow {}^3\text{He} + \gamma, \tag{4}$$

$$D + {}^3\text{He} \leftrightarrow {}^4\text{He} + p. \tag{5}$$

TABLE I. Leading cosmological parameters from the PLANCK primary CMB data, restricting polarization data to low multipoles, and from the PLANCK [13].

Costant	Symbol	Value
Baryon Density	$\Omega_b h^2$	$0.022\,26 \pm 0.000\,23$
Cold Dark Matter Density	$\Omega_c h^2$	0.1186 ± 0.0020
Dark Energy Density	$\Omega_\Lambda h^2$	0.318 ± 0.012
Total Mass-Energy Density	Ω	1.002 ± 0.011
Scale Factor	h	0.678 ± 0.009

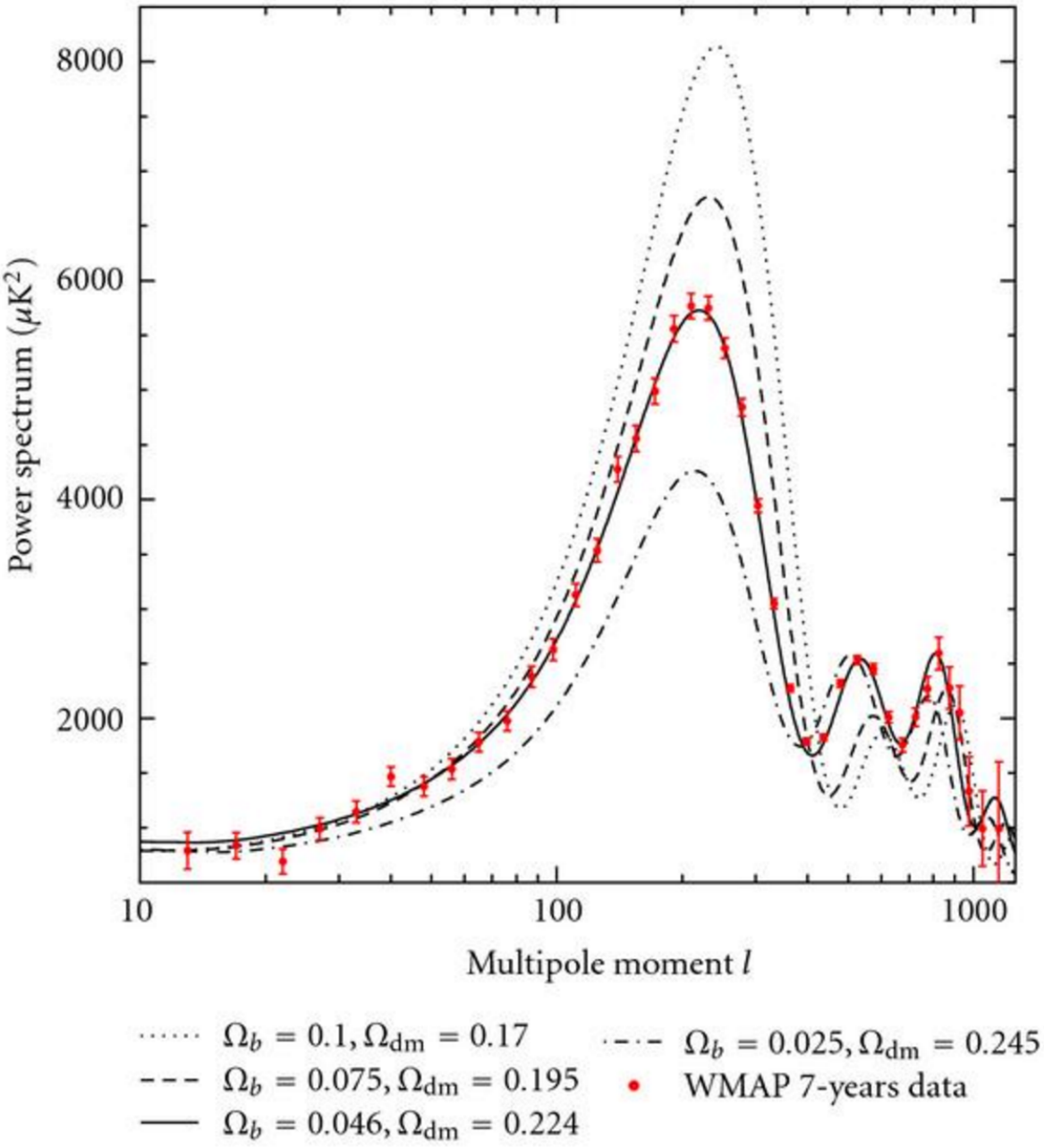

FIG. 5. CMB multipole power spectrum for various values of Ω_b and Ω_c, see Ref. [14].

Since deuterium is formed directly from neutrons and protons it can follow its equilibrium abundance as long as enough free neutrons are available. However, since the deuterium binding energy is rather small, the deuterium abundance becomes large rather late (at $T < 100\,\mathrm{keV}$). So although heavier nuclei have larger binding energies and hence would have larger equilibrium abundances, they cannot be formed until sufficient deuterium has become available.

$$\frac{n_{He}}{n_H} = \frac{n_{He}}{n_p} \sim \frac{1}{16}. \tag{6}$$

This prediction is consistent with the observed helium in the Universe, see Fig. 6.

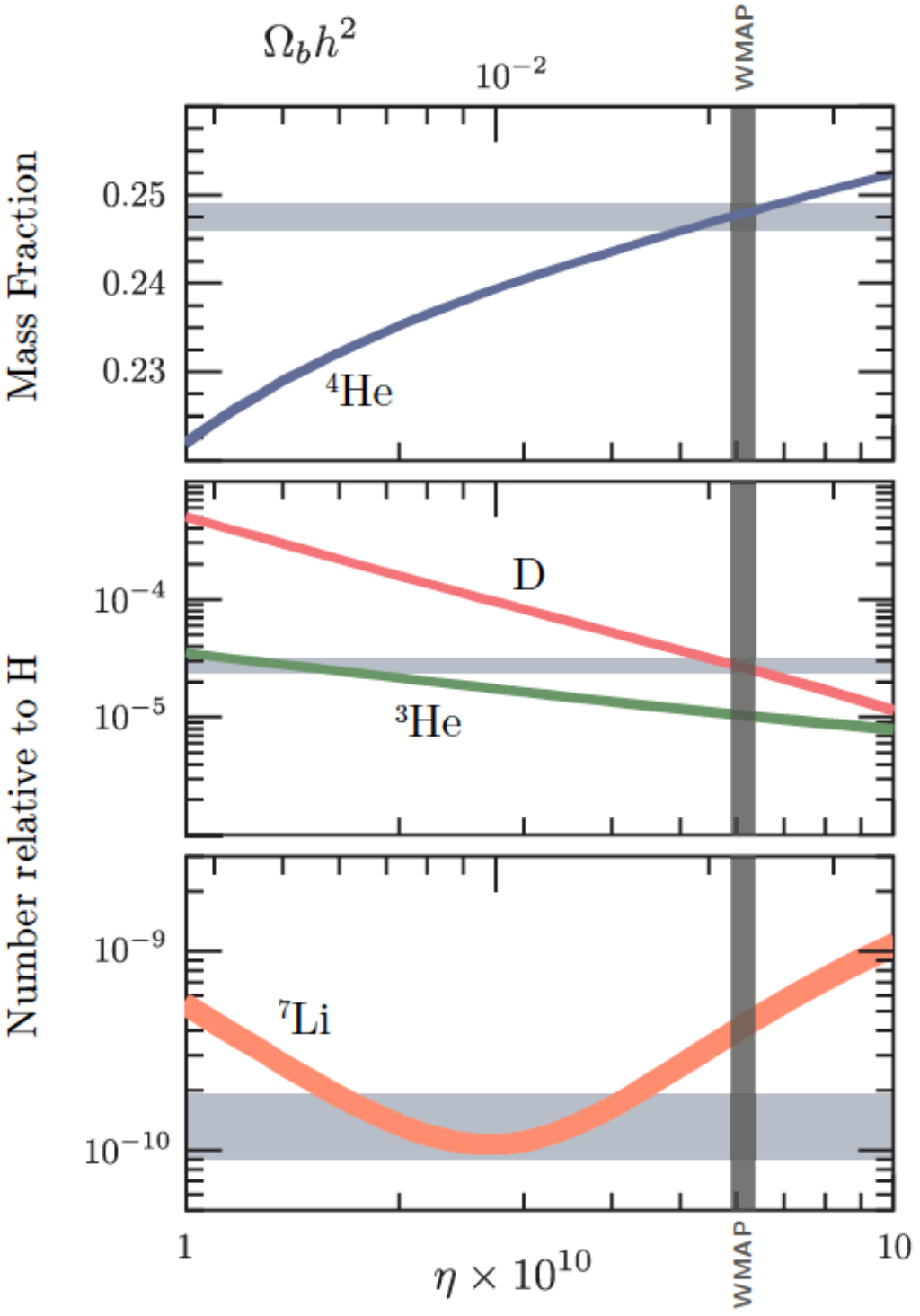

FIG. 6. Light elemental abundances from Big Bang Nucleosynthesis as a function of baryon density. The colored bands represent theoretical predictions. The vertical band is the baryon density from CMB measurements. The grey bands are from observational constraints. The variable η on x-axis represents the baryon-to-photon ratio.

II.E. Dark Matter Candidates

The idea of primordial nucleosynthesis suggests that the amount of baryonic matter is larger than the visible one, so we can assume that part of the galactic halos consists of baryonic matter. But the experimental result on the amount of luminous matter, $\Omega_{\rm lum} < 0.007$, suggests that this matter cannot exist in form of luminous stars. These arguments only leave room for special stellar objects of baryonic matter, called Massive Compact Halo Objects (MACHOs), that include celestial objects which just did not manage to initiate hydrogen burning, neutron stars, black holes and dwarf stars. However, the hypothetical amounts of these objects is not able to account for the dark matter amount, therefore one conclude that the missing matter in the Universe has non baryonic origin. Detailed numerical simulations of the structure formation process provide strong indications that the non baryonic dark matter is in form of a gas of cold (*i.e.*, non relativistic), massive particles. The standard model (SM) of particle does not provide such a candidate; one could think about neutrinos but still they can't be a reasonable dark matter candidate for reasons which I will explain soon.

Let us consider a stable massive neutrino: if its mass is less than $10^{-4}\,\mathrm{eV}/c^2$, it should be still relativistic today and its contribution to Ω_b should be negligible; in the opposite case, it is non relativistic and its contribution to the energy density of the Universe is simply given by its number density times its mass. One can demonstrate that with a neutrino mass in the range of $1\,\mathrm{eV}/c^2$ to $20\,\mathrm{eV}/c^2$, one can have a significant mass contribution of interest for the dark matter problem. However the data on neutrino oscillations suggest neutrino masses smaller than $1\,\mathrm{eV}/c^2$.

Theories beyond the Standard Model, which have been developed specifically to solve problems inherent to elementary particle physics, comprise very attractive dark matter candidates; the most popular candidates for WIMPs come from the supersymmetric and extra-dimensional theories. In particular, for the supersymmetric theories, among the Dark Matter candidates, two candidates have been widely studied for the last two decades the neutralino and the gravitino.

II.F. Dark Matter Relics

The most attractive Dark Matter candidates are WIMPs (Weakly Interacting Massive Particles) with a mass of order $M_\chi \sim 100\,\mathrm{GeV}/c^2$. In order to estimate the relic abundance of WIMPs in the Universe a calculation of the epoch of their freeze-out is required. In the early Universe, at temperature $T \gg M_X$, WIMPs are in thermal equilibrium and are nearly abundant as lighter particles, like photons, quarks and leptons. When the temperature falls below the WIMP mass, however, the WIMP abundance becomes Boltzmann-suppressed, and WIMPs can no longer find each other to annihilate. The remaining WIMPs constitute a primordial relic population that still exists today. The mechanism is detailed in Fig. 7.

Let's assume that WIMPs are Majorana particles. Their annihilation rate is:

$$\Gamma(XX \leftrightarrow q\bar{q}, \ell\bar{\ell}, \dots) = n_X \overline{\sigma v}, \tag{7}$$

where $\bar{\sigma}$ is the average cross section for annihilation of two WIMPs to all lighter Standard Model particles, and $\bar{v}$ is their average relative velocity. The expansion rate of the Universe is $H = (8\pi G\rho/3)^{1/2} \sim T^2/M_{\rm pl}$ during the radiation era, where $\rho \propto T^4$. Comparing these two rates, one can identify two different regimes:

- At early times, when $T \gg M_X, n_X \propto T^3$ and $\Gamma \gg H$, particles scatter and annihilate many times during an Hubble time, and this maintains chemical equilibrium;
- At later times, when $T \ll M_X, n_X \propto T^{3/2} e^{-M_X/T}$ and $\Gamma \ll H$, there can be no annihilations, and WIMPs freeze out fixing their abundance (the comoving number density becomes constant from there on).

This sequence of events is illustrated in Fig. 7 showing the number density of WIMPs as a function of the inverse temperature in equilibrium (solid curve) and including freeze-out (dashed curves). Freeze-out occurs when $\Gamma(T_f) \backsim H(T_f)$. For non relativistic particles, $n_X = g_X (M_X T/2\pi)^{3/2} e^{-M_X/T}$,where g_X is the number of degrees of freedom, so the freeze out condition becomes:

$$(M_X T_f)^{3/2}\, e^{-M_X/T_f} \overline{\sigma v} \sim \frac{T_f^2}{M_{\rm Pl}} \Rightarrow \frac{T_f}{M_\chi} \sim \ln\left(\frac{M_{\rm Pl} M_\chi^{3/2} \overline{\sigma v}}{\sqrt{T_f}}\right)^{-1}, \tag{8}$$

and taking $\overline{\sigma v} \backsim \alpha^2/M_X^2$ and taking as a first guess $T_f \sim M_X$ we find:

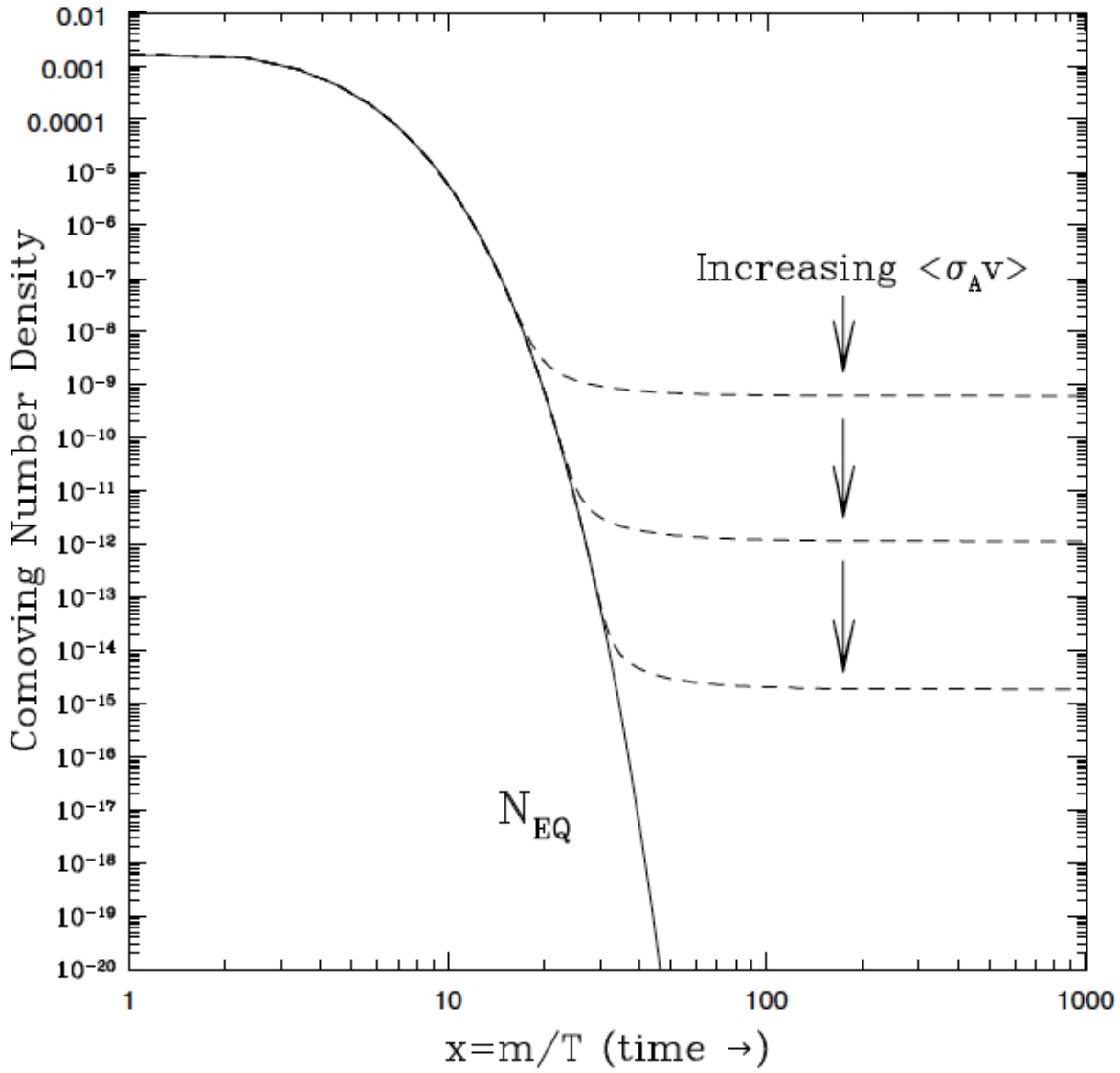

FIG. 7. Thermal history of equilibrium (solid curve) and relic abundance (dashed curves) of WIMP particles, highlighting the dark matter freeze-out mechanism.

$$\frac{T_f}{M_X} \sim \left[\ln\left(\frac{M_{\rm Pl}\alpha^2}{(M_X T_f)^{1/2}}\right)\right]^{-1} \sim \left[\ln\left(\frac{10^{19}10^{-4}}{100}\right)\right]^{-1} \sim \frac{1}{25} + \text{ log corrections}, \tag{9}$$

where the numerical values are characteristic electroweak-scale parameters (i.e $\sigma \backsim 10^{-8}/\mathrm{GeV}^2, M_X \backsim 100\,\mathrm{GeV}/c^2$).

At freeze out, the abundance relative to photons is:

$$\frac{n_\chi}{n_\gamma} = \frac{\Gamma(T_f)}{\overline{\sigma v} T_f^3} = \frac{H(T_f)}{\overline{\sigma v} T_f^3} \sim \frac{T_f^2}{M_{\rm Pl}\overline{\sigma v} T_f^3} \tag{10}$$

$$\sim \frac{1}{M_{\rm Pl}\overline{\sigma v} T_f} \sim \frac{25}{M_{\rm Pl}\overline{\sigma v} M_\chi}. \tag{11}$$

Then:

$$\Omega_X = \frac{\rho_X}{\rho_c} \sim \frac{n_X}{n_\gamma}\frac{M_X n_\gamma}{\rho_c} \sim \frac{25}{M_{\rm Pl}\overline{\sigma v}}\frac{400/\mathrm{cm}^3}{10^{-6}\,\mathrm{GeV/cm}^3}, \tag{12}$$

with no explicit dependence on the particle mass. We thus obtain the observed abundance $\Omega_X h^2 \backsim 0.1$ for $\sigma \backsim 10^4(0.1\times 10^{19}\times 10^{-6})^{-1}1/\mathrm{GeV}^2 \sim 10^{-8}/\mathrm{GeV}^2$, which turns out to be nearly exact. A more precise calculation (including all the dropped factors) gives:

$$\Omega_X h^2 \sim \left(\frac{3\times 10^{-26}\,\mathrm{cm}^3/\,\mathrm{sec}}{\overline{\sigma v}}\right) + \text{ log corrections.} \tag{13}$$

The fact that a thermal relic with a cross section characteristic of the weak interaction gives the right dark matter abundance is called the "WIMP Miracle". Having estimated the abundance of WIMPs in the Universe, we can proceed with the explanation of the basic methods for their detection.

II.G. Dark Matter Detection

Two basic methods can be used to detect Dark Matter, either direct or indirect. Direct searches are based on the detection of Dark Matter particles passing through detectors and physically interacting with them; indirect searches look for secondary products originated by Dark Matter particles annihilation typically in the Galaxy. The two methods, being very different, are complementary.

As for the indirect detection techniques they are based on self-annihilation processes of WIMPs that is proportional to the square of the particle density; so the most obvious annihilation source is the centre of the Galaxy, where the Dark Matter density is expected to rise substantially.

The clearest signatures for a detection would be single energy lines in γ-ray, neutrino or charged lepton cosmic ray spectra, which would give unambiguous information about the WIMP mass as well. However, γ-ray lines are suppressed in all models considered here, making them a weak signal. The great advantage in searching for Dark Matter through annihilation to γ-rays is that this channel retains the information of the source location, in contrast to charged cosmic rays that are diffused by the galactic magnetic turbulence. The experiments performing Dark Matter searches with γ-rays are space-based for low energies ($\sim$ MeV) and ground-based for high energies (tens to hundreds GeV). Of course, even in this case, the signal has to be disantangled from a background represented by a continuum in the energy spectrum.

The main γ-ray production mechanism that contributes to this diffuse flux, at energies from 100 MeV to tens of GeV's, is the interaction of charged cosmic rays with the interstellar matter, which produces π^0 that decays via $\pi^0 \to \gamma\gamma$. Other sources are the inverse Compton scattering of cosmic ray electrons off the interstellar photons and the electron bremsstrahlung in the interstellar medium.

Another way to search Dark Matter consists in the detection of rare species of particles in the cosmic-ray extra-atmospheric flux, generally antimatter components, which are not expected to be involved in the cosmic acceleration mechanisms. Of course, secondary interactions take place during the propagation of the primary cosmic rays and generate antiparticles.

The second class of detection techniques, the direct search, is based on the hypothesis that a WIMPDM particle can scatter off normal matter via weak interactions, producing nuclear (or electron) recoils that are then detected via ionization, scintillation or phonons, or combinations of two of these processes. The basic idea lies on the differential energy spectrum of such nuclear recoils, given by:

$$\frac{dR}{dE_R} = \frac{R_0}{E_0 r}e^{-E_R/E_0 r}, \tag{14}$$

where E_R is the recoil energy, E_0 is the most probable incident kinetic energy of a Dark Matter particle of mass M_D, r is the kinematic factor, R is the event rate per unit mass, and R_0 the total event rate. The kinematics for a target nucleus of mass M_T, is expressed by the following equation:

$$r = \frac{4M_D M_T}{(M_D + M_T)^2}. \tag{15}$$

Since galactic velocities are of order $10^{-3}\,c$ and the mass of a WIMP particle is of the order of $10\,\mathrm{GeV}/c^2$ to $1000\,\mathrm{GeV}/c^2$, the recoil energies, rising from the interaction of a WIMP within a detector, lie in the range

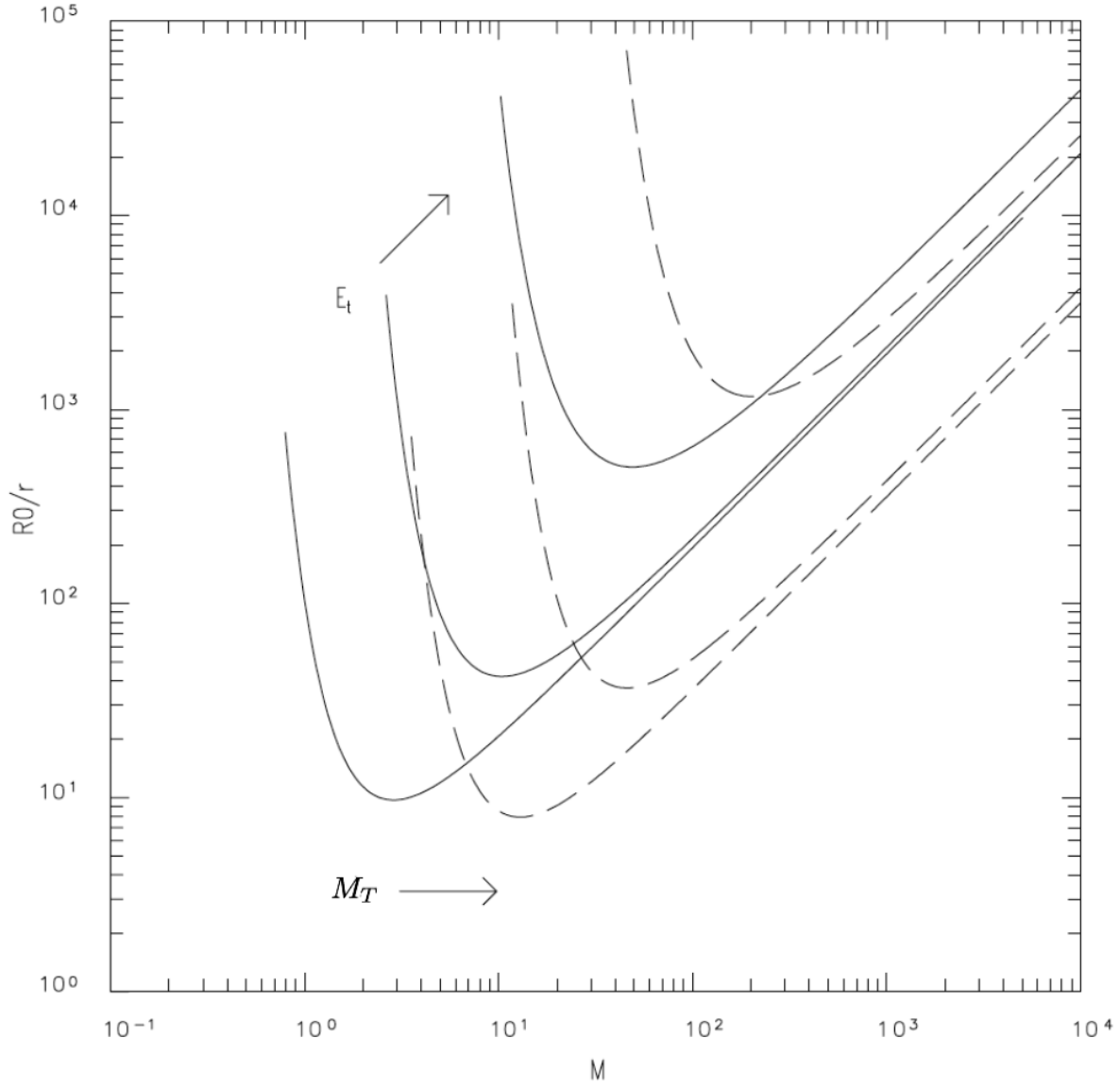

FIG. 8. Typical shape of limit curves: continuous lines for small M_T, and dashed lines for large M_T. Each curve is drawn three times, from left to right, in correspondence of three increasing values of instrumental energy threshold E_t. (Credit: Ref. [15].)

1 keV to 100 keV. Considering Eq. (14), when an experiment has set an upper limit to the differential rate at any particular value of E_R, this implies a corresponding limit for R_0, the WIMP dark matter signal, to be calculated for each assumed value of particle mass M_D. Since the galactic dark matter density and flux are approximately known, the limit on R_0 can be converted into a limit on the particle interaction strength or cross-section. The typical shape of these limits, and their variation with the target mass M_T and instrumental energy threshold is illustrated in Fig. 8.

Taking into account the nuclear interactions of a WIMP with nuclei of the target, the WIMP's velocity distribution and density in the galactic halo, Eq. (14) becomes:

$$\frac{dR}{dE_R} = N_N \frac{\rho_0}{M_D} \int_{v_{\min}}^{v_{\max}} d\mathbf{v} f(\mathbf{v}) v \frac{d\sigma}{dE_R} \tag{16}$$

where N_N is the number of nuclei target, ρ_0 is the WIMP halo density, $\mathbf{v}$ is the WIMP velocity in Earth's reference frame, f($\mathbf{v}$) is the WIMP velocity distribution, $v_{\min}$ is the Dark Matter particle velocity

corresponding to $E_{\min} = E_R/r$, *i.e.* the smallest particle energy which can give a recoil energy of E_R, $v_{\max}$ is the escape velocity of WIMPs in the galaxy. The simplest galactic model assumes a Maxwell-Boltzman distribution for the WIMP velocity in the galactic rest frame, with a velocity dispersion of $\sigma_v \approx 270\,\mathrm{km/s}$ and an escape velocity of $v_{\mathrm{escape}} \approx 544\,\mathrm{km/s}$. Assuming a local Dark Matter density of $\rho_{\mathrm{dm}} = 0.3\,\mathrm{GeV}/(c^2\,\mathrm{cm}^3)$, the number density of WIMPs is $n_0 = \rho_{\mathrm{dm}}/M_D$, and their flux on Earth will be:

$$\Phi_0 = n_0 \times \overline{v} = \frac{\rho_{\mathrm{dm}}}{M_D} = 6.6 \times 10^4\,\mathrm{cm}^2/\mathrm{s}. \tag{17}$$

Taking $\sigma_{\mathrm{DN}} \approx 10^{-38}\,\mathrm{cm}^2$, we obtain a rate for elastic scattering:

$$R \sim N_N \times \Phi_0 \times \sigma_{\mathrm{WD}} = \frac{N_A}{A} \times \frac{\rho_0}{M_D} \times \overline{v} \times \sigma_{\mathrm{WD}} \sim 0.13\,\mathrm{events}/(\mathrm{kg\,yr}) \tag{18}$$

with N_A the Avogadro number and A the atomic mass of the target nucleus. So far we have assumed a WIMP with spin 0, but in the case of a WIMP with spin 1/2 or spin 1 the cross section has to be expressed as the sum of the spin-independent (SI) and spin-dependent (SD) terms:

$$\frac{d\sigma_{\mathrm{DN}}}{dE_R} = \frac{m_N}{2m_r^2 v^2}[\sigma_{\mathrm{SI}} F_{\mathrm{SI}}^2(E_R) + \sigma_{\mathrm{SD}} F_{\mathrm{SD}}^2(E_R)], \tag{19}$$

where σ_{SI} and σ_{SD} are the cross sections in the zero momentum transfer limits (i.e the momentum transfer $q = (2M_T E_R)^{1/2}$ is such that the wavelength h/q is no longer large compared to the nuclear radius), F_{SI} and F_{SD} are the nuclear form factors, which depend on the recoil energy, and:

$$\sigma_{\mathrm{SI}} = \frac{4m_r^2}{\pi}[Z f_p + (A - Z) f_n]^2, \tag{20}$$

$$\sigma_{\mathrm{SD}} = \frac{32 m_r^2}{\pi} G_F^2 \frac{J+1}{J}[a_p \langle S_p + \rangle + a_n \langle S_n \rangle]^2, \tag{21}$$

with f_p, f_n and a_p, a_n being the effective WIMP-couplings to neutron and protons in the spin-independent and spin-dependent case, respectively. The nuclear form factor for the coherent interaction is taken as the Fourier transform of the nucleon density and is parameterized as a function of momentum transfer p:

$$F_{SI}^2(p) = \left(\frac{3 j_1(pR_1)}{pR_1}\right) e^{-p^2 s^2}, \tag{22}$$

where j_1 is a spherical Bessel function, $s \backsim 1\,\mathrm{fm}$ is a measure of the nuclear skin thickness, and $R_1 = \sqrt{R^2 - 5s^2}$ with $R \backsim A^{1/3} \times 1.25\,\mathrm{fm}$. At zero momentum transfer, the nuclear form factor is normalized to unity, $F(0) = 1$. In the spin-dependent case, the form factor is defined as:

$$F_{SD}^2(p) = \frac{S(p)}{S(0)}, \tag{23}$$

with $S(p)$ being the spin structure functions.

Cryogenic bolometric experiments can operate with a very low energy threshold (<10 keV) and an excellent energy resolution (<1 % at 10 keV) [16]. The principle on which these experiments are based on is T^3-dependence of the heat capacity of a dielectric crystal, implying that at low temperatures a small energy deposition can significantly change the temperature of the absorber. The low energy thresholds and excellent resolutions of these detectors made them the clear channel for initiating the first set of dark matter searches: bolometers dominated dark matter searches through the end of the 1990's.

Liquid noble elements such as argon and xenon are good scintillators and ionizers in response to the passage of radiation, the simultaneous detection of ionization and scintillation signals allows to identify the primary particle interacting in the liquid. In addition, the 3D position of an interaction can be determined with sub-mm (in the z coordinate) to mm (in the x-y coordinates) precisions in a time projection chamber (TPC). These features, together with the relative ease of scale-up to large masses have contributed to make liquid xenon (LXe) and liquid argon (LAr) powerful targets for WIMP searches. The rapid development of cryogenic light detectors allowed noble liquid detectors to overtake the sensitivity of bolometers starting from 2006-7 [17, 18].

III. THEORETICAL OVERVIEW OF NEUTRINO-LESS DOUBLE BETA DECAY

Neutrino physics is a very interesting physics since it opens the road to new physics beyond Standard Model. In this chapter first I will retrace briefly the history of the neutrino, starting from its hypothesis to its first detection. After that I will give a short introduction on the neutrino-less double beta decay theory and the importance that it covers.

III.A. The massive neutrino

In 1914 Chadwick observed that the electrons emitted in such decays have a continuous spectrum unlike it happens in α and γ decays, where energy conservation imply a monochromatic electron spectrum since the final state occurs with only two particles [19].

The existence of neutrino was postulated by Pauli in 1930 to remedy to the apparently violation of energy conservation of radioactive β decays [20]. Pauli hypothesized the presence of a new particle, called neutron, with a mass of the same order of magnitude of electrons and a cross section equal or bigger than that of a γ-ray: this hypothesis built upon the idea that particles emitted in decays were bounded in the parent nucleus (as it happens in α decays).

Only in the 1934 Fermi modeled a theory in which the neutrino results from the β decay [21]. The new particle was re-named neutrino after Chadwick identified the real neutrons [22, 23]. The first detection of neutrinos was performed by Cowan and Reines in 1956 in a nuclear reactor experiment [24]. The discovery that neutrinos are left-handed dates to 1958 [25].

Thenceforth many experiments were been conducted to throw light on neutrino's nature: the first evidence for a neutrino anomaly was done by Davis who, since 1968, measured a ν_e solar rate [26] smaller than the predicted one by Bahcall [27]. Up to only a few years ago, it was not clear if there was a solar neutrino problem or a neutrino solar problem. In those years Pontecorvo advanced the hypothesis that neutrinos could oscillate, that is change their flavor [28]. Only in 2002 the SNO solar experiment found evidence for $\nu_{\mu\tau}$ appearance in solar neutrino oscillations [29], while the KamLAND experiment confirmed the anomaly by discovering the disappearance of $\bar{\nu}_e$ from nuclear reactors [30].

In the meantime, the study of atmospheric neutrinos, originally of interest as background for proton decay searches, also provided interesting results. In 1998 the SuperKamiokande experiment established the presence of oscillations for atmospheric neutrinos [31], confirmed around 2004 by the K2K experiment, the first long base-line neutrino beam experiment [32].

The fact that the neutrinos can oscillate is a consequence of their masses and this calls for a physics beyond the Standard Model (SM). The motivation of this statement will be clear soon. The Standard Model of particle physics is a quantum field theory describing the electromagnetic, weak and strong nuclear interactions of elementary particles characterized by the gauge symmetry $SU(3)_C \otimes SU(2)_L \otimes U(1)_Y$. In this scenario fermions are described as:

$$Q_{fL} = \begin{pmatrix} u_{fL} \\ d_{fL} \end{pmatrix} , u_{fR} , d_{fR} \tag{24}$$

$$L_{fL} = \begin{pmatrix} \nu_{fL} \\ l_{fL} \end{pmatrix} , l_{fR}. \tag{25}$$

where the index L states for the three quark and lepton families. In particular the three left-handed neutrino fields are νeL, $\nu \mu L$ and $\nu \tau L$, which transform in the corresponding left-handed charged lepton l_L under the $SU(2)_L$ group; while the right-handed charged leptons l_R are singlets under $SU(2)_L$ and right-handed neutrinos don't exist in the Standard Model. As for leptons and quarks masses they are generated by the spontaneous breaking of symmetry group $SU(2)_L \otimes U(1)_Y$ through Higgs mechanism. The Yukawa interaction between fermions and the Higgs field $\Phi = \frac{1}{\sqrt{2}}\binom{\Phi^+}{\Phi^0}$ is a gauge invariant term in the Lagrangian. When the electroweak symmetry is spontaneously broken and the Higgs acquires a vacuum expectation value $\langle 0|\Phi|0\rangle = \frac{1}{\sqrt{2}}\binom{0}{v}$ the Yukawa interaction generates a mass term for the charged leptons of the form $\lambda \nu \bar{l_L} l_R$, called Dirac mass term, that involves both left-handed and right-handed fields. Every massive fermion in the Standard Model acquires its mass from such a Dirac mass term. The absence of right-handed neutrinos implies that neutrinos are massless in the Standard Model: the Yukawa interactions that would give rise to neutrino masses do not exist. But, as we have seen, experimental results show that neutrinos are not massless; to take into account this fact one can introduce neutrino masses into the theory adding right-handed neutrinos to the Standard Model by analogy with the charged leptons or quarks. So, neutrino masses would be generated by the usual Higgs mechanism; the introduction of right-handed neutrinos allows for

new terms in the Lagrangian. The term that should be included in the Lagrangian in order to construct the most general gauge invariant and renormalizable Lagrangian is of the type $m\overline{(\nu_{lR})^c}\nu_{lR}$. The term takes into account the fact that a right-handed neutrino is uncharged under all the gauge symmetries. This type of term, involving fields of the same chirality, is called Majorana mass term. It is the only possible term for neutrinos because for charged fermions it is not invariant under the $U(1)$ gauge symmetry of electromagnetism. A consequence of the existence of a Majorana mass term is that lepton number is not conserved. Conservation of lepton number is not associated with a gauge symmetry, like the conservation of electric charge is for example. Lepton number is an accidental symmetry of the Standard Model; its conservation is a result of the field content and the requirement of renormalizability. Lepton number is the only quantum number that distinguishes neutrinos and antineutrinos. If lepton number is not conserved, there is nothing left to distinguish neutrinos and antineutrinos: neutrinos, being identical to antineutrinos, would thus be Majorana fermions, i.e. fermions that are their own antiparticles.

III.B. Dirac and Majorana neutrinos

The Dirac equation describes a free spin -1/2 fermion, whether Dirac or Majorana, by a four-component spinor field ψ:

$$(i\gamma^\mu\partial_\mu - m)\psi = 0 \tag{26}$$

The field could be represented as the sum of left-handed and right-handed chiral projections, that is $\psi = \psi_L + \psi_R$ where

$$\psi_L = \left(\frac{1-\gamma_5}{2}\right)\psi \ , \ \psi_R = \left(\frac{1+\gamma_5}{2}\right)\psi \tag{27}$$

The field of a Majorana fermion, by definition, satisfies the condition:

$$\psi^c = \psi \tag{28}$$

where $\psi^c = \mathcal{C}\psi = \gamma_0\gamma_2\bar{\psi^T}$ and $\mathcal{C}$ is the charge-conjuction matrix. When $\mathcal{C}$ is applied to a left-handed field it becomes a right-handed one, and viceversa. Since neutrino has no electric charge, one can states that the right-handed component of the neutrino field is simply the $\mathcal{C}$-conjugated of the left handed field. If this possibility is verified then neutrino is said to be a Majorana particle. The Majorana condition implies that $\psi_R = (\psi_L)^c$, then the right-handed and left-handed components of a Majorana fields are not independent. The Lagrangian mass term for a Majorana neutrino can be written as:

$$-\mathcal{L} = -\frac{1}{2}m(\bar{\nu_L^c}\nu_L + \bar{\nu_L}\nu_L^c) \tag{29}$$

In principle neutrinos can have both Majorana and Dirac mass terms. Considering for simplicity the case of only one flavour, one can write:

$$-\mathcal{L} = \frac{1}{2}(\bar{\nu_L^c}\bar{\nu}_R)\begin{pmatrix} 0 & m_D \\ m_D & M_R \end{pmatrix}\begin{pmatrix} \nu_L \\ \nu_R^c \end{pmatrix} + \text{h.c} \ . \tag{30}$$

In eq. 30 we have the two independent fields ν_L and ν_R, m_D stands for the Dirac mass and M_R is the Majorana mass for ν_R; the coefficient m_L is set to zero since in the Standard Model ν_L has weak Isospin projection $I_3 = 1/2$, the corresponding Majorana mass term would be a Isospin triplet and would not be gauge invariant. The mass matrix introduced in eq. 30 can be diagonalized to find the corresponding mass eigenstates. After the mass matrix is diagonalized, the neutrino Lagrangian mass term becomes:

$$-\mathcal{L} = \sum_{k=1,2} m_k\bar{\nu_{kL}^c}\nu_{kL} + \text{h.c.} \tag{31}$$

where

$$\nu_1 = cos\theta\nu_L + sin\theta\nu_r^c \tag{32}$$
$$\nu_2 = -sin\theta\nu_L + cos\theta\nu_r^c \tag{33}$$

and $\tan 2\theta = m_d/M_R$.

As we can see from Eq. (31), even in the general case where the Dirac mass term is present, in the mass eigenstates basis neutrinos are described by Majorana fields. Moreover, while the Dirac mass m_D, that is generated by the Higgs mechanism, is expected to be of the same order of magnitude of the mass of other fermions, there are no limitations for the Majorana mass M_R; it can assume arbitrarily large values. The proccess by which neutrino takes mass is often referred to as the "See-Saw mechanism [33]. If $M_R \gg m_D$ from, Eq. (33) we have:

$$\nu_1 \simeq \nu_L \ , \ m_1 \simeq \frac{m_D^2}{M_R} \tag{34}$$
$$\nu_2 \simeq \nu_R^c \ , \ m_2 \simeq M_R \tag{35}$$

If this condition is verified, the heavy neutrino ν_2 is predominantly ν_R^c and the light neutrino ν_1 is essentially the observed particle ν_L. Thus with the introduction of the Majorana mass term in the Lagrangian we obtain a natural explanation for the smallness of neutrino masses: the bigger is the mass of the unseen particle ν_R, the smaller is the mass of ν_L. The nature of neutrinos, Dirac or Majorana, and whether lepton number is conserved in nature are open experimental questions. Experiments aiming to answer these questions attempt to observe a lepton-number-violating process with neutrino-less double beta decay, being the most promising candidate.

III.C. Neutrinoless Double Beta Decay

Double beta decay is a rare spontaneous transition in which the nuclear charge changes by two units while the mass number remains the same (two neutrons simultaneously transmute into two protons). This decay may occurs with the emission of two neutrinos (two-neutrino double beta decay, $2\nu\beta\beta$) or without (neutrino-less double beta decay, $0\nu\beta\beta$). The latter hasn't been officially observed yet. In 1935 Goeppert-Meyer first calculated the probability for the $2\nu\beta\beta$-decay, using Fermi's theory of weak decays and predicted half-life time in excess of 10^{20} yr [34]. In 1937 Majorana proposed that the neutrino particle might be indistinguishable from its antiparticle [35]. In the same year, Racah, building upon the fundamental suggestion of Majorana, discussed the possibility of a neutrino-less transformation of two neutrons into two protons plus two electrons [36]. Furry in 1939 realized that $0\nu\beta\beta$-decay could be mediated by virtual neutrino and predicted the half-life on the level of $T_{1/2}^{0\nu} = (10^{12} \div 10^{15})$ years [37]. The existence of double-beta decay was first confirmed in a series of geochronological experiments in 1950 using ^{130}Te and then in 1967 with ^{82}Se.

While these measurements unequivocally demonstrated that double beta decay was a real phenomenon, nothing could be inferred about the particular mode of double-beta decay (two neutrinos or neutrinoless) responsible of the daughter products. The two-neutrino double beta decay mode, shown in Fig. 9 is expected in the Standard Model as a second order weak semileptonic process, and it imposes no special requirements on the properties of the neutrino. It will occur independently of whether the neutrino is a Majorana or a Dirac particle and also independently of whether it has mass or not. More interesting thing is the neutrino-less double beta decay, reported in Fig. 9, with the emission of a neutrino from one neutron and its absorption on another. This process violates the lepton number conservation ($\Delta L = 2$) and is therefore forbidden in the standard electroweak theory. For this reason it could be a possible window into a physics beyond the Standard Model. Indeed the $0\nu\beta\beta$ decay can occur only if two requirements are satisfied:

1. the neutrino exchanged has to be a Majorana particle. This means that antineutrino and neutrino are actually the same particle ($\nu = \bar{\nu}$);
2. the neutrino has to have a non-vanishing mass and/or the neutral current has to have a right handed (V+A) component. This condition is needed because of the helicity of the neutrino. Due to the $V-A$ nature of the weak interaction, the neutrino emitted in the first vertex is right-handed, while in order to be absorber in the second one, it needs to change its helicity. This is possible only if the neutrino has a finite mass and, in this case, the decay amplitude is proportional to m_ν.

From a Particle Physics point of view the neutrino-less double beta decay is a very important process insofar as representing a unique tool to establish the absolute neutrino mass scale, its nature (Dirac/Majorana) and the values of the Majorana CP phase. Starting from experimental results on $0\nu\beta\beta$ decay lifetimes it's possible

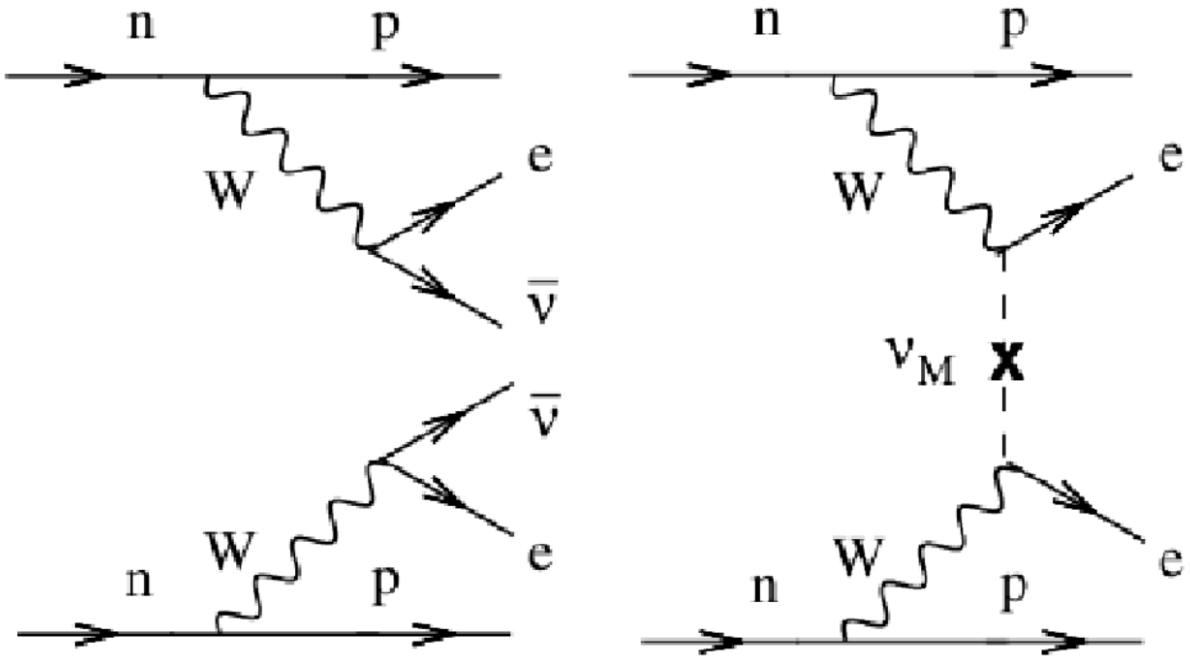

FIG. 9. Possible $\beta\beta$ transitions. Left: Feynman diagram for $2\nu\beta\beta$ decay. The lepton number is conserved ($\Delta L = 0$), this transition is expected in the standard electroweak theory. Right: Feynman diagram for $0\nu\beta\beta$ decay. The lepton number is violated ($\Delta L = 2$), this transition is forbidden in the standard electroweak theory. (Credit: Ref. [38].)

to determinate the very important quantity $\langle m_\nu \rangle$ called effective neutrino mass. In order to extrapolate this parameter a precise knowledge of the nuclear transition matrix elements is required. It is easy to distinguish the two decay modes by the shape of the electron sum energy spectra, which are determined by the phase space of the outgoing light particles. In the $2\nu\beta\beta$ decay the summed kinetic energy K_e of the two electrons displays a broad maximum below half the endpoint energy; while in the $0\nu\beta\beta$ mode, the two electrons carry the full available kinetic energy and the spectrum is therefore a single peak at the endpoint, see Fig. 10.

Considering only the case of left-handed V-A weak current and light massive Majorana neutrinos, the differential decay rate (inverse half-time) for the $\beta\beta0\nu$ transition can be written as:

$$\Gamma^{0\nu}_{1/2} = [T^{0\nu}_{1/2}(0^+ \to 0^+)]^{-1} = F_N \frac{|\langle m_\nu \rangle|^2}{m_e^2}, \tag{36}$$

where:

$$\frac{F_N}{m_e^2} = G^{0\nu}(E_{max}, Z) \left| M^{0\nu} \right|^2, \tag{37}$$

with:

$$\left| M^{0\nu} \right|^2 = \left| M^{0\nu}_{GT} - \frac{g_V^2}{g_A^2} M^{0\nu}_F \right|^2 \tag{38}$$

$G^{0\nu}$ is the exactly calculable phase space integral, $\left| M^{0\nu} \right|^2$ is the specific nuclear matrix element of the nucleus undergoing the decay (M_{GT} and M_F are, respectively, the Gamow-Teller and Fermi matrix elements), g_V and g_A are the vector and the axial-vector coupling constant and, at last, the parameter m_e is the electron mass. The nuclear structure factor F_N is calculable using different nuclear models. The parameter $\langle m_\nu \rangle$ is the effective electron neutrino mass (often written as $\langle m_{ee} \rangle$) also called effective Majorana mass. This mass is directly derivable from the measured half-life of the decays as follows:

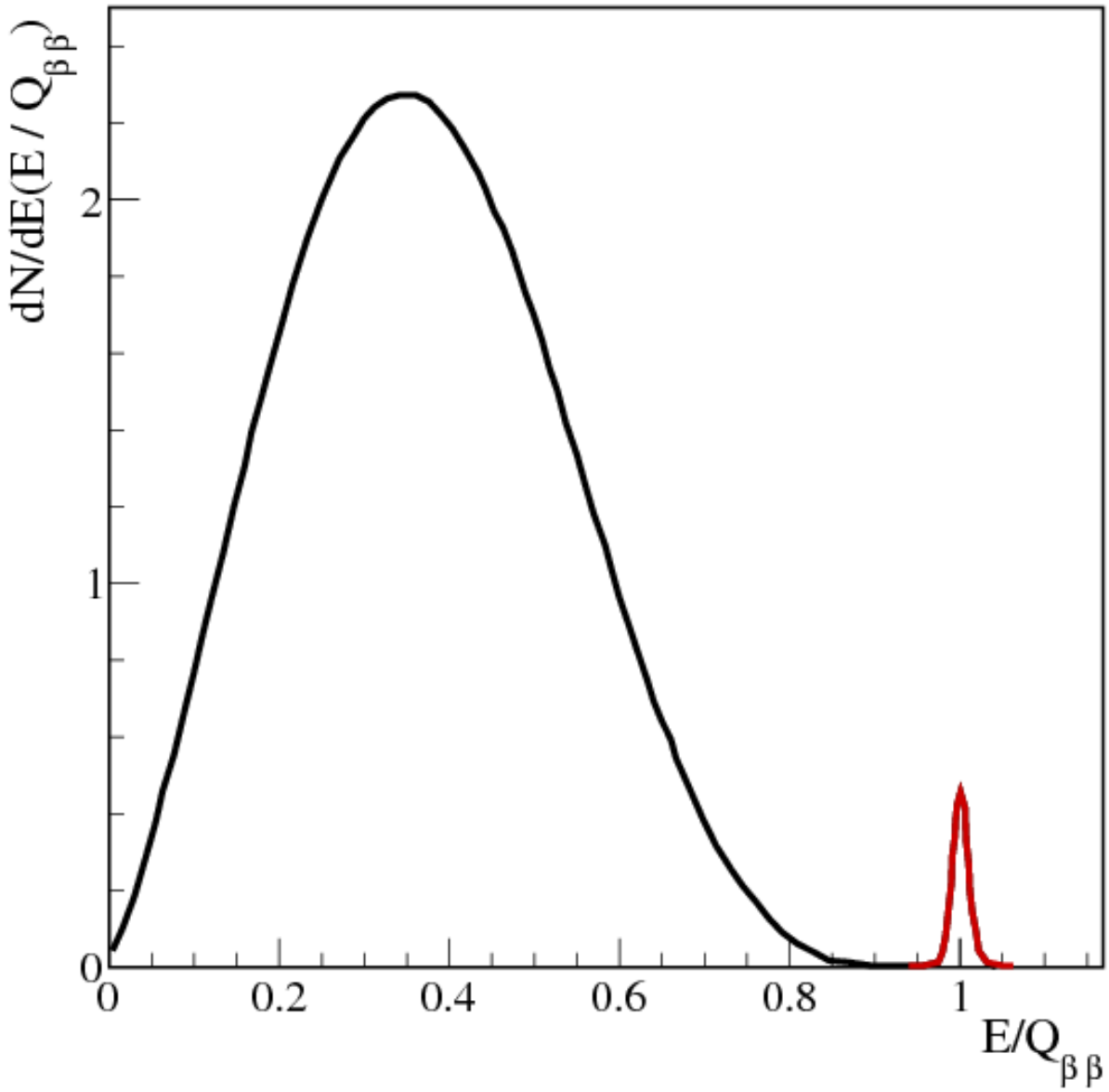

FIG. 10. Energy spectrum of a $\beta\beta$ decay. The portion of the spectrum highlighted in red at the $Q_{\beta\beta}$ endpoint indicates the contribution from the $0\nu\beta\beta$ decay mode. (Credit: Ref. [39].)

$$|\langle m_\nu \rangle| \equiv |\langle m_{ee} \rangle| = m_e \frac{1}{\sqrt{F_N T_{1/2}^{0\nu}}} \tag{39}$$

The value of $|\langle m_\nu \rangle|$ is derived from nuclear structure calculation, and, for this reason it is model dependent.

IV. THE DARKSIDE PROGRAM

Noble liquids, specifically liquid Xenon (LXe), liquid Argon (LAr), liquid Neon (LNe), and liquid helium (LHe) are excellent scintillators. All four targets can be purified to the level where the probability of capture of electrons becomes negligible. In LXe and LAr, it is very easy to drift electrons over very long distances (less so for LNe and LHe, where electrons create a "vacuum bubble" displacing nearby atoms, and have an effective mass comparable to that of atoms [40]).

The possibility of simultaneously detecting ionization and scintillation signals in LXe and LAr, along with the ease of purification and possibility of scaling to very large masses, makes them ideal candidates for dark matter and other rare events detectors.

In this chapter I will discuss the DarkSide program of dark matter searches with LAr detectors with one unique trait, the use of low-background argon from underground sources (UAr).

IV.A. Physical Properties and Processes of Noble Liquids

When radiation passes through a noble liquid starts a series of processes that at the end create photons, i.e scintillation and ionization.

The ionization process: the energy loss of an incident particle in noble liquids is dissipated into the medium according to its nature and kinematics and leads to the creation of electron-ion pairs;

The scintillation process: luminescence emitted from liquids or solids is called scintillation. Scintillation from noble liquids arises from two distinct processes: the so called recombination luminescence and excitation luminescence.

The recombination luminescence originates from the following processes:

$$\begin{aligned} R^+ + R &\rightarrow R_2^+, \\ e^-_{\text{hot}} + \text{collisions} &\rightarrow e^-_{\text{thermal}}, \\ R_2^+ + e^-_{\text{thermal}} &\rightarrow R^{**} + R, \\ R^{**} &\rightarrow R^* + \text{heat}, \\ R^* + R &\rightarrow R_2^*, \\ R_2^* &\rightarrow R + h\nu\,(\text{UV}), \end{aligned} \tag{40}$$

where R^+ stands for an atomic ion, R^* for an excited atom, R^{**} for an highly excited atom, R_2^+ for a molecular ion, R_2^* for an excited molecule, e_{hot} for a sub-excitation electron and e_{thermal} for a thermalized electron. As suggested by the name this process is essentially driven by the presence of a free electron-ion pair; on the other hand the excitation luminescence is produced by the simpler process showed in 41 and 42:

$$R^* + R \rightarrow R_2^*, \tag{41}$$

$$R_2^* \rightarrow R + R + h\nu\,(\text{UV}). \tag{42}$$

The excitation luminescence leads to the creation of excimers (R_2^*), that can exist both in singlet and triplet states. The decay of these states produces the emission of a 128 nm UV photon for argon and 172 nm UV photon for xenon.

However the decay times of singlet and triplet states are different. For example they could be very near in time, as in xenon, with decay times 2 ns and 22 ns respectively [41], or could be more separated, like in LAr, with values of 6 ns and ∼1.5 µs [41]. Of course, when the values of the two decay times are very close, it becomes much more difficult to recognize apart the signal belonging to the two classes of photons.

The values of decay times depend only weakly on the ionization density of the particle, but the ratio of singlet to triplet states is higher at higher ionization density. A nuclear recoil of a neutron with the atom of the noble liquid will produce a cloud of electron-ion pairs much more dense than that of an electron, which scatters with atoms of the noble liquid by electron recoil producing a more sparse cloud of electron-ion pairs.

Fig. 11, from Ref. [42], shows the decay times of the singlet and triplet states for different impinging particles in LAr the interaction of electrons and neutrons produce both singlet states and triplet states, which decay with very different times, and the very significant difference in population of the singlet and triplet states LAr can be exploited for discriminating the source of ionization via pulse shape discrimination (PSD).

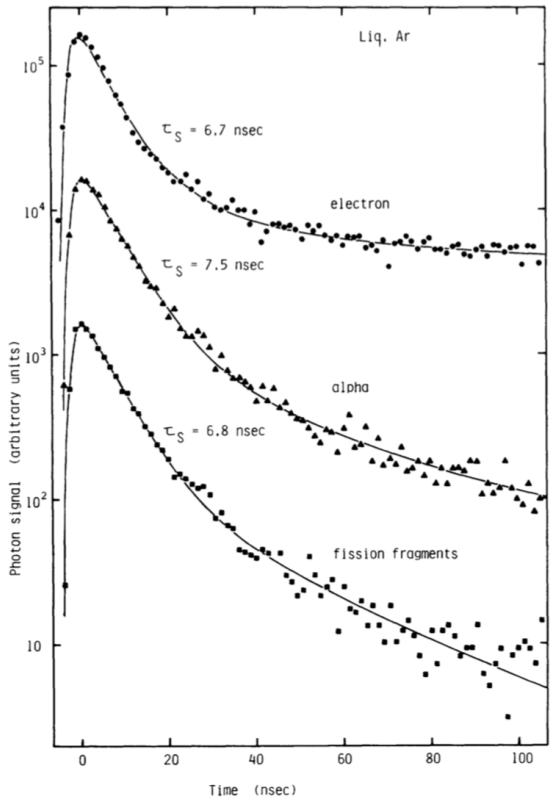

FIG. 2. Typical decay curves obtained for the luminescence from liquid argon excited by electrons (●), α particles (▲), and fission fragments (■) shown for the short time range. A slightly slow rise for electron excitation may be due to the recombination.

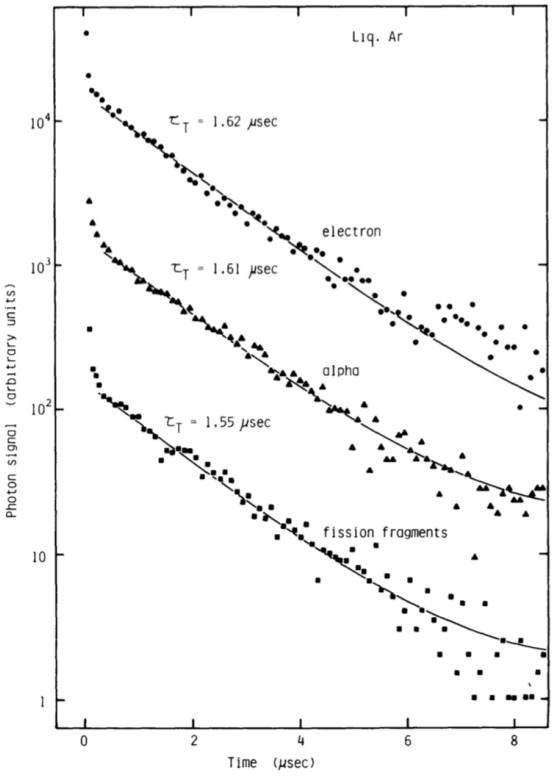

FIG. 3. Typical decay curves obtained for the luminescence from liquid argon excited by electrons (●), α particles (▲), and fission fragments (■) shown for the long time range. The fast exponential decay component is not shown in the figure.

FIG. 11. Decay curves for triplet and singlet states LAr dimers induced as results of different ionizing sources [42].

The first realization of the very significant statistical power of discrimination of the primary LAr scintillation is due to Boulay and Hime [43], which in their 2006 paper detailed how the detection of a limited (a few tens) number of scintillation photons could generate an enormous discrimination power in LAr, due to the combination of the very strong unbalance in population of the singlet and triplet states (1:3 for electron recoils and 3:1 for nuclear recoils) and to the huge difference in decay times (from 6 ns to ∼1.5 µs). Under the assumptions that one could completely separate singlet from triplet photoelectrons and that the ratio of population is exactly 1:3 for electron recoils and 3:1 for nuclear recoils, a purely statistical argument can show that the PSD corresponding to a 60 PE threshold is already at the level of one part in 10^6, and that the discrimination power would increase by one order of magnitude for the additional 10 PE to the threshold values. The first demonstration of PSD in LAr took place in LNGS thanks to the results of the WArP Collaboration in 2006 [18]. Today, the results of PSD obtained with the DarkSide-50 and DEAP-3600 detectors fall incredibly in line with the original argument. The best value of PSD experimentally demonstrated is of one part in 2.4×10^8 [44].

In a real experiment, it is customary to build one parameter which provides most (if not all) of the discrimination power required. The parameter is sometimes referred to as that allowed to discriminate nuclear recoil and electron recoil is the so called f_{prompt}parameter, defined as the ratio of fast component of the primary scintillation signal, integrated over a window of a few tens of ns from the start of the pulse, to the total integral of the scintillation pulse, integrated over a few µs from the start of the pulse. In a detector able to identify the time of the arrival of the individual photons composing the scintillation pulse f_{prompt} can be defined as in 43:

$$f_{\text{prompt}} = \frac{\sum_i \text{PE}_{i,\text{prompt}}}{\sum_i \text{PE}_i}, \tag{43}$$

where i indicates the sequential number of the photon detected in said real experiment. We note that the strong PSD available in LAr scintillation detectors is practically absent in LXe detectors: even if the strong imbalance of population persists, the nearly identical decay time of the singlet and triplet scintillation components (2 ns and 22 ns) inhibits the separation of the two classes of photons and nullifies the potential separation power of PSD.

In addition to PSD, LAr detector able to detect the ionization signal can also exploit an additional, interesting discrimination tool. Very dense ionizing tracks such as those induced by nuclear recoils are known to undergo a strong recombination process [41, 42, 45–47]. This recombination effectively suppresses the number of free charges, electrons and ions, that can be drifted apart from the original position of the ionizing track. As a result, the ratio of the ionization to scintillation signal is strongly suppressed for nuclear recoils relative to minimum ionizing events. This type of discrimination was first introduced, in the context of dark matter detection, at CERN in the early 1990's [48, 49]. Today, it serves as the major discrimination tool in use in LXe-based dark matter searches with TPCs [50–53]. This technique was first exploited in a LAr TPC by the WArP Collaboration [18] and perfected for use in LAr TPCs by the DarkSide Collaboration [54–56]. For both LXe and LAr detectors, at the lower end of the energy range of interest this discrimination typically reaches values of one part in 10^2 to 10^3 for a typical 50 % acceptance of nuclear recoils (the purported dark matter signal).

IV.B. The Past and Present: DarkSide-50

Experiments attempting to directly detect WIMP dark matter via scattering on target nucleons must be carefully designed to reduce neutrons-, β-, and γ-induced backgrounds. The DarkSide-50 experiment consists of three nested detectors: from the center outward the three detectors are: the Liquid Argon Time Projection Chamber, which is the dark matter detector filled with (153 ± 1) kg of LAr depleted in ^{39}Ar, an active mass of (46.4 ± 0.7) kg, and a fiducial mass of (36.9 ± 0.6) kg; the liquid scintillator veto (LSV), serving as shielding and as anti-coincidence for radiogenic and cosmogenic neutrons, γ-rays and cosmic muons, filled with boron-loaded liquid scintillator. Finally the water Cherenkov veto (WCV), serving as shielding and as anti-coincidence for cosmic muons filled with high purity water. The three detectors will be described in more detail soon.

The active region of the two-phase liquid argon time projection chamber (LAr TPC) is constituted by a cylinder of low-radioactivity teflon of diameter 356 mm and height 363 mm, filled with (46.4 ± 0.7) kg of LAr. The LAr is present in the active volume to a height of 353.5 mm, above which there is a 1 cm gas ullage. The 353.5 mm height of the LAr column is separated by a 50 µm mesh (serving as an intermediate electrode, see next sentence) between a bottom LAr column of 348.8 mm height and a top LAr column of 4.7 mm height, terminating with the surface of separation between liquid and gas. Three electrodes, the cathode at the bottom of the active volume, the 95 % transparent mesh below the liquid surface just mentioned, and the anode at the top of the TPC ullage define electric potentials at the bottom of the liquid, near the liquid surface and at the top of the gas region. A thin layers of indium-tin-oxide (ITO) covers the top of the bottom and the bottom of the top silica window.

A uniform field region, the so called drift field, is established in the bulk liquid target between the cathode and the grid via a set of copper field-rings sitting at a graded potential. A second, more intense field, the extraction field, is applied between the grid and the anode. When energy is deposited in the LAr target, a primary scintillation light pulse (S1) is emitted and a column of electron-ion pairs is produced. The ionized electrons which escape recombination are drifted by the electric field in the liquid towards the liquid surface, from which they are extracted into the ullage by the extraction field. As the electrons pass through the gas region, they induce further emission of light by electro-fluorescence in the gas (the S2 signal). The wavelength shifter tetraphenylbutadiene (TPB) is used to convert the argon scintillation light, emitted in the VUV range at 128 nm, to the visible range and it is evaporated on the inner surfaces of the active volume. Both the S1 and S2 signals are viewed through the silica windows by a system of 38 PMTs, 19 above the anode and 19 immediately below the cathode. The first signal, S1, gives information on the amount of energy deposited and, through its time profile, on the type of interaction in the liquid. The second signal, because of its proximity to the top PMTs, gives information on the x-y position of the interaction; given the known drift-velocity of electrons in the liquid argon, the time interval between S2 and S1 gives information on the depth within the liquid of the interaction. The original interaction can thus be localized in 3D within a few mm. Fig. 12 shows a schematic view of the TPC.

The LSV is a 4.0 m diameter stainless steel sphere filled with 30 t of boron-loaded liquid scintillator. The internal walls are covered with Lumirror, a reflecting foil used to enhance the light collection efficiency. An array of 110 Hamamatsu R5912 LRI 8″ PMTs is mounted on the inside surface of the sphere to detect scintillation photons. A photographs of the internal of the LSV detector is shown in Fig. 13.

The boron-loaded liquid scintillator consists of a mixture of three components: pseudocumene (PC), trimethylborate (TMB), and 2,5-diphenyloxazole (PPO). PC is the primary scintillator, TMB is an organic

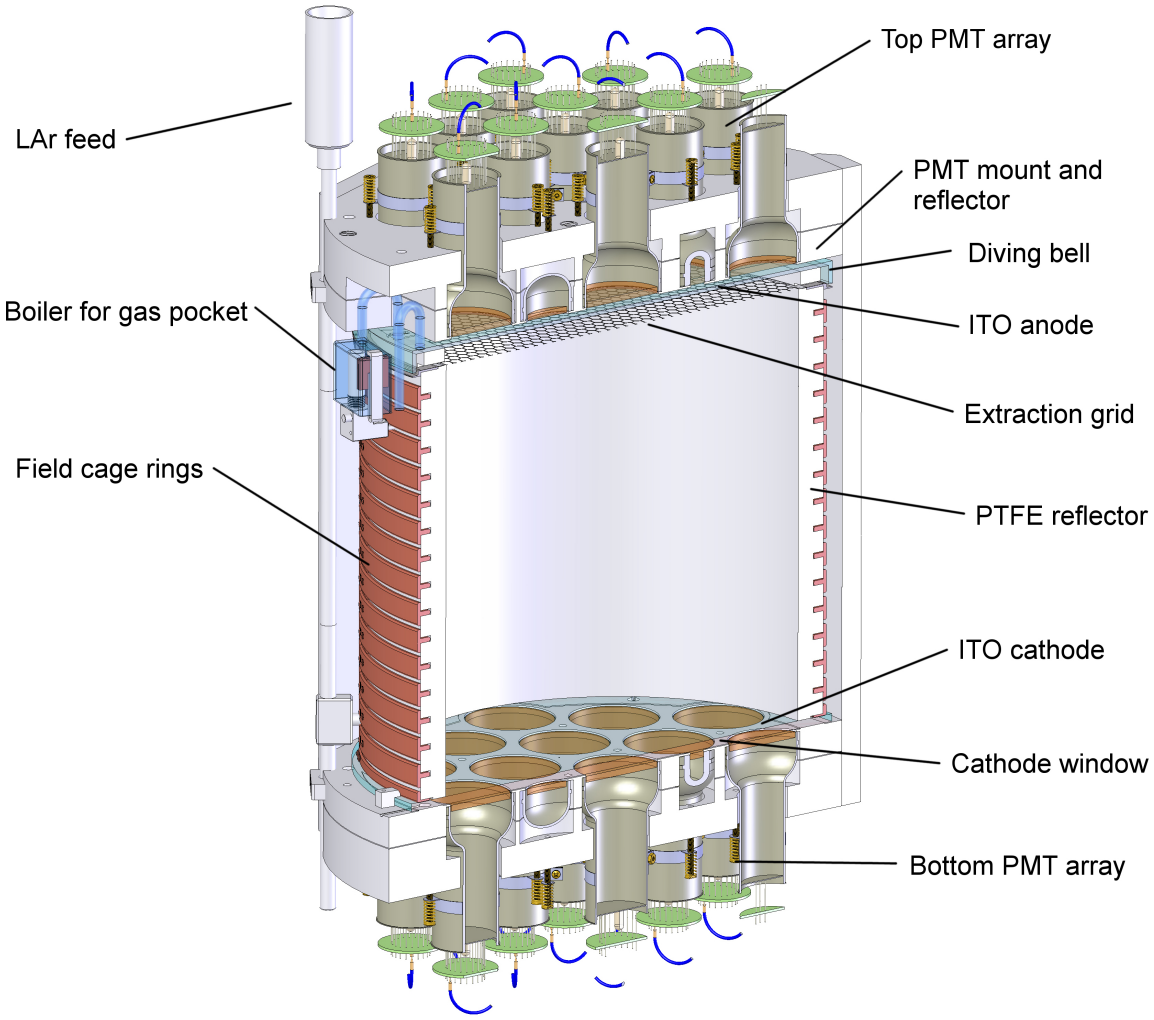

FIG. 12. 3D rendering of the DarkSide-50 LAr TPC. The photodetectors are PMTs looking at the active LAr volume contained in the cylindrical TPC. Copper rings around the cylinder provide the electric field, assisted by a metal grid near the top of the argon volume, located just below the ullage, which serves the purpose of enabling the process of electroluminescence of the electrons extracted from the liquid target volume.

molecule carrying boron, and PPO is a wavelength shifter. The neutron capture reaction $^{10}\mathrm{B}(n,\alpha)^{7}\mathrm{Li}$ makes boron-loaded scintillator a very effective neutron veto because of its large cross section for thermal capture ($\backsim$ 4000 barn). When a neutron captures on ^{10}B two reactions are possible:

$$^{10}\mathrm{B} + n \rightarrow {}^{7}\mathrm{Li}(1015\,\mathrm{keV}) + \alpha(1775\,\mathrm{keV}) \qquad 6.4\,\%, \tag{44}$$

$$^{10}\mathrm{B} + n \rightarrow {}^{7}\mathrm{Li}^{*} + \alpha(1471\,\mathrm{keV}) \hookrightarrow \qquad 93.6\,\% \tag{45}$$

$$\hookrightarrow {}^{7}\mathrm{Li}^{*} \rightarrow {}^{7}\mathrm{Li}(839\,\mathrm{keV}) + \gamma(478\,\mathrm{keV}). \tag{46}$$

Detecting these decay products requires a high light collection efficiency and low background. The decay to the excited state produces a γ-ray that is easily seen as long as it does not escape into the cryostat before depositing energy into the scintillator. Energy deposits due to the α and ^{7}Li nucleus are always contained in the scintillator, due to their high stopping power and consequently short track length. This gives boron a comparative advantage over other loading options such as gadolinium, which only produces high energy γ-rays which may escape the veto without leaving a detectable signal. Detecting these decay products requires a high light collection efficiency and low background. However, the light output of α and

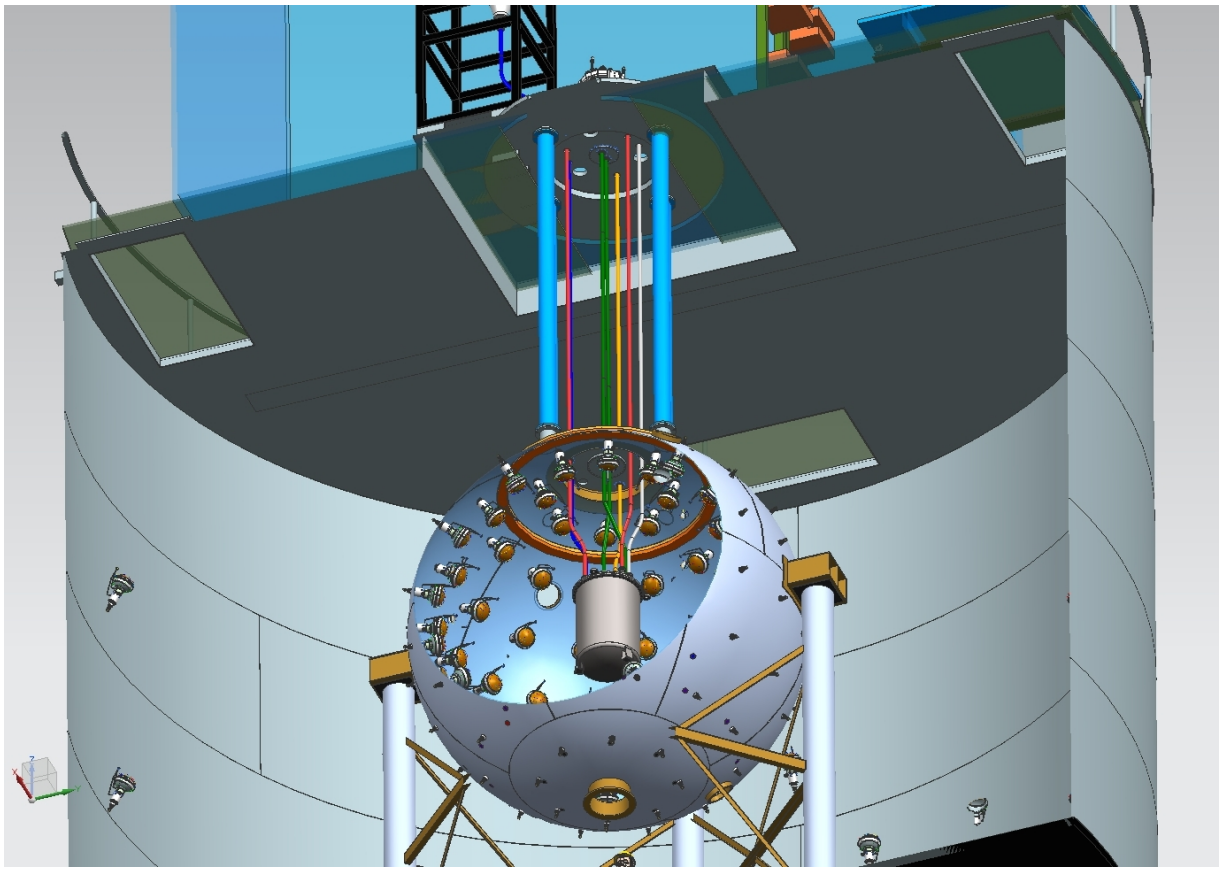

FIG. 13. The Liquid Scintillator Veto. The picture shows the internal surface of the LSV, covered with the Lumirror reflector, with PMTs evenly assembled over the surface.

^{7}Li nuclei is highly suppressed due to ionization quenching, causing them to scintillate equivalently to a 30 to 35 keV$_{ee}$ (keV$_{ee}$ is the "electron equivalent" energy scale).

Neutrons that enter the TPC of DarkSide-50 and interact with LAr are expected to come primarily from four sources.

- Fission reactions in the detector materials, uranium and thorium contamination in the detector components.
- (α, n) reactions in the detector materials, α-emitting radioisotopes contaminating the detector components may interact with light nuclei to produce neutrons in the detector materials.
- Environment radioactivity constituted primarily by uranium and thorium in the surrounding rocks that can produce fission or (α, n) neutrons.
- Cosmogenic interactions, cosmic ray muons can interact with the detector or surrounding materials to produce high energy (typically around 100 MeV) neutrons, or they can produce unstable nuclei that will decay and produce lower energy neutrons.

Neutrons from the last two sources are easily eliminated by the detector's design: the WCV detects passing muons, and the LSV provides a substantial amount of shielding as well as a visible signal before external neutrons can reach the LAr TPC; moreover fission reactions often generate multiple neutrons and high energy γ-rays giving rise to multiple coincident interactions in the LSV at the same time that a neutron interacts with the LAr. This leaves (α, n) neutrons as the most challenging type of neutron to veto, and much of the design and analysis is targeted around vetoing these neutrons with a high efficiency. When a neutron enters the LSV from the LAr TPC there are two signals that can be used to detect and veto the neutron: the first signal is the prompt thermalization signal produced by the neutron slowing down in the LSV that scatters off the nuclei in the scintillator, mostly on hydrogen and carbon; the second signal is the delayed signal from the neutron capture. The thermalized neutron can capture on various isotopes in the scintillator, typically on a time scale on the order of 1 µs to 100 µs. In addition it is also possible to indirectly veto neutron events in the LAr TPC: if a neutron scatters in the TPC but captures on detector components, this capture reaction may produce a γ-ray that can later be detected in the LSV on a timescale up to 60 µs after the scatter in the TPC, as shown in Monte Carlo simulations.

FIG. 14. View of the inside of the WCV of the DarkSide-50 detector. The stainless steel sphere of the LSV at the center of the water tank is shown covered with its Tyvek reflector. PMTs are mounted on the wall and floor of the WCV.

If a neutron is produced by a cosmic ray muon, it is possible to mark the neutron by detecting the muon in the WCV. Alternatively, if the muon produces neutrons in the rock surrounding the experiment and does not pass through the WCV, it may be possible to detect charged products of the electromagnetic shower accompanying the neutron's production in the rocks. Neutrons that scatter once in the LAr TPC and don't produce any signal in the vetoes, directly or indirectly, will not be vetoed and may produce a fake WIMP-like event in DarkSide-50. Monte Carlo simulations show that only $\sim$0.05 % of radiogenic neutrons produced by the (α, n) reaction leave absolutely no signal in the LSV.

The water tank of the WCV is a 11 m diameter, 10 m height cylindrical tank with a fill 1 kt of ultra-pure water that acts as a shield against external background (γ-rays and neutrons from the rock) and as a Cherenkov muon detector. The muon flux at the 3800 m.w.e. LNGS depth is $1.2/(\mathrm{m}^2\,\mathrm{h})$. An array of 80 ETL 9351 8″ PMTs, with 27 % average quantum efficiency at 420 nm, is mounted on the side and bottom of the water tank, 56 on the cylindrical tank wall and 24 on the floor. These PMTs collect the Cherenkov light emitted by muons or muons electromagnetic shower products in the water. Picture of the WCV is showed in Fig. 14. In order to improve the light collection efficiency, the inside surface of the tank is covered with a laminated Tyvekpolyethylene-Tyvek reflector. The reflectivity of this material has been measured to be greater than 96 % in air and 99 % in water, for light's wavelenght of 300-800 nm.

IV.C. Results from the first use of low radioactivity argon in a dark matter search

The goal of the analysis is to distinguish events that are induced by the scattering of WIMPs in the active LAr from those caused by any other process. The signature of a WIMP scattering event is a single-sited nuclear recoil. The dominant backgrounds by far are those from β/γ decays in the materials of the TPC and cryostat. We performed a non-blind physics analysis on the data set and impose several classes of cuts:

1. Selection of single-sited events in the TPC, this eliminates part of the neutrons and of the γ-ray induced background. It requires that events contains two pulses, S1 and a single S2
2. Cuts to establish the validity of the S1-S2 identification of the found pulses are applied to allow use of these pulses for PSD and fiducialization. We require that the first pulse occur at the expected time

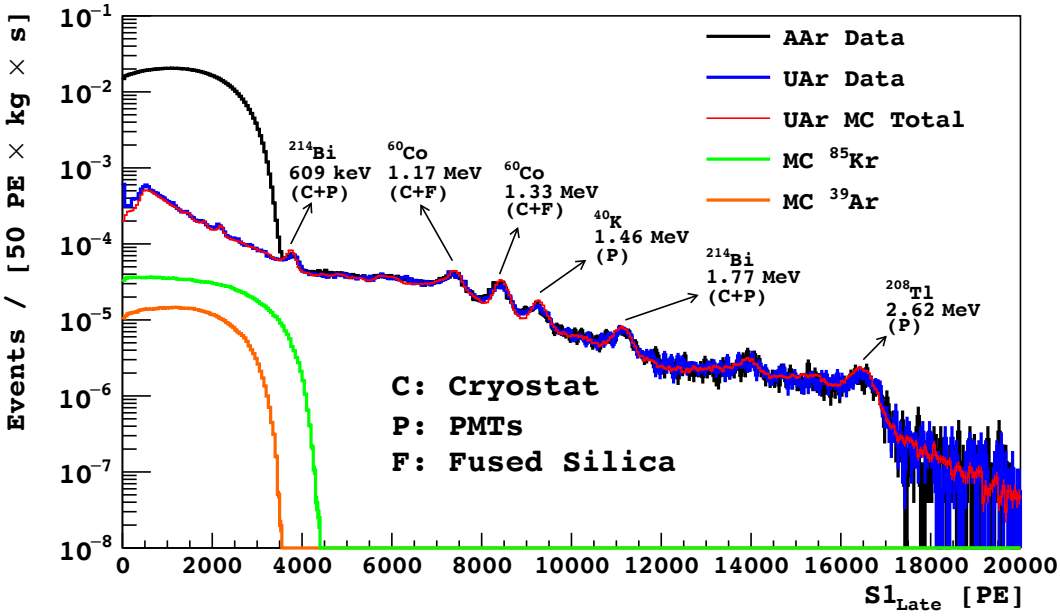

FIG. 15. From Ref. [54], comparison of the measured field off spectra for the UAr (blue) and AAr (black) targets, normalized to exposure. Also shown are the MC fit to the UAr data (red) and individual components of ^{85}Kr (green) and ^{39}Ar (orange) extracted from the fit.

in the acquisition window to within 50 ns, consistent with our assumption that we triggered on S1.

3. We see evidence for Cherenkov background, including a sample of events with both f90$\sim$ 1 and nearly all the S1signal in a single PMT. We cut events in which the S1 light is abnormally concentrated in a single PMT.
4. Veto detector information is used to suppress events with either prompt energy deposition in the LSV from neutron thermalization, or delayed energy deposition from neutron capture γ rays, notably those from the dominant ^{7}Li* final state from capture on ^{10}B in the scintillator.
5. The fiducial volume is limited in the vertical coordinate (measured by electron drift time) only, no radial cut is applied. We place a fiducial cut retaining events with drift times between 40.0 µs and 334.5 µs, corresponding to 36.3 mm below the grid and 36.3 mm above the cathode. This reduces the total active volume to (36.9 $\pm$ 0.6)kg, where the dominant uncertainty arises from the uncertainty on the shrinkage of the teflon body of the TPC when cooled from room temperature to cryogenic temperature.

Atmospheric argon contains $\backsim$ 1 Bq/kg of cosmic ray produced ^{39}Ar. A source of argon with reduced ^{39}Ar activity is a crucial requirement for developing experiments that will push argon-based WIMP dark matter direct detection searches to their highest possible sensitivity. Since ^{39}Ar is produced by cosmic ray interactions in the upper atmosphere, principally via ^{40}Ar(n, 2n)^{39}Ar reactions, gas from underground is a possible source of argon with low levels of ^{39}Ar. Gases from Kinder Morgan CO_2 in Cortez, Colorado, were found to contain low radioactivity argon: the DarkSide-50 experiment is the first experiment which uses as target for dark matter underground argon naturally depleted in ^{39}Ar extracted in Colorado and purified at Fermilab in a multi-year effort, [57–59]. Figure 15 reports the activity of ^{39}Ar in atmospheric Argon (AAr) and in underground Argon, measured in DarkSide-50.

After data quality cuts, we obtain 70.9 live days of WIMP search data with the UAr. The null result of the UAr exposure sets the upper limit on the WIMP-nucleon spin-independent cross section of 3.1 $\times 10^{-44}$ cm^2(1.4×10^{-43}cm^2, 1.3×10^{-42}cm^2) for a WIMP mass of 100 GeV/c^2 (1 TeV/c^2, 10 TeV/c^2). When combined with the null result of previous AAr run, [55], we obtain an upper limit of 2.0×10^{-44} cm^2(8.6×10^{-44} cm^2, 8.0×10^{-43} cm^2) for a WIMP mass of 100 GeV/c^2 (1 TeV/c^2, 10 TeV/c^2) [55]. Fig. 16 compares these limits to those obtained by other experiments. The DarkSide-50 detector is currently accumulating exposure in a stable, low-background configuration with the characteristics described above.

The most recent result obtained by DarkSide collaboration is reported in Fig. 16 corresponding 532.4 live-days exposure of DarkSide-50.

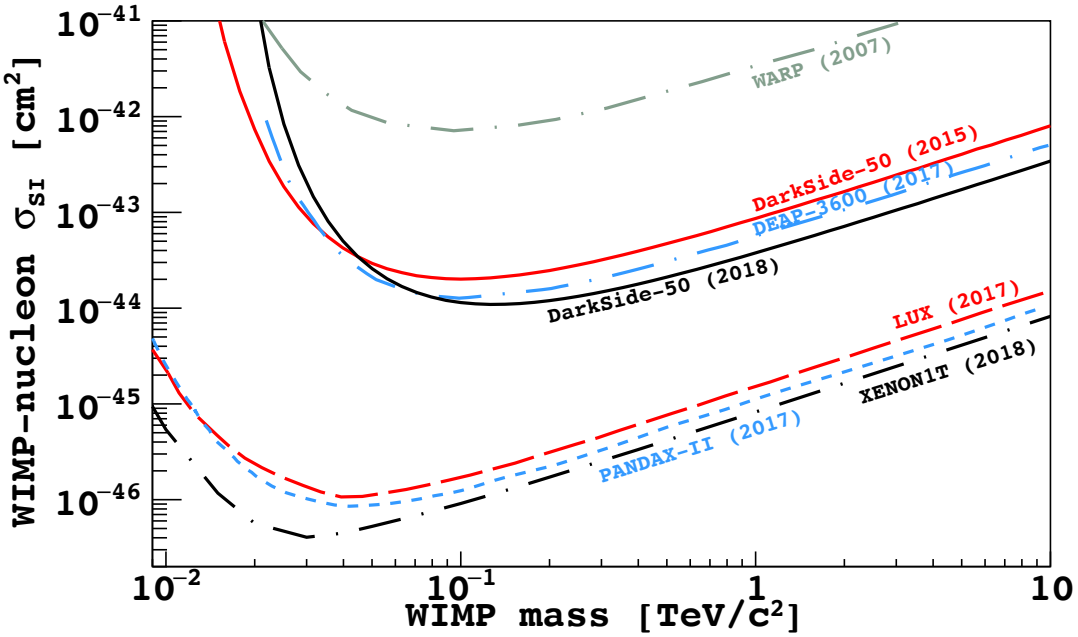

FIG. 16. From Ref. [55], spin-independent WIMP-nucleon cross section exclusion limits (90 % C.L.) from a 532.4 live-days campaign, compared to previous result from a more limited campaign [55] and selected leading (at the time of publication results from other LAr [18, 44] and LXe experiments [52, 53, 60].

As explained in the first chapter one of the most favoured candidate in a particle physics interpretation of Dark Matter are WIMPs, which obtains their relic abundance by thermal freeze-out through weak interactions, there is as yet no unambiguous evidence of WIMP direct detection, warranting searches for other possible DM paradigms. Another well-motivated class of DM candidates is low mass (few GeV) particles interacting through a vector mediator with couplings smaller than the weak-scale. These light DM candidates arise in a variety of models, and there are a number of proposed mechanisms that naturally obtain the expected relic abundance for light DM. Light DM may have couplings to electrons, and because the energy transferred by the DM particle to the target depends on the reduced mass of the system, electron targets more efficiently absorb the kinetic energy of sub GeV-scale light DM than a nuclear target. In the early 2018, the DarkSide-50 collaboration published 532.4 live-days campaign, albeit returning null result in the high-mass WIMP dark matter search, demonstrated an extremely low background, high stability, and low 0.1 keV$_{ee}$ analysis threshold [61]. These elements enable a study of very-low energy events, characterized only by the presence of the ionization signal, since WIMPs in the sub GeV mass range produce nuclear recoils well below 1.66 keV$_{ee}$, where the efficiency for detecting the S1 signal is too low and PSD is moreover not available. The analysis resulted in the world-best limit for low-mass dark matter searches in the mass range 1.8 GeV/c^2 to 6.0 GeV/c^2 as shown by C.L. exclusion curves shown in Fig. 17 [61].

In this regard the Collaboration has decided that it will propose to LNGS the construction and operation of DarkSide-LowMass (DS-LM), a search specialized for discovery of dark matter in the low mass region. In the next chapter I will discuss in detail the geometry and functioning of the elements of a DarkSide-Proto like detector, then I will describe the proposed new detector DarkSide-LowMass that introduces some new features aimed to optimize the search of dark matter in the low-mass range.

IV.D. The Future: DarkSide-20k

Based on the good results reached by DarkSide-50 an enlarged DarkSide Collaboration proposes the construction of DarkSide-20k a direct WIMP search using a LAr TPC filled with UAr. DarkSide-20k will be a detector with ultra-low background levels and the ability to measure its backgrounds in situ, designed to achieve a background-free exposure of 100 t yr accumulated during a run of approximately 5 yr. Thanks to its exceptionally low instrumental background, DarkSide-20k could extend its operation to a decade, increasing the exposure to 200 t yr and reaching a sensitivity to WIMP-nucleon interaction cross sections of 7.4×10^{-48} cm^2 for a WIMP mass of 1 TeV/c^2 [62]. The projected sensitivity of DarkSide-20k is showed in

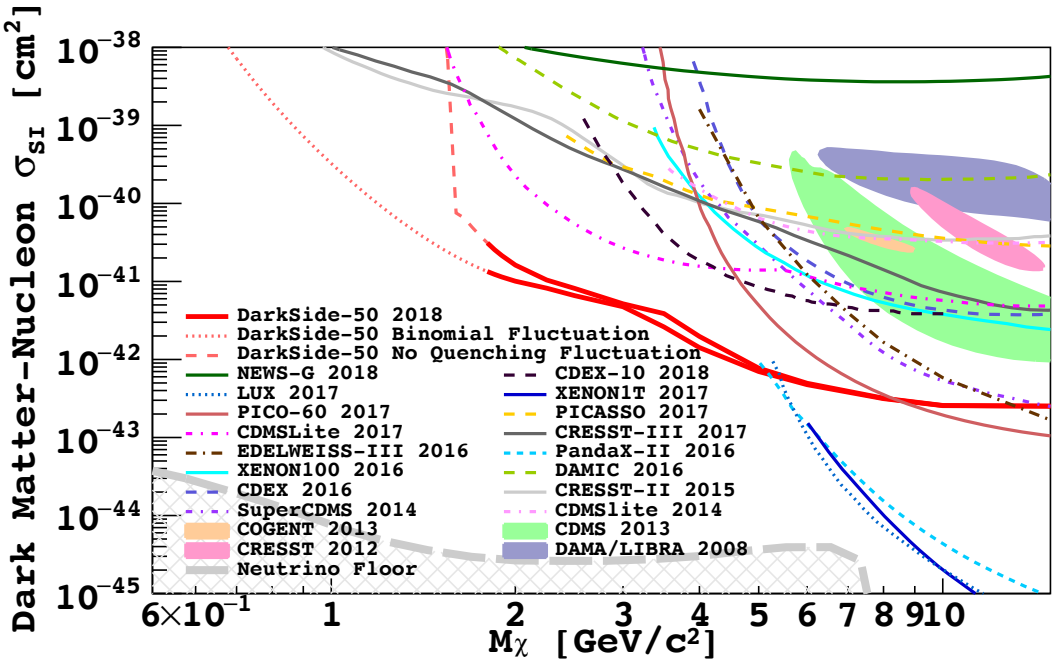

FIG. 17. The 90% C.L. exclusion curves for the binomial fluctuation model (red dotted line) and the model with zero fluctuation in the energy quenching (red dashed line). For masses above 1.8 GeV/c^2 the 90% C.L. exclusion is nearly insensitive to the choice of quenching fluctuation model. Below 1.8 GeV/c^2, the two exclusion curves rapidly diverge because of the effective threshold due to the absence of the fluctuations in the energy quenching process. Without additional constraints on the quenching fluctuations, it is impossible to claim an exclusion in this mass range [61].

Fig. 21. The shape of the DarkSide-20kLAr TPC will be an octagonal prism contained in a vessel made by ultra-pure acrylic (PMMA); the active LAr volume is defined by eight vertical reflector panels and the top and bottom windows of the acrylic vessel. Compared to DarkSide-50 LAr TPC the DarkSide-20k LAr TPC will not present the external copper field cage rings and ITO, but it will use a conductive polymer, poly (3,4-ethylenedioxythiophene) polystyrene sulfonate. The internal walls will be covered with a wavelength shifter, TPB, to convert LAr scintillation light to a wavelength detectable by Silicon PhotoMultipliers (SiPMs). The height of the TPC is 350 cm, for a total LAr volume in the active region of 49.7 t. The LSVwill be substituted by a passive Gd-loaded PMMA shell surrounding the inner detector and between two active AAr layers held at the same temperature and pressure of the TPC . These two detectors will be hosted in a ProtoDUNE-like cryostat [63, 64] that in turns will be surrounded by layers of plastic to shield it by the cosmogenic and radiogenic neutrons coming from the rock of the Hall C. The outer walls of the TPC will sit approximately 2 m away from inner wall of the cryostat. A a 3D representation of the DarkSide-20k is shown in Fig. 19. A schematic view of the veto is reported in Fig. 18. The choice to abandon organic liquid scintillator comes from the need to minimize the environmental impact that experiments could have on underground LNGS operations, but it will carry a lot of advantages from an experimental point of view. Indeed operating the TPC directly in the ProtoDUNE-like cryostat eliminates the need to have a cryostat in proximity of the TPC and then near the UAr this will help to further lower the residual background.

In addition to the ProtoDUNE-like cryostat, (SiPMs) photosensors will constitute the main new feature of DarkSide-20k with respect to DarkSide-50 [62], and have a number of advantages over traditional PMTs: high photon detection efficiency, better single-photon resolution, low bias voltage requirement and they can be arranged into tiles that cover large areas with a fill factor way higher than PMTs'.

For the DarkSide-20k the photosensing unit will be a "photodetector module" (PDM) consisting of a large array of SiPMs; the photodetector modules are located above the anode and below the cathode, assembled in ∼4000 photodetector modules for each windows: a single readout module consists of a 50× 50 mm^2 SiPMtile assembly containing 24 SiPMsof ∼1 cm^2 joined together to form a single light sensing unit. The SiPMtiles are used to form two larger basic mechanical units called the SQuare Board (SQB) and the TRiangular Board (TRB), as shown in Fig. 20. The SQB and TRB have the same edge size of 25 cm. The SQB and TRB are then used to form the full readout octagonal planes. The total number of photon readout channels (top and bottom) is ∼8000. Given the increase in size of two orders of magnitude from DarkSide-50 to DarkSide-20k the collaboration plans to build a prototype detector of intermediate size, DarkSide-Proto

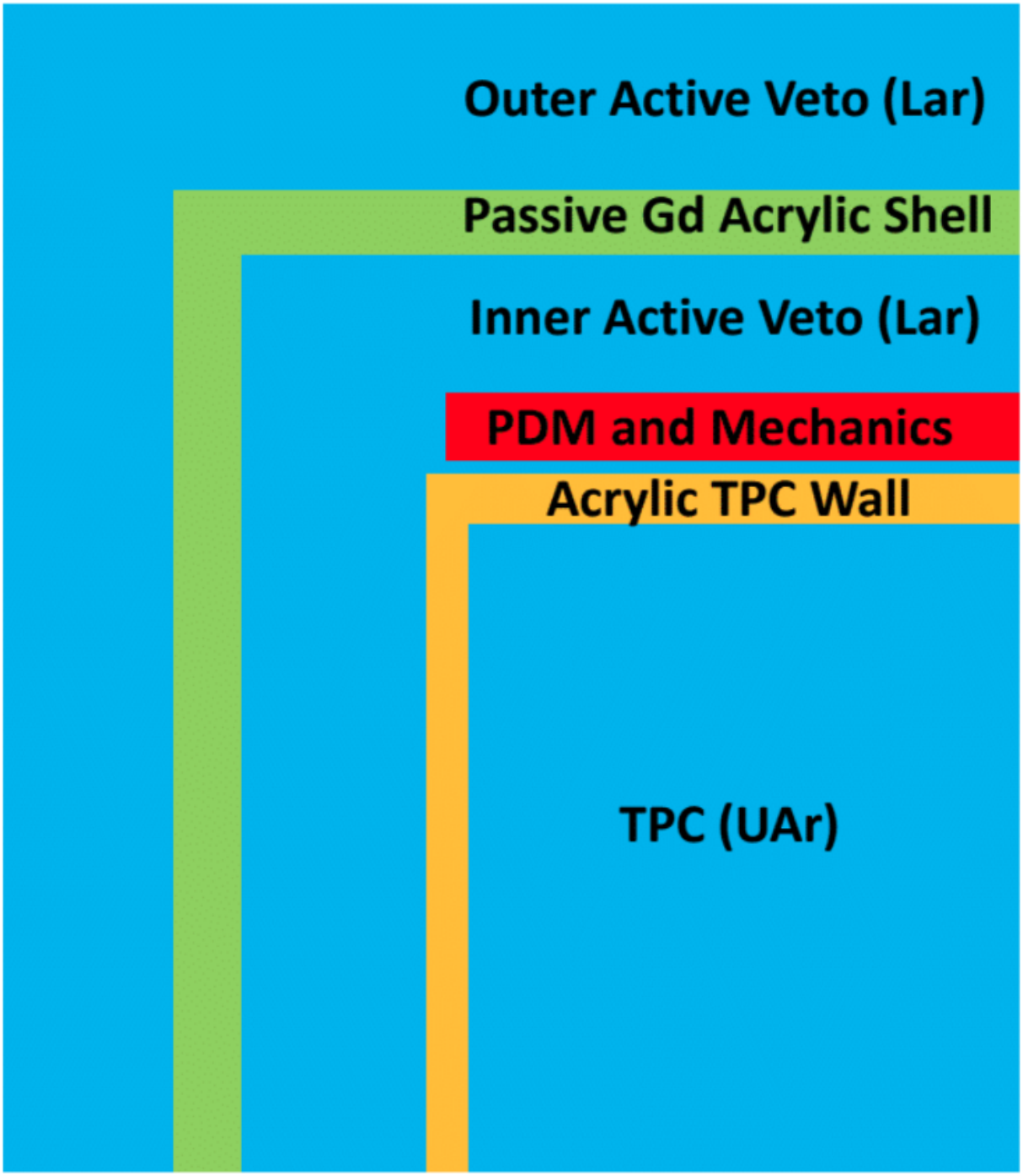

FIG. 18. Schematic conceptual view of the veto detector of DarkSide-20k

(DS-Proto), incorporating the new technologies for their full validation. The choice of the ∼1 ton mass scale allows a full validation of the major innovative technical features of DarkSide-20k mechanical and cryogenic design, integration of the custom photodetector modules with the full read-out electronics and data acquisition chain. [62]

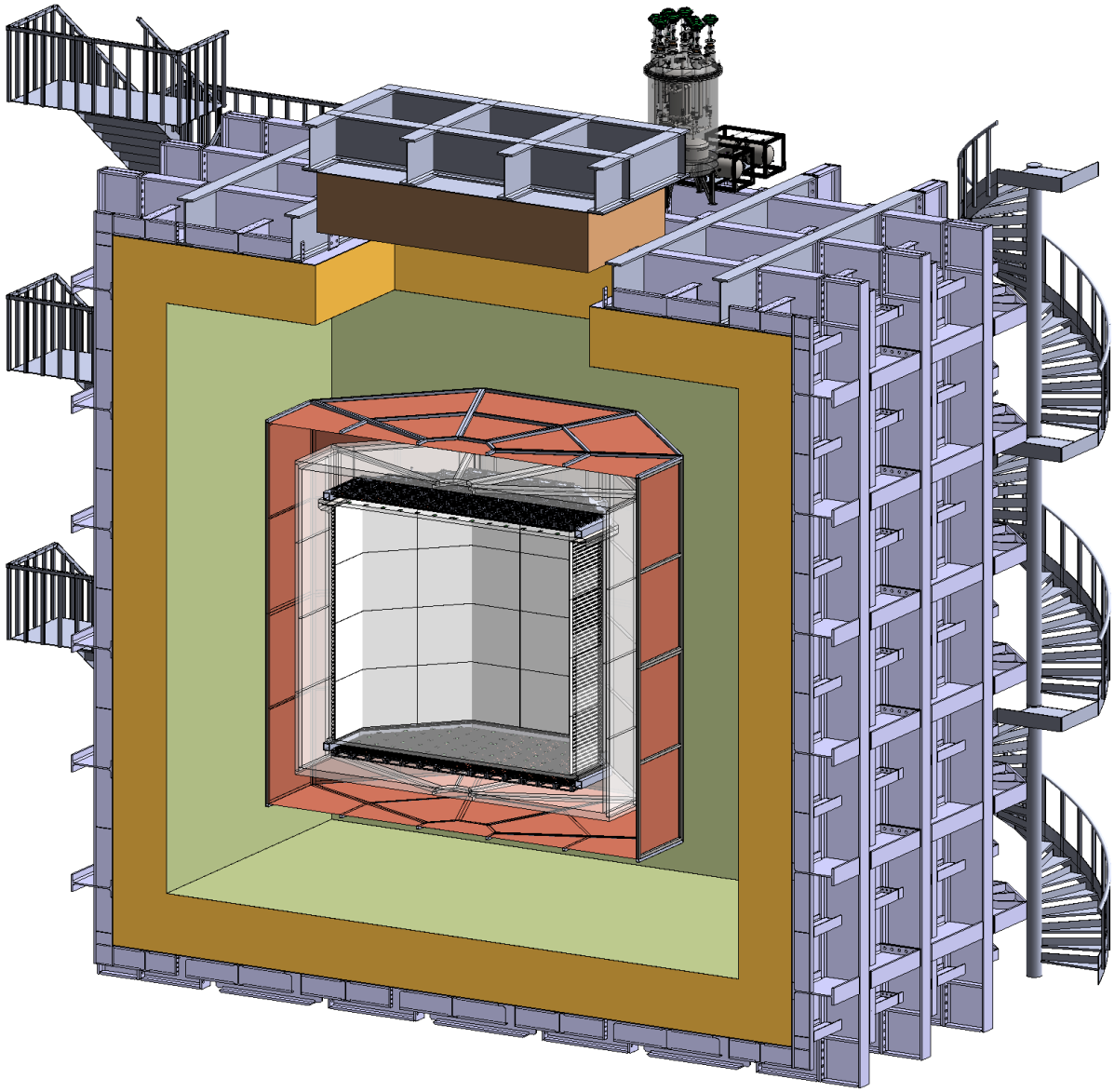

FIG. 19. 3D rendering of the DarkSide-20k LAr TPC and cryostat.

V. DARKSIDE TECHNOLOGY FOR LOW MASS DARK MATTER SEARCHES: DARKSIDE-LOWMASS

The results obtained with the DarkSide-50 experiment lead the sensitivity in dark matter searches in the range $1.8\,\mathrm{GeV}/c^2$ to $6.0\,\mathrm{GeV}/c^2$ [61]. These results were obtained exploiting the very low threshold of DarkSide-50, and specifically by looking at events in the energy range where the S1 signal is absent while the S2 signal is still plentiful. In turn, the extremely low threshold of DarkSide-50 is owed to the low temperature and high purity of the target, to the excellent control of the electrostatics of the LAr TPC, and to the high ionization yield of LAr.

One significant characteristic of the results obtained with DarkSide-50 at low masses is that the leading sources of residual background are all amenable to be suppressed through an appropriate background reduction plan. The most significant contributions come from γ-rays from the PMTs and β-rays from ^{39}Ar and ^{85}Kr dissolved in the target UAr. Thus, the LAr TPC technique is primed to make further, significant advance in sensitivity for the search of low-mass dark matter.

The enabling factors, for the new and more sensitivity campaigns with detectors featuring the DarkSide technology, are the deployment of SiPM-based PhotoDetector Modules (PDMs) and the further refinement

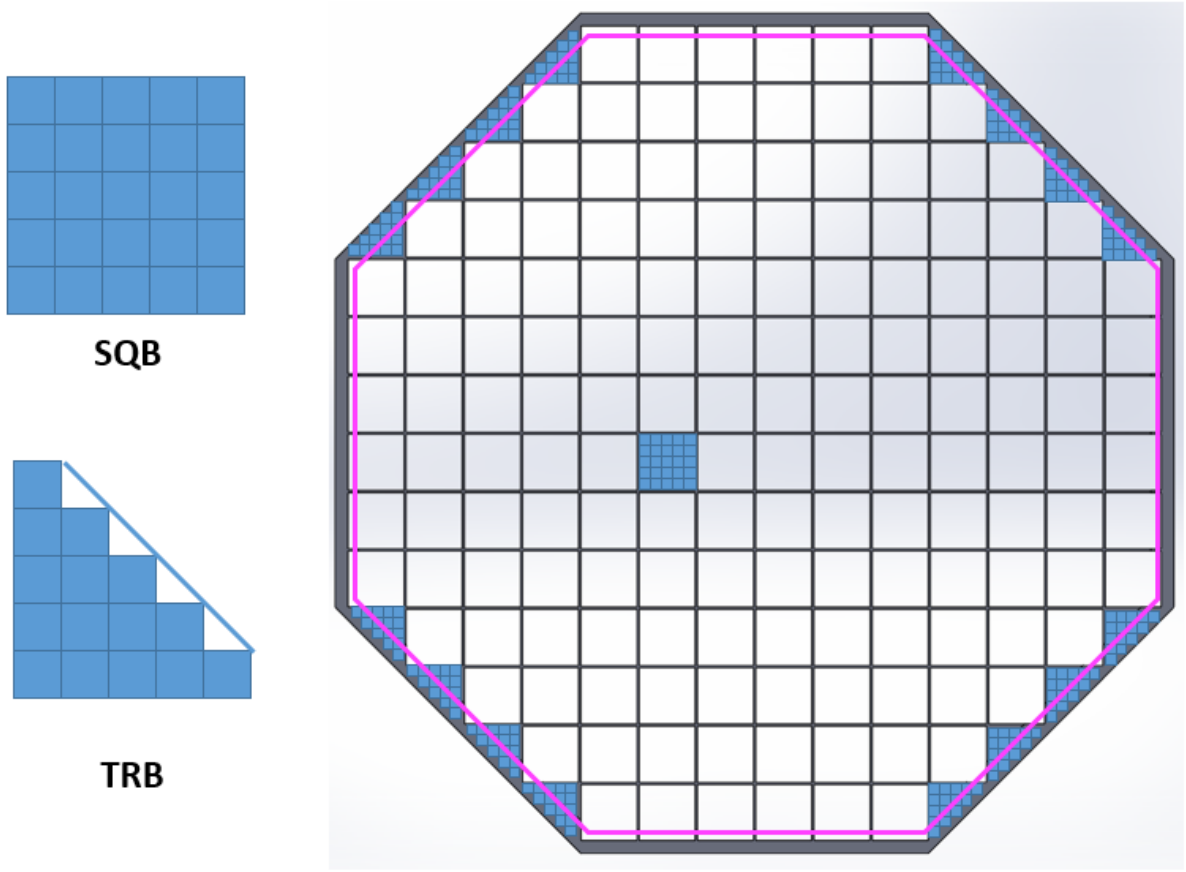

FIG. 20. Pattern scheme for the PDMs. Pink lines indicate the edges of the TPC active volume. A single PDM, the elemental photon readout channel in DarkSide-20k, covers an area of $50 \times 50\,\mathrm{mm}^2$. On the left hand side are shown the patterns of the individual square motherboard, SQB, an array of 5×5 PDMs, covering an area of $25 \times 25\,\mathrm{cm}^2$, and of an individual triangular motherboard, TRB, featuring 15 PDMs arranged in a triangle shape and covering an area of $15 \times 25\,\mathrm{cm}^2$.

of the UAr target material. For the latter, the DarkSide Collaboration is planning to improve drastically the quality of the UAr extracted at the Cortez, Colorado site by eliminating all sources of air infiltration discovered after completion of the DarkSide-50 extraction campaign [55]; the Collaboration is also planning to deploy cryogenic distillation for the removal of ^{85}Kr in both the Urania and Aria plants and for the selective isotopic separation (and rejection) of ^{39}Ar with the Aria plant.

In this Chapter, my goal is to analyze and present the ultimate possible performance of a detector based on the DarkSide technology in the search for low-mass dark matter. Key to any practical deployment will be the processing of the target with the Seruci-I column. Given the expected rate of 10 kg/d for the removal of ^{39}Ar, at a level of a factor 10 per pass, it is prudent to restrict the study to a detector with the approximate scale of $\sim$1 t. Incidentally, this happens to be the scale of the DarkSide-Proto prototype detector, which offers a very solid study case for the start of the determination of the sensitivity of the DarkSide technology for low-mass dark matter searches.

Therefore, this Chapter starts from a detailed examination of the DarkSide-Proto detector. Upon completion, I will review the plans for the ultimate DarkSide-LowMass detector, based on the DarkSide-Proto geometry but endowed with many advanced solution to afford the utmost background suppression.

V.A. The DarkSide-Proto Detector

The objective of the DS-Proto experiment is the construction and operation of a prototype detector of intermediate size ($\sim$1 t), to fully validate the new DS-20k technologies for their integration in both the mechanical and functional aspects. The prototype will be constructed using the materials planned before

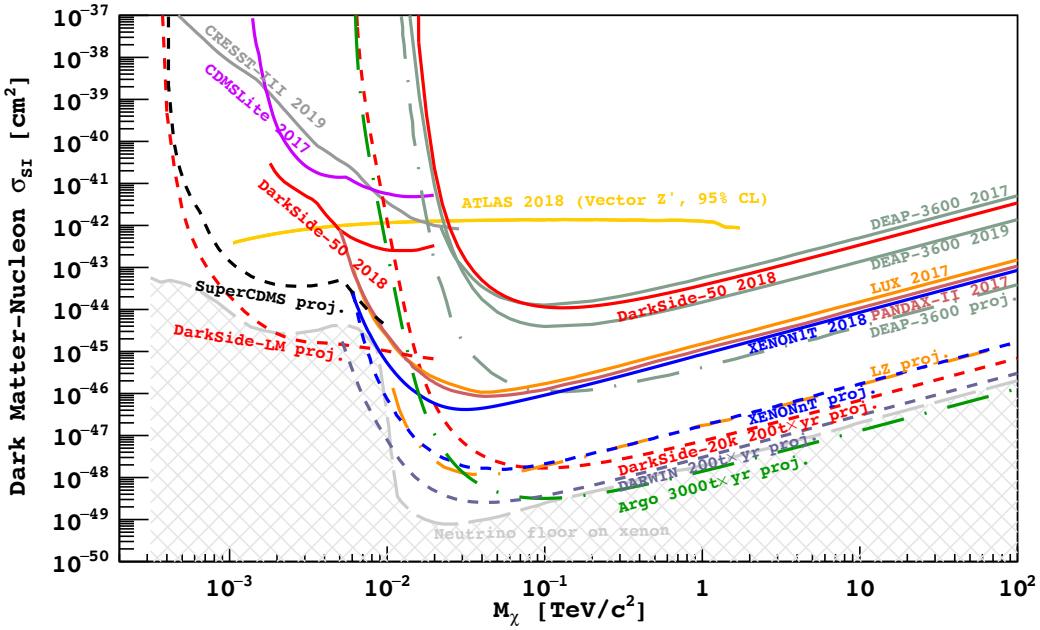

FIG. 21. 90 % C.L. exclusion limits showing leading results from direct (continuous lines, Ref. [52, 53, 56, 60, 61, 65]) and accelerator-based dark matter searches (region above the yellow line [66]) compared with sensitivities of future germanium-, xenon-, and argon-based direct searches (dashed lines, Ref. [67–71] and this work). The "neutrino floor" curve follows the definition of Ref. [72]. The 95% C.L. limit from the ATLAS Experiment is shown for a benchmark model in which Dirac-fermion WIMPs interact with ordinary matter via a vector mediator with coupling strengths to quarks, leptons and WIMPs of 0.25, 0.01, and 1, respectively [73].

screening, in order to accelerate as much as possible the program of mechanical validation. This choice may evolve over time and steer towards the inclusion of screened material as they become available from the general program of validation of materials from DarkSide-20k. Eventually, the most significant components of DarkSide-Proto may be replaced with low background components certified in the process of procurement of parts for the DarkSide-20k construction.

Design of the DarkSide-Proto detector is ongoing at CERN, where its stainless steel cryostat was already delivered in 2018, see Fig. 22. While engineering of the DarkSide-20k detector is still ongoing and not complete, we anticipate that a preliminary design will need to be complete before turning to the construction of DarkSide-Proto. It is intended that the DS-Proto TPC mechanics, comprising all structural elements, including the race track, the reflector panels, the electrodes (anode and cathode), as well as the PDMs will all be built as a scaled-down version of the intended DarkSide-20k detector. Fig. 23 shows the current artist rendering of the DarkSide-Proto detector. The Collaboration expects to turn to the construction of the DarkSide-Proto detector at the beginning of 2020.

Two planes of 185 PDMs will cover the top and bottom of the DarkSide-Proto TPC, for a total of 370 PDMs. When the construction of the TPC of DarkSide-Proto will be completed at CERN, it may be moved to LNGS, to begin the search of low mass dark matter, in a detector geometry configuration still under study. This work is intended to explore different geometry designs to have background as low as possible; of course this can be achieved only through the choice of ultra-pure materials and thanks to cleaning and purification techniques.

At this time, prior to the completion of the engineering of DarkSide-20k at the level necessary for the start of the detailed design of DarkSide-Proto, there are a few essential parameters of the DarkSide-Proto design that are already nearly frozen. DarkSide-Proto should be an octagonal prism LAr TPC with an external edge of the octagon of 30 cm and a nominal diameter of 72 cm. The TPC height of 60 cm will result in a drift length of 58 cm. The nominal drift field of 200 V/cm requires cathode potential of −15 kV and implies a nominal drift of 7 µs. The LAr TPC will operate in a two-phase mode, with a thin gas ullage above the target liquid, as in DarkSide-50.

The top and bottom boundaries of the active volume are two PMMA windows, 5 cm thick, acting as anode and cathode. The inside surface of the windows will be coated with a conductive polymer (replacing the ITO in use for DarkSide-50). A grid, located just below the liquid-gas separation surface, will define sharply the potential below the transition from the electron drift to the electron extraction regions. The distance

FIG. 22. The laboratory space allocated for the DarkSide-Proto assembly at CERN. (Credit: Dr. Hanguo Wang, UCLA.)

from the grid to the top of the liquid phase will be of 3 mm, and the argon ullage will be 7 mm thick, in both cases mirroring the design parameters of DarkSide-20k. Extraction and electroluminescence fields will be operated at 2.8 kV/cm and 4.2 kV/cm as foreseen for DarkSide-20k. The sides of the TPC will be delimited by 16 reflector panels, made of a specular reflector enclosed by a thin PMMA sheet, each of 30 cm width and 30 cm height. On the basis of the DarkSide-50 experience, to optimize light collection the acrylic panels will be coated on the inside surface with a 200 µg/cm^2 layer of the wavelength shifter TetraPhenylButadiene (TPB).

The conceptual design of the cryostat, see Fig. 23, follows closely that of the successful DarkSide-50 cryostat: a 4π vacuum-insulated vessel made of three separate parts, the top assembly, the inner cryostat vessel, and the vacuum insulation vessel. The top assembly is formed by an outer dome and an inner dome mechanically linked, the outer dome of the top assembly has a flange that matches the insulation vessel flange. The inner dome has a flange that matches the inner cryostat vessel.

V.B. Background Sources and Mitigation Strategy

Scintillation properties of LAr allow the discrimination of the kind of particles that deposit energy in it. In particular this is achieved via Pulse Shape Discrimination on the scintillation light (S1), with the result of being able to tag events as nuclear recoils or electron recoils. Here I will present a search for DM with a much lower recoil energy threshold, down to 600 eV$_{\rm nr}$, sensitive to DM masses in the mass range from 0.6 GeV/c^2 to tens of GeV/c^2. WIMPs in this mass range produce nuclear recoils well below 10 keV$_{\rm nr}$, where the efficiency for detecting the S1 signal is low and PSD is therefore not available. Moreover for the very low energy part of the search, S1 is basically non-existent. At low-energies the separation in the values of $f_{\rm prompt}$ for ERs and NRs disappears and they become almost indistinguishable. The required low recoil energy analysis threshold is achieved by exploiting the high gain of the ionization (S2) signal of the dual-phase liquid argon

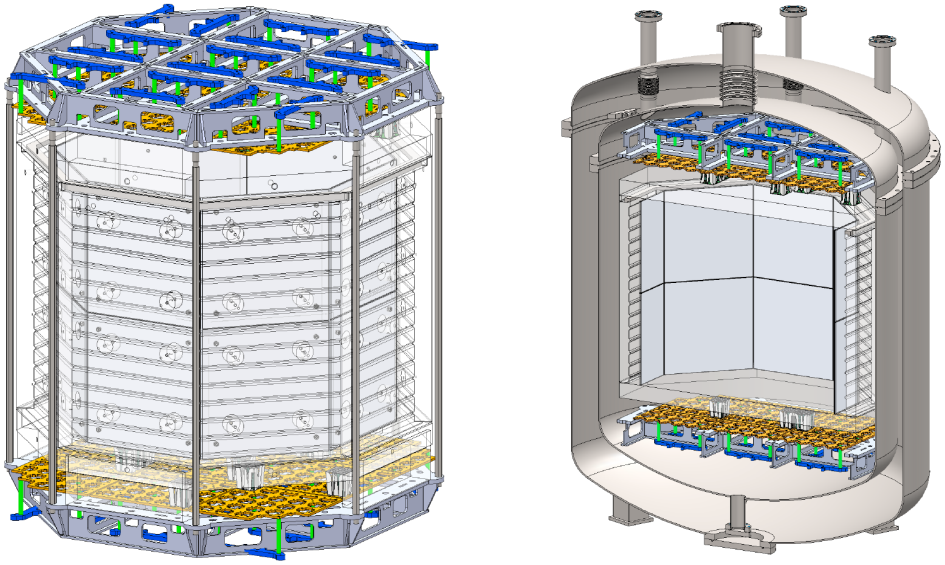

FIG. 23. **Left:** 3D-rendering of the DarkSide-Proto LAr TPC. **Right:** Cutout of the DarkSide-Proto LAr TPC inside its surrounding cryostat. (Credit: Dr. Hanguo Wang, UCLA.)

time projection chamber. Furthermore, in this energy range the mechanisms that produce neutron, causing NRs, are extremely rarer than all the other mechanisms that lead to ERs; indeed neutrons constitute only a minimal fraction of the total background budget. In this context it is clear that the role of an active neutron veto loses its key-role suggesting a revisitation of the geometry of the detector. Before starting to report the results of the simulations of the proposed geometries for the DS-LM, it is useful to give a description of the background sources which produce low energy deposits in the TPC and that have been taken into account during the simulation.

The background sources can be divided into three broad categories:

Internal Background: events due to notable radioactive contaminations dissolved in solution in the active UAr target;

External Background: events originating from radioactivity in the construction materials of the LAr TPC and its cryostat;

Cosmogenic Background: events originating from the residual cosmic ray flux in Hall C of the underground LNGS (depth 3800 m.w.e.).

The radioisotopes directly responsible for internal backgrounds are:

^{39}Ar: is the main source of β-rays in the target material. ^{39}Ar decays generate electron recoils either directly from β decay or indirectly from electron capture producing an X-ray that is subsequently absorbed. Mitigation of this important background is one of the cornerstones of the DarkSide program. The Collaboration has invested very significant effort and resources in the development of the Urania plant for high-throughput extraction of UAr and of the Aria plant for chemical purification and isotopic separation of UAr. The first step in the mitigation strategy will be the elimination of all air leaks that affected the extraction of the UAr target for DarkSide-50. In addition, the Collaboration has the option to utilize the isotopic purification possibly made available with the Seruci-I column to further suppress ^{39}Ar. A description of the Urania and Aria facilities can be found in Ref. [62].

^{37}Ar: is a cosmogenic radioisotope with a 35.04 d half-life [74], whose presence in the UAr target of DarkSide-50 was unexpectedly noticed and reported [55]. Likely, the origin of the ^{37}Ar contamination is due to the fact that the last bottle of the DarkSide-50 UAr contingent reached LNGS from the USA via airplane (having missed the boat that delivered all other bottles). Because of its short half-life, ^{37}Ar was not a major background for the high-mass search in DarkSide-50, and ended up providing a crucial calibration point for the calibration of of the low-mass search [61], through its 0.27 keV and 2.82 keV X-rays emitted after the ^{37}Ar decay. ^{37}Ar is here listed among the internal background sources because, though of cosmogenic origin, its activation likely took place before the UAr target reached the underground Hall C of LNGS.

^{85}Kr: is a fission product with a 10.8 yr half-life [74], whose unexpected presence in the UAr target of DarkSide-50 was hard to recognize and was first reported in Ref. [55]. The suspected source of this contamination is a leak to the atmosphere during the argon extraction process. ^{85}Kr undergoes β

decay to ^{85}Rb, producing β-rayswith a 687 keV end point.

The radioisotopes directly responsible for external backgrounds are:

^{60}Co: is a radioactive isotope with a 5.27 yr half-life [74], which is typically produced in nuclear reactors. Most of ^{60}Co present today is incidentally present in steel, entering the manufacturing process in the form of contaminated scrap. ^{60}Co undergoes β decay to ^{60}Ni. In DarkSide-50, background from ^{60}Co, the activity from the pair of coincident 1.17 MeV and 1.33 MeV γ-rays emitted in the de-excitation of the ^{60}Ni was a major background source.

^{40}K: ^{40}K is a primordial radionuclide, with a 0.012 % natural abundance and a 1.25×10^9 yr half-life [74]. Due to its long half-life, it is one of the most abundant γ-ray emitters naturally present in common detector materials. ^{40}K can undergo three different decay mechanisms: the first and most likely mechanism is a β-decay to the ground state of ^{40}Ca with a Q-value of 1.31 MeV; the rarest of the three decay mechanisms is a β^+ decay to ^{40}Ar; ^{40}K can also undergo electron capture and produce a 1.46 MeV γ-ray that is a powerful source of external background. Additionally, since electron capture reactions remove an atomic electron from one of the atom's inner shells, these reactions may be followed by a 2.66 keV X-ray as the atom relaxes or by the emission of a Auger electron of the same energy: these X-rays are generally not a problem for high mass searches, but do play a role in ultra-low threshold searches such as the ones enabled by the DarkSide technology.

^{232}Th: is a long-lived radioactive isotope naturally present in the crust of the earth with a 1.4×10^{10} yr half-life [74]. Due to its presence in rock, trace amounts of ^{232}Th tend to be present in most metal samples. ^{232}Th spawns a decay chain, which includes a wide array of important radioisotopes, each undergoing one or several decay processes, including emission of γ-rays, α-rays, and neutrons (either directly through fission or (α, n) reactions).

^{238}U: Uranium is naturally present in the crust of the earth with a 99.27 % natural abundance and 4.47×10^9 yr half-life [74]. As a result, most metals mined from the earth will have some trace level of ^{238}U contamination. As in the case of ^{232}Th, the daughters in the decay chain of ^{238}U can produce α-rays, γ-rays, and neutrons either through direct fission or via (α,n) reactions. Given the long half-life of the daughter ^{226}Ra, 1600 yr, it is important to differentiate between the upper and lower parts of the chain.

^{235}U: Much like ^{238}U, ^{235}U is a naturally occurring isotope of uranium with a 4.47×10^9 yr half-life [74] and is nearly inevitably present in trace amounts of metal samples. Although it is always present in smaller concentrations than ^{238}U, the ^{235}U decay chain contains higher energy α-rays which are an important source of neutrons from the subsequent (α,n) reactions. ^{235}U can also undergo spontaneous fission but the main product of the ^{235}U decay chain is still given by low energy γ-rays.

Other than ^{37}Ar, thoroughly discussed above, cosmogenic backgrounds do not play an important role in the determination of the ultimate sensitivity of the DarkSide technology for low-mass dark matter searches.

V.C. Background Simulation and Analysis

The goal of this work is to parse the possible geometries for a future detector featuring the DarkSide technology to optimize the sensitivity to low mass dark matter WIMP-like particles. The first step of this study is to prepare simulations which take into account all the features of the geometry of the detector, the activity of the radioisotopes of interest, how they decay and interact inside each of the components of the detector. The simulations have been produced using G4DS, a Geant4-based toolkit developed for DarkSide. The Geant4 package provides a rich set of particle generators, detailed geometry descriptions, and tuned physical processes. The G4DS toolkit integrates the full optical propagation of photons produced by scintillation in liquid argon and by electroluminescence in gaseous argon [75]. Simulations based on G4DS can track all generated photons until they either are detected in the PDMs (or adsorbed in some material and lost). For this work, I used the G4DS package to generate a large number nuclear decays of the radioisotopes mentioned above for every major detector component. It is paramount to underline that the G4DS package was throughly tested, in the context of the low-mass searches, with the DarkSide-50 campaign [61]: the end result is perhaps the only instance of a low-mass search whose spectrum is almost completely understood and justified in terms of known radioactive contaminations, see also Fig. 26.

The final result of the analysis procedure is the spectrum of ionization electrons, N_{e^-}, generated by background events that pass all the WIMP selection cuts. Then the spectra are analyzed and compared with those expected for WIMP interactions to determine the sensitivity of the detector configurations under consideration. In the next sections I will illustrate the major steps of the analysis procedure.

The first step of the analysis process is the event reconstruction. For each event the interesting output variable of the G4DS simulation consists of energy clusters, deposited by the decay products in the active

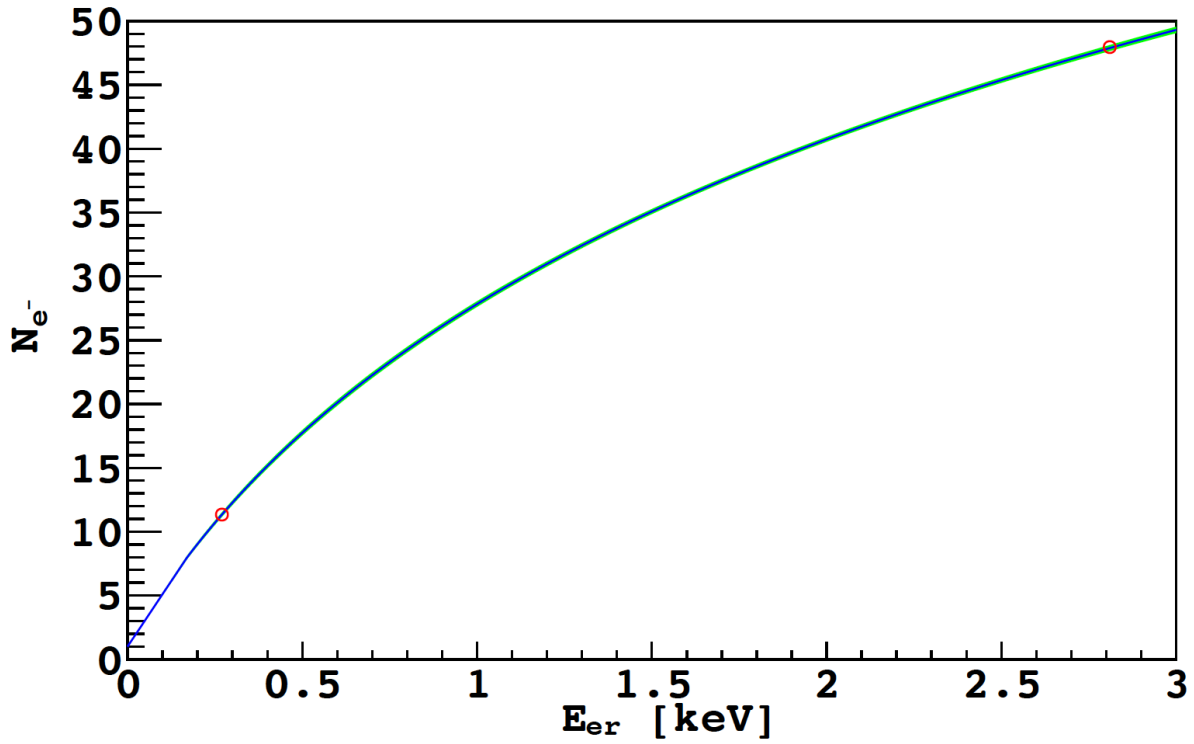

FIG. 24. Calibration curve used to convert electron recoil spectra to ionization spectra. (Credit:Ref. [79]).

volume of the LAr TPC. A cluster is defined as one or more energy deposits which occur at a distance not greater than 2 mm on the z-axis and within a 2 µs time window, opened at the time of the first energy deposition. The clustering is applied in order to minimize the impact of artificial discretization performed by Geant4, which treats continuous energy losses (like ionization) as successive finite steps. The only variables needed for the analysis henceforth are the energy and position of each cluster. In particular the position is calculated as the center of mass of the deposits, weighted with their individual energy deposit amount.

That said, in a real experiment what we actually measure directly are not the variables just mentioned. The observation relies on the detection of the secondary scintillation light, S2, produced by the electrons through a process of electroluminescence while crossing the gas ullage above the active target volume.

To convert energy clusters in number of electrons, we rely upon the conversion curve show in Fig. 24, which allows us to establish a correspondence between the energy measured from S2 signal and average number of electrons required to generate said signal have generate it. Below 8 N_{e^-}, it is assumed there is no recombination and a straight line that intersects $N_{e^-} = 1$ with a slope determined by the ratio of the number of excitations to ionization, $N_{ex}/N_i = 0.21$, measured in ref. [76] and the work function measured in ref. [77]. Above this point, the effects of recombination are included by fitting the Thomas-Imel model [78] to the mean N_{e^-} measured for the 2.82 keV K-shell and 0.27 keV L-shell lines from the electron capture of ^{37}Ar. In order to get good agreement between the model and data, we multiply the model by a scaling factor, whose best-fit value shifts the curve up by 15 % This scaling factor can be interpreted as the agreement between our measured N_{ex}=N_i and work function and the literature values. The green band shows the statistical uncertainty of the fit.

To reproduce the effect of the detector's finite resolution, we perform a rough event reconstruction applying a gaussian smearing on x-y position reconstructed via the S2 signal, given the resolution expected by SiPMs at 2 cm.

After this first step, we apply the following cuts, aimed at the removing events with features incompatible with WIMP-like interactions.

Single scatter cut: we expect WIMPs to produce single interactions in the active volume of the detector, due to their low scattering cross-section. All events with more than one identified scatter are therefore rejected, as likely originated by interactions induced by γ-rays.

Fiducial Cut: one of the main source of background is constituted by radioisotopes present in the material of which the detector is made, as well as the wall LAr TPC that is in direct contact with UAr target. With this cut in the x-y plane, we discard events taking place near the surface of the LAr TPC. In

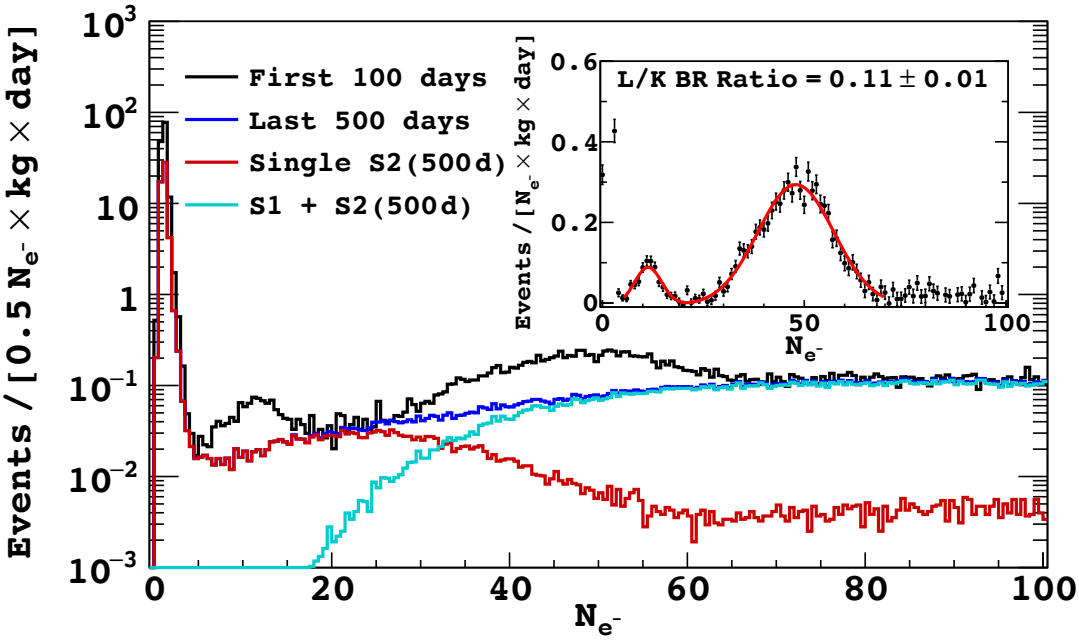

FIG. 25. Spectrum showing cosmogenic ^{37}Ar contributions and their decay as discussed in the text. Black: first 100 days of present exposure. Dark blue: last 500 days. Red and cyan show respectively the contributions to the dark blue spectrum from events with only an S2 pulse and from events with a single S1 and a single S2 pulse. Inset: normalized difference of black minus dark blue, showing the two peaks from ^{37}Ar decay. (Credit: Ref. [61].)

particular, we reject all events whose vertex is reconstructed within a 5 cm distance from the edges of the LAr TPC.

Consistency Cut: With this method we also reject a class of small number of events that have large S1 pulse, even when accompanied by an abnormally low S2 pulse that would, on its own, fall in the region of interest. These events tend to occur near the wall of the LAr TPC, and therefore their largest majority of them is independently rejected by the fiducial cut.

The residual fiducial mass of UAr, following the application of the cuts discussed above, is 267 kg.

To obtain the final N_{e^-} spectra we need to normalize the background spectra generated through G4DS, based on the expected activities of the radioisotopes for the UAr target and for the construction materials of the detector. In order to accomplish this result it is crucial to make correct and realistic assumptions on the radioactive budget for the materials composing the detector. We heavily rely upon the DarkSide materials database, which details the activities of components used in DarkSide-50 and for the preliminary selection of components of DarkSide-20k.

Before introducing the conceptual geometries for low-mass dark matter detector based on the DarkSide technology it will be interesting spend some words on the electron excess observed in the spectrum of N_{e^-} of DarkSide-50, see Fig. 26 between $4\,e^-$ and $7\,e^-$. Since the detection of the S2 only signal is sensitive to single electrons, the electron train background constitutes a serious limitation to this technique. This phenomena has been also observed in XENON10 experiment, as referred in [50], its origin is ascribed to the thermalization and trapping of un-emitted electrons below the liquid xenon surface, with eventual emission on longer (¿¿10 µs) timescales. A possible cause of the electron train background can be found in [80], the explanation model starts from the Shottky barrier model: as an electron approches a dielectric boundary, that is held at a constant potential, the force due to its image charge results in an energy barrier. The force driving the electron toward the barrier is that due to the applied external electric field. The energy distribution of drifting electrons can be derived from Boltzman equations, as referred in [80]. One finds that on average electrons retain thermal energies for electric fields below about 50 V/cm. By 2.8 kV/cm and 4.2 kV/cm the average energy of electrons is about a factor 10 above thermal. In this basic model is completely missing the fact that electrons scatter significantly when they travel through matter and that their trajectories are random and only slightly biased by the applied electric field. In this scenario electrons could undergo to a series of situations: they could fail to cross the barrier and will most likely continue to scatter or may eventually thermalize just below the surface, or they could escape into the gas too. Including these possibilities in the basic Shottky model one finds that at an electric field of about 5 kV/cm, the mean free path between collisions is approximately of 10 nm and the saturated drift velocity is nearly 3000 m/s.Taking

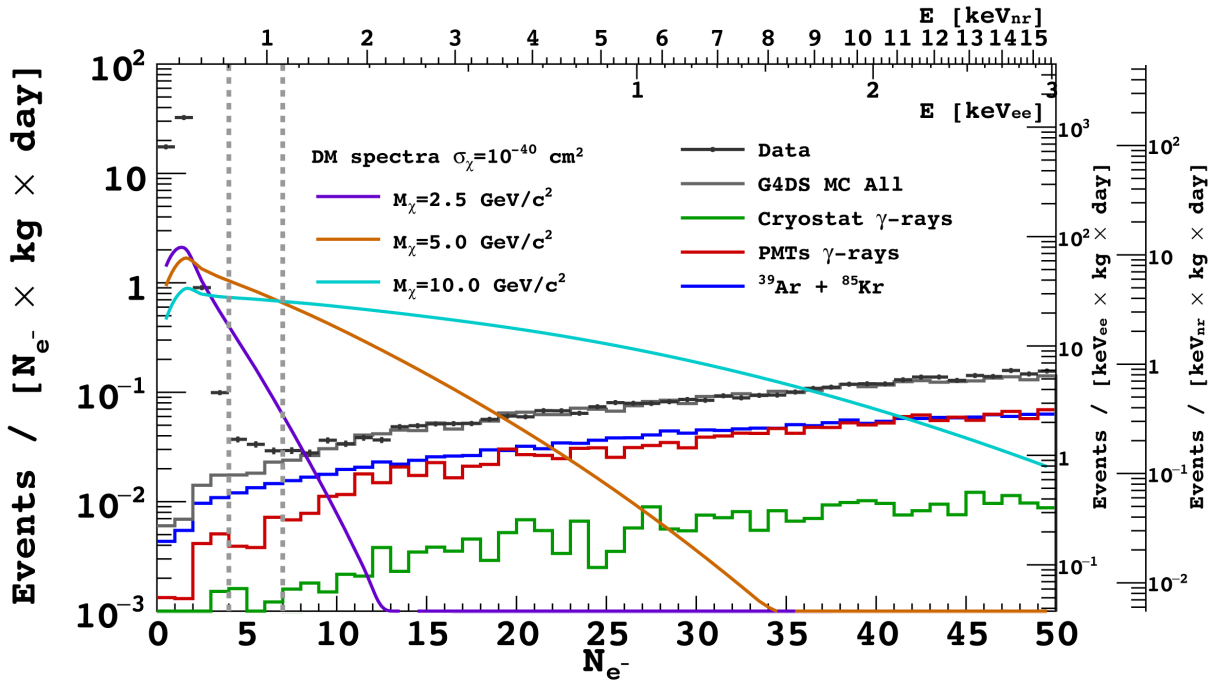

FIG. 26. The DarkSide-50 N_{e^-} spectra at low recoil energy from the analysis of the last 500 days of exposure compared with a G4DS simulation of the background components from known radioactive contaminants. Also shown are the spectra expected for recoils induced by dark matter particles of masses 2.5, 5, and 10 GeV/c^2 with a cross section per nucleon of 10^{-40} cm^2 convolved with the no energy quenching fluctuation model and detector resolution. The y-axis scales at right hand side are approximate event rates normalized at $N_{e^-} = 10\,e^-$. (Credit: Ref. [61].)

into account the lattice constant of Xe this suggests a typical relaxation time between collisions of about 3 ps. Suppose that a typical electron could experience up to 10 additional collisions between successive attempts to escape the liquid, the emission process would be complete in less than 1 ns, which is consistent with time observation of electron train. According to this model a possible mitigation strategy for electron train is to have a more intense extraction field to lower the probability that electrons remain in the boundary region and be thermalized. The value for which the effect is reduced to a factor 50 is 7 kV. This solution from one side should give a great improvement to the S2 only detection technique, but from the other side should be very challenging from technical point of view. A series of studies are on going to find possible solutions to reduce the effect.

V.D. Specific Detector Configurations

In this section I will introduce and describe several conceptual geometries for a low-mass dark matter detector based on the DarkSide technology. I will start from the simplest example, and will gradually move to consider more evolved and efficient schemes by introducing novel arrangements devised upon observation of the limitations of the previous scenario. For ease of discussion, the different scenarios are enumerated in a list. I will consider for each case the contribution from the backgrounds that are deemed relevant. For example, I will neglect any contribution from ^{85}Kr: notwithstanding its important role in setting the ultimate background in DarkSide-50, the Collaboration has made a solid case that ^{85}Kr can be completely removed. Similarly, I will make reasonable assumptions on the strategies that can be deployed for the removal of the major sources of background, leading from one step to the other the development of a "ultimate" detector for the discovery of low-mass dark matter with the DarkSide technology.

DarkSide-Proto in its first configuration: in the the first scenario, the DarkSide-Proto detector is installed inside the Liquid Scintillator Veto (LSV) tank of DarkSide-50, filled for the purpose with an ultra-pure water buffer (no liquid scintillator). The LSV is in turn contained within the CTF water tank, which is also filled for the purpose with an ultra-pure water buffer. Dimensions and characteristics of the LSV and CTF containers and associated veto detector can be found in Ref. [81]. The DarkSide-Proto detector is installed inside a double wall cryostat vessel (assuming 1.25 cm and 1.75 cm thickness for the internal and external stainless steel wall). The thickness of the PMMA electrode

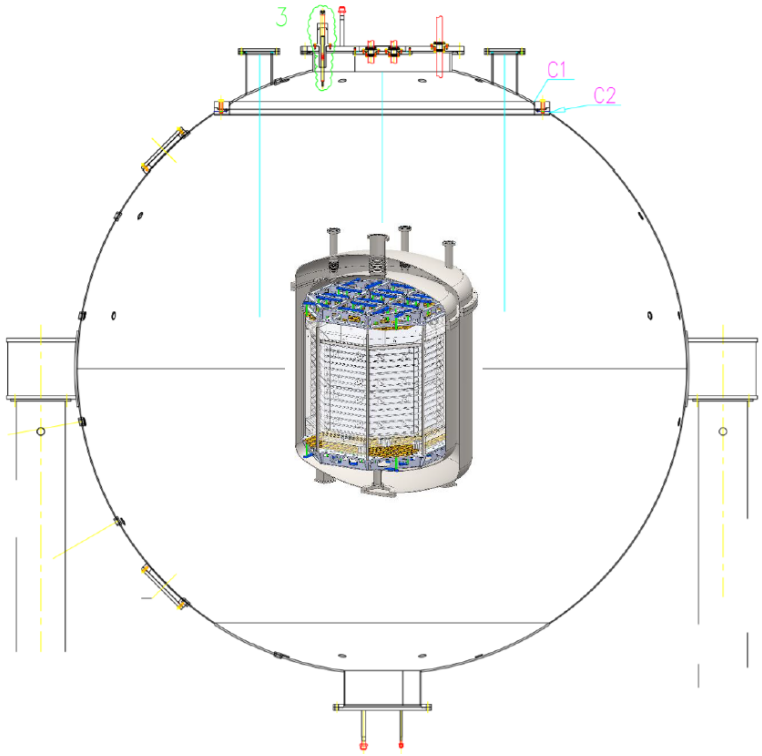

FIG. 27. Schematic configuration of the DarkSide-Proto detector. From outside to inside, shows are the stainless steel sphere enclosing the LSV, the small cryostat, and the LAr TPC.

windows and reflector walls is 5 cm. The schematic configuration for this arrangement is shown in Fig. 27. The rationale for the consideration of this scenario is the ease in its possible implementation: the DarkSide-Proto detector will be built and operated at CERN in preparation for DarkSide-20k, and the LSV has been in operation at LNGS since 2008. The key components and materials of the detector, impacting the background and sensitivity, are listed in Table II.
The radioactive contaminations taken in consideration are listed in Table III. The spectrum obtained is shown in Fig. 28: it is evident that the major contribution for the radioactivity comes from the activity of ^{39}Ar of the UAr target, which is assumed to be the same (0.73 ± 0.11) mBq/kg measured in DarkSide-50 [55]. With this level of activity, ^{39}Ar contributes a background that is one order of magnitude higher than that of SiPMs. The PMMA gives the lowest contribution to the background among the leading sources.

DarkSide-Proto in its second configuration: the results obtained with the first configuration lead us naturally in the direction of proposing, for the second scenario under consideration, a small modification

TABLE II. Components and materials of the DarkSide-Proto detector.

Components	Material	Mass	Units
Cryostat	Stainless Steel	2300	[kg]
Reflector	PMMA	89	[kg]
Windows	PMMA	67	[kg]
PDMs	Various	370	
Target	UAr	260	[kg]

TABLE III. Specific activities for the materials of the DarkSide-Proto detector in its two configurations.

Material	Cf. #1	Cf. #2	^{238}U	^{226}Ra	^{235}U	^{232}Th	^{40}K	^{60}Co	^{39}Ar	Units
Stainless Steel	✓	✓	2600	2600	26	1400	<3700	<650	0	[µBq/kg]
PMMA	✓	✓	120	120	1.2	41	0	0	0	[µBq/kg]
PDMs	✓	✓	4200	4400	0	3400	<1900	<82	0	[µBq/PDM]
UAr	✓	✗	0	0	0	0	0	0	730	[µBq/kg]
UAr	✗	✓	0	0	0	0	0	0	7.3	[µBq/kg]

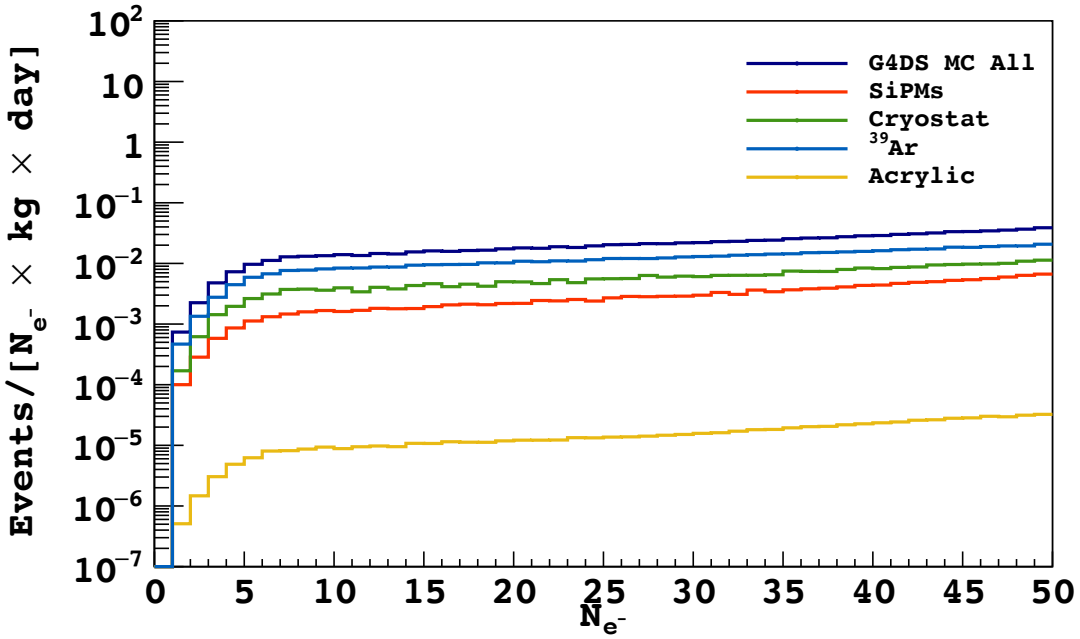

FIG. 28. Background spectrum for the DarkSide-Proto detector in its first configuration. See text for discussion.

of the first scenario, with operation of the same detector with a UAr target depleted in ^{39}Ar by two additional orders of magnitude, The abatement of the ^{39}Ar activity is made possible by the operation of the Seruci-I cryogenic distillation column, described in Ref. [62]. The abatement by two additional orders of magnitude is now only compatible with the expected purification rate of 10 kg/d for an expected depletion of 10 per pass, but it is also compatible with the small re-activation rate due to the transport of the UAr target from the Seruci site to LNGS [62]. The key components and materials of the detector, impacting the background and sensitivity, are still listed in Table II.

The radioactive contaminations taken in consideration are listed in Table III. The spectrum obtained is shown in Fig. 29: in this case, having suppressed the ^{39}Ar contribution, the dominant activity becomes that from the stainless steel of the cryostat.

DarkSide-LowMass in its first configuration: given the leading residual contribution from the stainless steel of the cryostat in the previous step, in the next step I will consider the complete removal of the cryostat. This can be achieved by inserting the LAr TPC at the center of a larger cryostat with a liquefied AAr fill (possibly instrumented as a veto detector, although this is not exploited in the current analysis), which allows the substitution of the cryostat with a ultra-low background containment vessel for the UAr target. For simplicity, the choice is to utilize the same technology under development for DarkSide-20k, which foresees the use of a sealed PMMA serving at once as containment vessel for the UAr target and structural element for the LAr TPC. This detector, DarkSide-LowMass, is inserted at the center of a membrane cryostat of 5 m diameter and 6 m height. With this choice of dimensions, the thickness of the liquefied AAr buffer is of 2 m. The schematic configuration for this arrangement is shown in Fig. 30. The key components and materials of the detector, impacting the background and sensitivity, are listed in Table IV.

The radioactive contaminations taken in consideration are listed in Table V. We assume for ^{39}Ar activity the same suppression of two orders of magnitude below the value achieved in DarkSide-50 that was considered for the previous case. The spectrum obtained is shown in Fig. 31: the activity from the steel of the cryostat becomes comparable to that of the PDMs.

TABLE IV. Components and materials of the DarkSide-LowMass detector in its first configuration.

Components	Material	Mass	Units
Cryostat	Stainless Steel	13 000	[kg]
Reflector	PMMA	89	[kg]
Windows	PMMA	67	[kg]
PDMs	Various	370	[number]
Target	UAr	260	[kg]

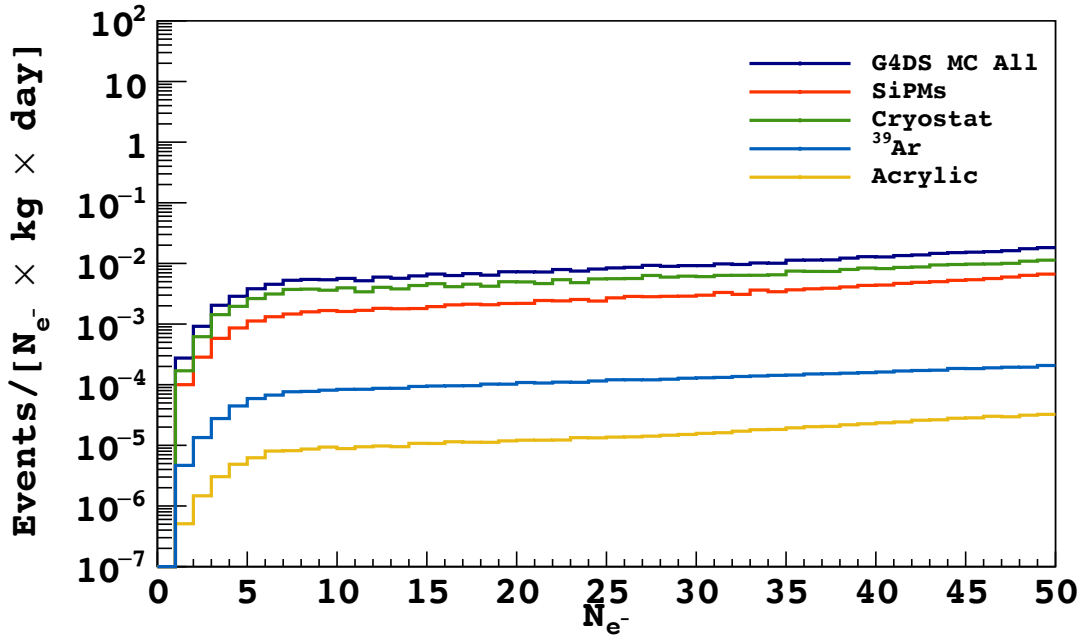

FIG. 29. Background spectrum for the DarkSide-Proto detector in its second configuration. See text for discussion.

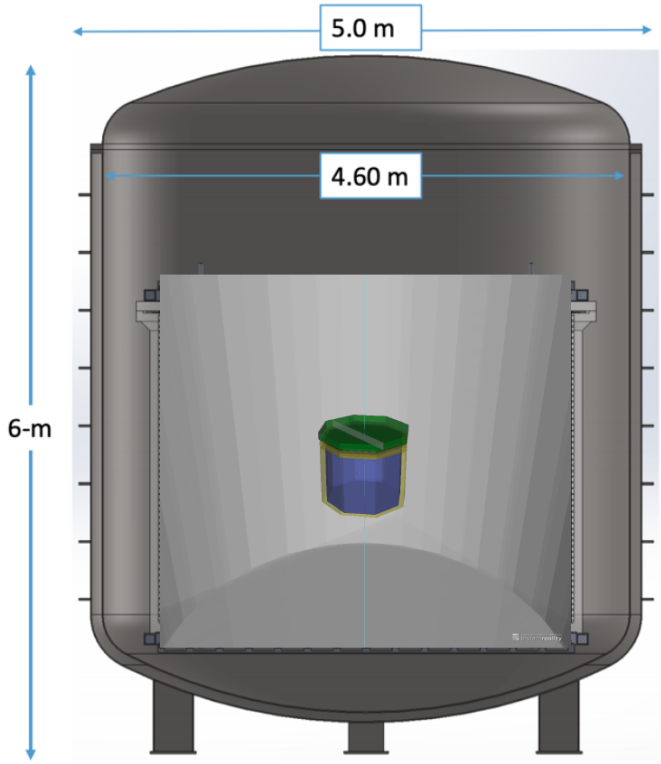

FIG. 30. Schematic configuration of the DarkSide-LowMass detector, with the LAr TPC detector surrounded by a large cryostat with a liquefied AAr fill.

DarkSide-LowMass in its second configuration: the results of the previous step prompt us to take

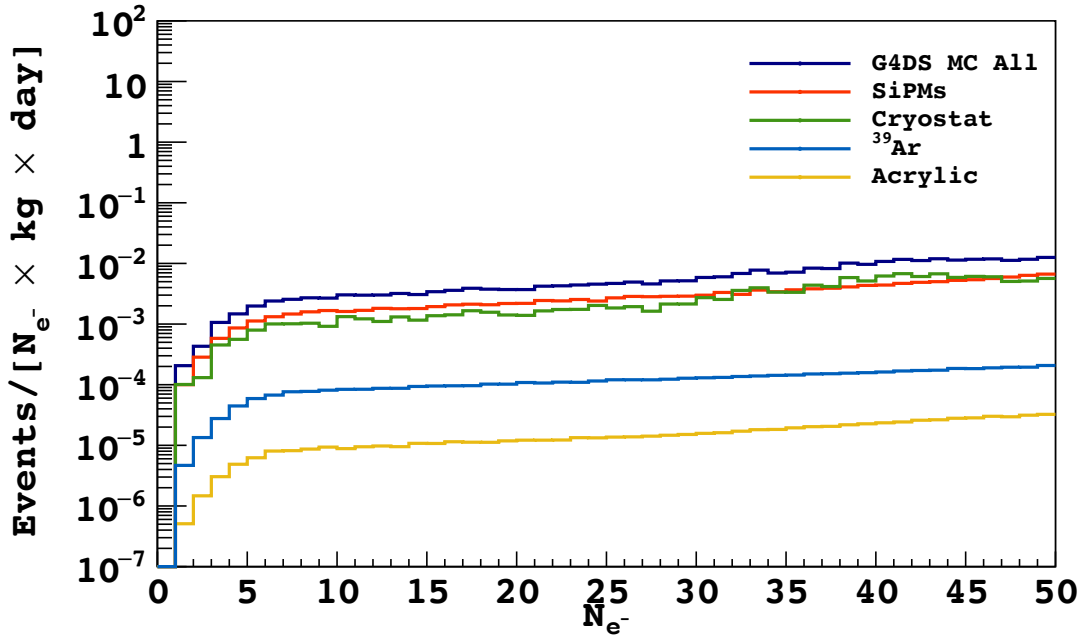

FIG. 31. Background spectrum for the DarkSide-LowMass detector in its first configuration. See text for discussion.

further measures to reduce the background from the large steel cryostat. This can be achieved by imagining the operation of the DarkSide-LowMass detector in a much larger cryostat, such as it would be possible by placing DarkSide-LowMass at the center of a DUNE cryostat. This idealization allows use to remove from consideration the external background from the cryostat. The abatement of the background from the PDMs is more tricky. Given the need to deploy a solution in the near - 2 to 5 years - future, the safe assumption is that the intrinsic activity of PDMs will not see drastic, order-of-magnitude improvements. I will still make the assumption that some improvements are possible for the activity of the PDMs- for example, I consider a reduction of the divider chain resistors [82], which are the leading contributors of background, from 52 to 8 per PDM, and a reduction of the masses (or radioactivity) of all the other components by a factor of 2. These two limited assumptions seem justified given the excellent progress of the R&D effort ongoing at LNGS, but are not sufficient to obtained the desired suppression of background. Still, the contribution from the PMMA vessel can be strongly reduced by substituting high purity PMMA with the ultra-pure PMMA developed for the JUNO detector [83] and by increasing the thickness of said PMMA, from 5 cm to 15 cm, so that the PMMA electrode windows can serve as moderators for the low-energy γ-rays source by the PDMs. The key components and materials of the detector, impacting the background and sensitivity, are listed in Table VI.

The radioactive contaminations taken in consideration are listed in Table VII. The ^{39}Ar activity remains at same suppression of two orders of magnitude below the value achieved in DarkSide-50 that was considered for the previous two cases. The spectrum obtained is shown in Fig. 32, giving our best - and reference, from now on - result.

V.E. Signal Analysis

The final step of the analysis consists in estimating the upper limit on WIMP-nucleon scattering cross-section corresponding to the best and reference scenario, that of the DarkSide-LowMass detector in its second

TABLE V. Specific activities for the materials of the DarkSide-LowMass detector in its first configuration.

Material	Cf. #1	^{238}U	^{226}Ra	^{235}U	^{232}Th	^{40}K	^{60}Co	^{39}Ar	Units
Stainless Steel	✓	2600	2600	26	1400	<3700	<650	0	[µBq/kg]
PMMA	✓	120	120	1.2	41	0	0	0	[µBq/kg]
PDMs	✓	4200	4400	0	3400	<1900	<82	0	[µBq/PDM]
UAr	✓	0	0	0	0	0	0	7.3	[µBq/kg]

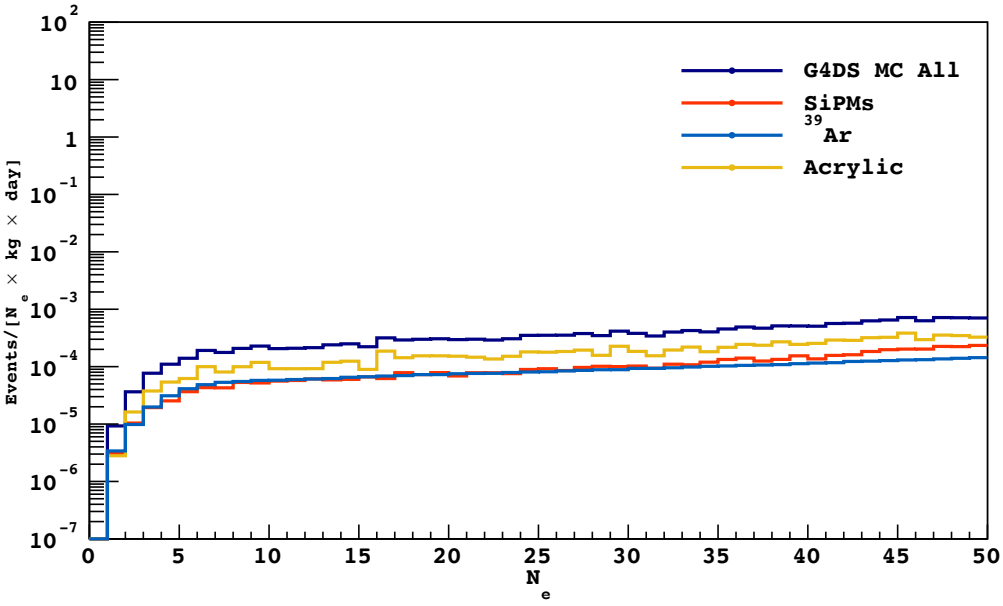

FIG. 32. Background spectrum for the DarkSide-LowMass detector in its second configuration. See text for discussion.

configuration. This is achieved by comparing the calculated background with the expected N_{e^-} spectrum due to WIMP interactions, and determining the combinations of WIMP masses and cross sections that are incompatible with the calculated background.

The absolute scale of the signal was determined in the context of the low-mass experiment performed with DarkSide-50. The ionization yield for nuclear recoils was reconstructed as per Fig. 33. The figure shows all the ionization yield measurements for argon in the region of interest as a function of the reduced energy ϵ. Direct measurements of the nuclear ionization yield were performed by the SCENE experiment [84, 85] and by Joshi *et al.* at 6.7 $\mathrm{keV_{nr}}$ [86]. The measurements by ARIS [87] experiment are converted to ionization yield using the DarkSide-50 calibration data, where both scintillation and ionization signals are present, and using optical models of both detectors. The red curve represents the fit of ionization yield from the Bezrukov model [88] to ^{241}AmBe and ^{241}Am^{13}C data. The shaded region below the curve represents the $-1\,\sigma$ uncertainty from the fit. The upper boundary of the shaded region is drawn to represent the ionization predicted using the same model but fitting to the neutron beam scattering measurements. The difference between the curve and the upper boundary is taken as our systematic uncertainty included in the profile likelihood analysis.

The energy scale for low-energy electrons was determined thanks to the use of the ^{37}Ar X-rays, see Fig. 25.

The signal of the dark matter is obtained from the standard isothermal WIMP halo model, with the following parameter: $v_{\mathrm{escape}} = 544\,\mathrm{km/s}$, $v_0 = 220\,\mathrm{km/s}$, $v_{\mathrm{Earth}} = 232\,\mathrm{km/s}$, and $\rho_{\mathrm{dm}} = 0.3\,\mathrm{GeV}/(c^2\,\mathrm{cm}^3)$. As for the experiment signal, since we have only a simulation of the detector, we don't have knowledge of the width of the ionization distribution of nuclear recoils and of measurements in liquid argon in the energy range of interest. For this reason we'll assume a model for LAr that allows fluctuations in energy quenching, ionization yield, and recombination processes. Moreover we consider systematic uncertainties of the nuclear recoil ionization yield and the single electron S2 yield and an uncertainty of 15 % on the background rates from SiPMsand Acrylic, and of 3 % for ^{39}Ar. The upper limit on the WIMP-nucleon scattering cross-section is then extracted matching the simulated N_{e^-} spectrum using a binned profile likelihood method based on a frequentist significance [89, 90]. The signal region is defined using a threshold of $4\,e^-$, determined by the approximate end of the trapped electron background spectrum in DarkSide-50 [61], thus allowing sensitivity

TABLE VI. Components and materials of the DarkSide-LowMass detector in its second configuration.

Components	Material	Mass	Units
Reflector	PMMA	300	[kg]
Windows	PMMA	310	[kg]
PDMs	Various	370	[number]
Target	UAr	260	[kg]

TABLE VII. Specific activities for the materials of the DarkSide-LowMass detector.

Material	Cf. #2	^{238}U	^{226}Ra	^{235}U	^{232}Th	^{40}K	^{60}Co	^{39}Ar	Units
PMMA	✓	3.7	3.7	0	5.3	<2600	0	0	[µBq/kg]
PDMs	✓	570	170	20	140	<360	<22	0	[µBq/PDM]
UAr	✓	0	0	0	0	0	0	7.3	[µBq/kg]

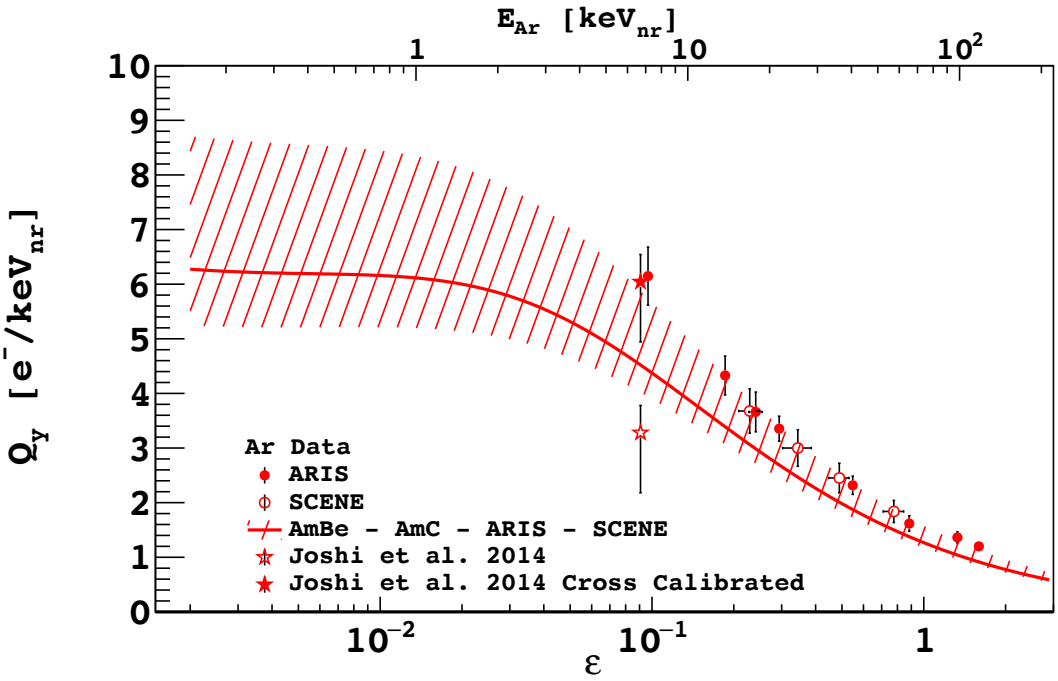

FIG. 33. The measured ionization yield, Q_y, for nuclear recoils in LAr as a function of the reduced energy parameter, ϵ. Also shown is the Bezrukov model [88] fit to the ^{241}AmBe and ^{241}Am^{13}C data. (Credit: Ref. [61].)

to the entire range of WIMP masses explored in DarkSide-50.

V.F. Physics Potential

Fig. 34 shows the 90 % C.L. exclusion curves projected for the 1 and 3 yr exposure of DarkSide-LowMass in its second configuration. For masses below 8 GeV/c^2, DarkSide-LowMass can increase of about 2 orders of magnitude the sensitivity (and discovery power) of DarkSide-50, exploiting the technological advances under development for DarkSide-20k. Notably, the DarkSide-LowMass result could allow to nearly completely sweep the discovery region available at low masses, prior to the onset of background induced by solar neutrinos.

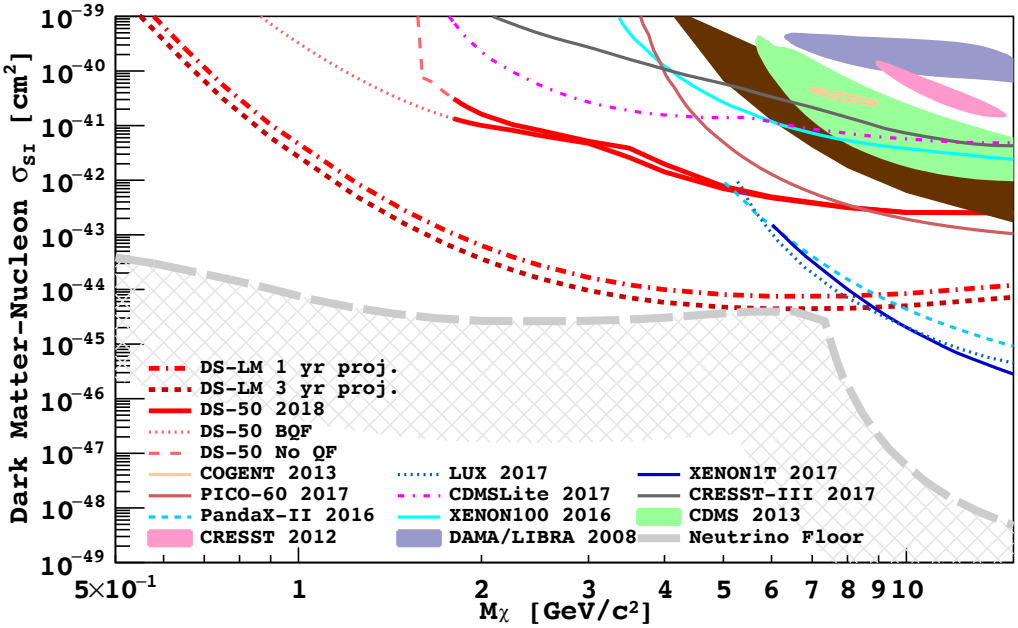

FIG. 34. The 90 % C.L. projected exclusion curves for the DarkSide-LowMass detector in its second configuration, represented as red-dashed lines for two different exposures of 1 yr and 3 yr. For comparison, shown are also the 90 % C.L. exclusion curve from Ref. [52, 61, 91–105], the region of claimed discovery of Ref. [65, 106–108], and the neutrino floor for LAr experiments from Ref. [109].

VI. DARKSIDE TECHNOLOGY FOR NEUTRINO-LESS DOUBLE BETA DECAY SEARCHES: DARKNOON

In this chapter I will describe the possibility of using the DarkSide technology for a search for neutrino-less double beta decay able to provide a yes/no answer to the fundamental question of the quantum representation of neutrinos.

The idea is to develop a cryogenic TPC filled with a solution of liquified argon and xenon ("the soup") [110–116] with the LXe fraction enriched in ^{136}Xe at the level of 90 %. The soup would operate near the argon normal boiling point, 87 K. Operation at this temperature is critical to reduce the dark rate of SiPMs [82, 117] and also allows to contain background from all radon isotopes at levels not possible for pure LXe detectors [44]. The LAr would be liquefied UAr to minimize the overall ^{39}Ar rate.

We note that as of this time, the largest xenon doping concentration in LAr reported is 20 % molar, equivalent to 45 % by weight, reported to allow stable operation near 87 K [110]. The detector considered in this study is an idealized study case, with a LXe mass fraction of 45 %, and a mass fraction of the ^{136}Xe isotope of 41 %.

VI.A. Background Sources and Mitigation Strategy

As for the dark matter search, also for the double beta decay search case the background is a key aspect to be considered. For the choice of radioisotopes to be taken into account and debated, we have established two selection criteria: first, the decay of the radionuclide must release sufficient energy to interfere with the detection of $0\nu\beta\beta$ decay of ^{136}Xe, which has a $Q_{\beta\beta}$ of 2458 keV; second, the radionuclide must have a sufficiently long half-life or must be produced *in situ* in the detector. In addition, we must properly account for other forms of ionizing radiation that present possible interferences.

A list of the possible background sources must include:

Long-lived Radionuclide: This class of background is constituted by the radionuclides of decay chain of ^{238}U and ^{232}Th. For our analysis we have considered only ^{214}Bi from ^{238}U and ^{208}Tl from ^{232}Th chain. The decay process of ^{214}Bi in ^{214}Po includes a γ-ray line at 2448 keV, close to the ^{136}Xe $Q_{\beta\beta}$,

and therefore extremely dangerous. The decay of ^{208}Tl is also responsible for the emission of another potentially dangerous γ-ray, with energy of 2614 keV. The mitigation strategy for the γ-ray from ^{214}Bi must include tagging through ^{214}Bi-^{214}Po coincidences, including space and time correlation, and identification of the β-ray-α-ray sequence. The mitigation strategy must include strong radon abatement, as made possible by operation at 87 K. It must also include minimization of background from the cryostat and any construction material, as the two energetic γ-rays sources by ^{214}Bi and ^{208}Tl can penetrate large distance.

Cosmogenically created radionuclides: Direct dark matter search experiments are located deep underground in order to be shielded against the cosmic rays and their interaction products. At moderate depths, however, the residual muon flux may still produce measurable amounts of radioactive isotopes by muon-induced spallation. In our case we have to take into account activation of both LXe and LAr. The most dangerous xenon radionuclide produced by activation is ^{137}Xe, which decays emitting a β-ray with a 4173 keV $Q_{\beta\beta}$. For ^{137}Xe, we rely upon the estimate of the nEXO Collaboration of a production rate of cosmogenic ^{137}Xe of 2.2×10^{-3}/(kg d) [118] at SNOLAB depth (equivalent to 2.7×10^{-3}/(kg d) given the 80.7 % of enrichment assumed in the calculation). As for the activation in LAr, we rely on the spectra made available in Ref. [119]. The rates and spectra can be easily ported from one laboratory setting to the other by rescaling with the residual muon flux, given the small difference in the residual muon flux [120].

Neutrino induced background: Interactions of solar neutrinos in the detector are a potential source of background for $0\nu\beta\beta$ experiments, since electron-neutrino scattering in the detector could mimic the signature of a candidate event. The neutrino capture process, via the charged-current reaction $\nu + {}^{136}\mathrm{Xe} \rightarrow e^- + {}^{136}\mathrm{Cs}$, which can contribute background events due to the prompt electron signal combined with any γ-ray emitted from the ^{136}Cs de-excitation, and the delayed decay of ^{136}Cs into ^{136}Ba with a 13.2 d half-life and a 2548 keV $Q_{\beta\beta}$. This background is totally negligible and not accounted for in our calculations. A more prominent role is played by solar neutrinos scatter on target electrons: while ^{7}Be neutrinos are well below threshold, ^{8}B neutrinos produce a continuous spectrum covering the full energy range of interest. Since solar neutrinos cannot be stopped, the only possible mitigation strategy requires the development of technologies able to distinguish the single electron resulting from the scatter of ^{8}B neutrinos from the two electrons expected of the ^{136}Xe double beta decay.

VI.B. Specific Detector Configuration

The detector under consideration is designed to permit operations with a target fiducial mass of 50 t of ^{136}Xe. The natural design to be considered is that of a TPC in the shape of DarkSide-20k, i.e. an active volume in form of an octagonal prism contained within an ultra-high purity PMMA vessel.

In order to factorize the problem of external backgrounds, we make the assumption that the TPC is operated inside a DUNE-like cryostat of infinite dimensions, so that the external background due to the construction materials of the cryostat and to any surrounding veto detector is by definition negligible.

In order to simplify the calculation of cosmogenic background, we make the assumption that the detector is installed at SNOLAB, with a depth of 6000 m.w.e. and a residual muon flux of 1.2×10^{-2}/(m^2 h) [120].

The dimensions of the DarkNoon TPC were determined in an iterative process, consisting of initial attempts and simulations. The final outcome is an active volume in form of an octagonal prism with a 670 cm height and a 175 cm side of the octagon. The fiducial volume is defined by a fiducial cut of 30 cm from all surfaces defining the active volume. The thickness of the PMMA vessel is 25 cm in all directions. The components and materials of the detector are summarized in Table VIII.

The specific activities are listed in Table IX. Concerning the specific activities, the following assumptions are made.

I will make the assumption that the target UAr has the same radioactivity as the DarkSide-50 target.

Improvements are possible for the activity of the PDMs, and I will assume a reduction in radioactivity by two orders of magnitude below that expected for DarkSide-LowMass in its second configuration, based on the possibility to develop, within the time frame of two decades considered for the effective start of the program, PDMs with silicon interposer with integrated electronics in lieu of printed circuit boards carrying soldered components.

Improvements are also possible for the PMMA. I will consider that possibility that, following a two-decades improvement program, the specific activity can be lowered at a level one order of magnitude below the best values obtained for JUNO [83].

VI.C. Background Simulation and Analysis

The analysis procedure follows that introduced for the low-mass dark matter search. The first step consists in the event reconstruction. For each event, starting with the decay nucleus, the output of the G4DS simulation is categorized by energy clusters in the active volume of the TPC. A cluster is defined as one or more energy deposits which occur at a distance not greater than 2 mm on the z-axis and within a 2 µs time window, opening with the first energy deposition. The clustering is applied in order to minimize the impact of artificial discretization performed by Geant4, which treats continuous energy losses as successive finite steps and to reproduce the finite resolution of the detector. In order to simplify the simulation, I opted not to perform a detailed tracing of the photons: this important step is left for follow-up studies.

After event reconstruction, the two following cuts are applied:

Single scatter cut: we expect $0\nu\beta\beta$ (and $2\nu\beta\beta$) decays to produce interactions contained within a 2 cm radius in the active volume of the detector. All events with a different topology are therefore rejected, as likely originated by interactions induced by γ-rays.

Fiducial Cut: one of the main sources of background is due to radio-impurities in the PMMA and in the PDMs. With this cut we eliminate any event reconstructed in the outer 30 cm of the active volume.

Consistency Cut: With this method we also reject a class of small number of events that have large S1 pulse, even when accompanied by an abnormally low S2 pulse that would, on its own, fall in the region of interest. These events tend to occur near the wall of the LAr TPC, and therefore their largest majority of them is independently rejected by the fiducial cut.

The next step in the analysis is the normalization of the spectra of each simulated isotope by the expected activity reported in Table IX. We have assumed the possibility of achieving a an energy resolution of 0.7 % ($1\,\sigma$) at the ^{136}Xe $Q_{\beta\beta}$, based on a reasonable extrapolation from the 1.5 % ($1\,\sigma$) resolution achieved in DarkSide-50, slightly better than the 1.6 % ($1\,\sigma$) achieved in EXO-200. [121]

I have considered three different cases, corresponding to no fiducial cut, to the standard 30 cm fiducial cut, and to a fiducial cut of 50 cm. The results are shown in Fig. 35, 37, and 37.

As we can see from all the three studied cases the major contribution to the background comes from mostly from the activity of ^{238}U and ^{232}Th in PDMs.

VI.D. Signal Analysis

The experimental signature of $0\nu\beta\beta$ is a mono-energetic peak at the Q-value of the chosen isotope decay, produced by the absorption in the detector of the two emitted electrons. To calculate the experimental sensitivity and discovery probability of DarkNoon we follow the procedure reported in Ref. [122].

The sensitivity of a neutrino-less double beta decay experiment is driven by Poisson statistics for events near $Q_{\beta\beta}$, so we can consider it as a counting experiment for which two main parameters determine the sensitivity: the isotope exposure, $\mathcal{E}$, and the specific background in the region of interest (ROI), $\mathcal{B}$. $\mathcal{E}$ is given by the product of fiducial mass of the isotope of interest and of the live time (corrected, where needed, by the efficiency of cuts). $\mathcal{B}$ is the (flat) background in the ROI, in units of counts per unit of mass, energy, and time.

We now define the number of signal and background counts as:

TABLE VIII. Components and materials of the DarkNoon detector.

Components	Material	Mass	Units
Vessel	PMMA	36703.8	[kg]
PDMs	Various	8280	
Target	^{136}Xe	74600	[kg]
Target	other Xe	82888.9	[kg]
Target	UAr	20000	[kg]

TABLE IX. Specific activities for the materials of the DarkNoon detector.

Material	Cf.	^{238}U	^{226}Ra	^{235}U	^{232}Th	^{40}K	^{60}Co	^{39}Ar	Units
PMMA	✓	0.4	0.4	0	0.5	<250	0	0	[µBq/kg]
PDMs	✓	6	2	0.2	1	<4	<0.2	0	[µBq/PDM]
UAr	✓	0	0	0	0	0	0	730	[µBq/kg]

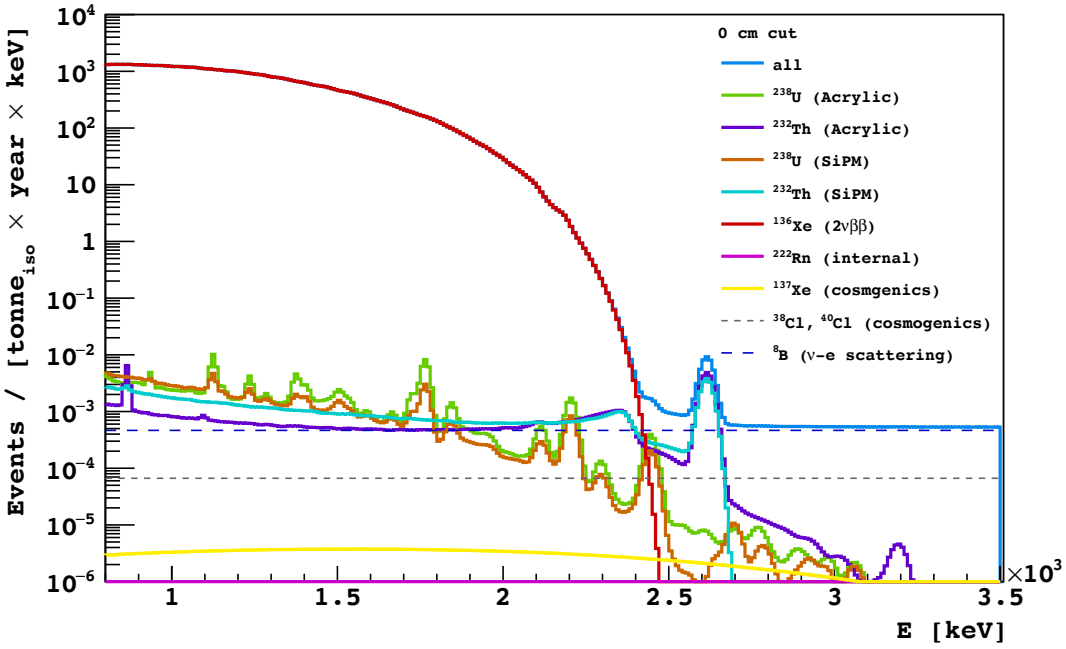

FIG. 35. DarkNoon background without fiducial cut.

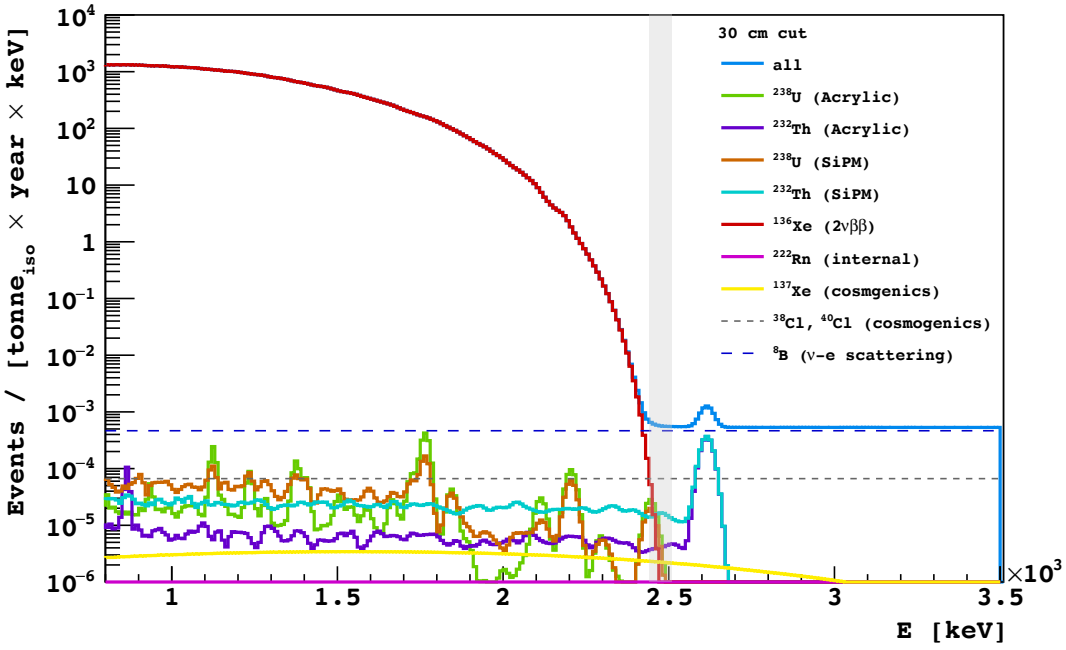

FIG. 36. DarkNoon background with a 30 cm fiducial cut.

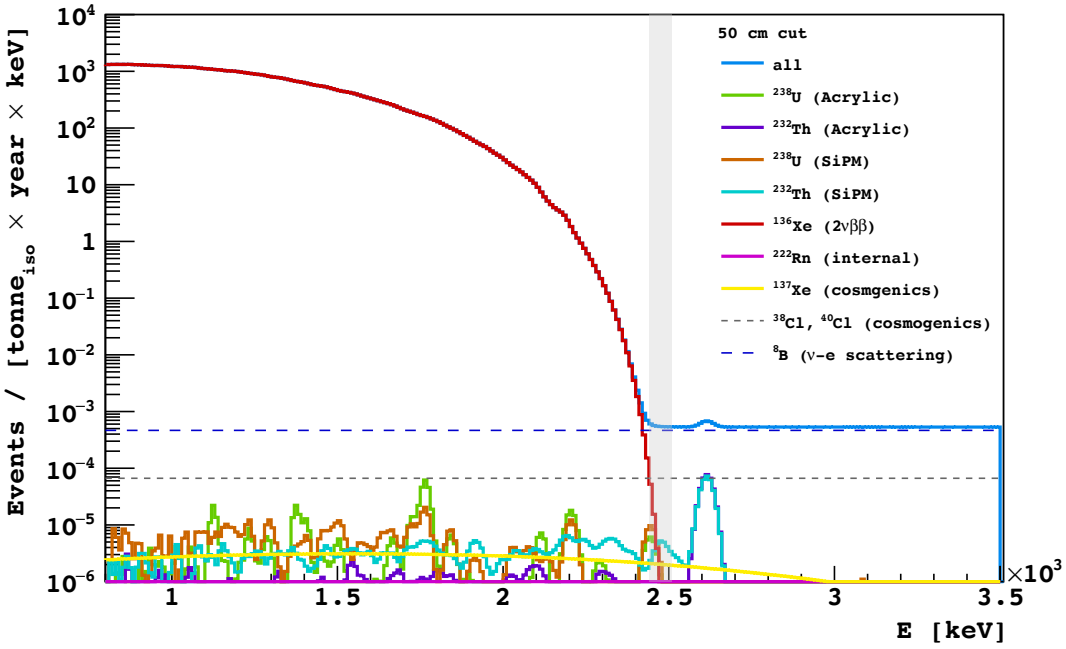

FIG. 37. DarkNoon background with a 50 cm fiducial cut.

$$N_{0\nu\beta\beta} = \frac{ln2 \cdot N_A \cdot \mathcal{E}}{m \cdot T_{1/2}}, \tag{47}$$

$$N_{\text{bkg}} = \mathcal{B} \cdot \mathcal{E}, \tag{48}$$

where N_A is Avogadro's number, m is the molar mass of target isotope and $T_{1/2}$ is the half-life of the decay. The sensitivity of an experiment to discover a signal has been defined in this work as the value of $T_{1/2}$ or $m_{\beta\beta}$ for which the experiment has a 50 % chance to measure a signal with a significance of at least $3\,\sigma$. The computation is performed for $T_{1/2}$ and the result converted to a range of $m_{\beta\beta}$ values. Given an expectation for the background counts in the ROI of $N_{\text{bkg}} = \mathcal{B} \cdot \mathcal{E}$ the sensitivity for $T_{1/2}$ is given by:

$$T_{1/2} = ln2 \frac{N_A \mathcal{E}}{m_a S_{3\sigma}(B)}, \tag{49}$$

where $S_{3\sigma}(N_{\text{bkg}})$ denotes the Poisson signal expectation at which 50 % of the measurements in an ensemble of identical experiments would report a 3σ positive fluctuation above N_{bkg}. The number of counts $C_{3\sigma}$ such that the cumulative Poisson distribution with mean N_{bkg} satisfies $\text{CDF}_{\text{Poisson}}(C_{3\sigma}|N_{\text{bkg}}) = \sigma$ and then obtain $S_{3\sigma}$ is given by solving $\overline{\text{CDF}}_{\text{Poisson}}(C_{3\sigma}|S_{3\sigma} + N_{\text{bkg}}) = 50\,\%$. To extend $\text{CDF}_{\text{Poisson}}$ to a continuous distribution in C, we'll define it using the normalized upper incomplete gamma function, and solve:

$$\text{CDF}_{\text{Poisson}}(C|\mu) = \frac{\Gamma(C+1,\mu)}{\Gamma(C+1)}. \tag{50}$$

VI.E. Physics Potential

Using Eq. (50), $S_{3\sigma}$ varies smoothly and monotonically with B for values greater than $-\ln[\text{erf}\,(3/\sqrt{2})] = 0.0027$ counts. Below this value of B, the observation of a single count represents a $3\,\sigma$ discovery; this could be considered as the level at which an experiment becomes effectively background-free under this metric. In

this regime, $S_{3\sigma}$ takes the constant value $\ln 2$. In a similar manner we can define the discovery probability as the probability that an experiment will measure a $3\,\sigma$ positive fluctuation above B, given the probability distribution function $dP/dm_{\beta\beta}$ for $m_{\beta\beta}$. The discovery probability (P) is then given by:

$$P = \int_0^\infty \frac{dP}{dm_{\beta\beta}} \overline{\mathrm{CDF}}_{\mathrm{Poisson}}(C_{3\sigma}|S(m_{\beta\beta}) + B) dm_{\beta\beta} \tag{51}$$

where $S(m_{\beta\beta})$ is the expected signal counts in the experiment for a given value of $m_{\beta\beta}$.

To compare the obtained result with other experiments searching for $0\nu\beta\beta$ I have followed the procedure adopted by JUNO Collaboration in Ref. [123]. In an experiment with non-negligible background, the sensitivity of $0\nu\beta\beta$ half-life can be written as:

$$T_{1/2}^{0\nu\beta\beta} = \ln 2 \cdot \frac{N_A}{m_{\mathrm{iso}}} \cdot \frac{M \cdot \epsilon\eta \cdot t}{\alpha \cdot \sqrt{b}}, \tag{52}$$

where $N_A = 6.022{\times}10^{23}$ is the Avogadro's number, m_{iso} is the molar mass of the isotope used for $0\nu\beta\beta$ search, M is the fiducial target mass, t is the live time, ϵ is the detection efficiency and η is the abundance of the $0\nu\beta\beta$ isotope. Moreover, to calculate the sensitivity at the 90 % (95 %) C.L., α is 1.64 (1.96). At this point the Eq. (52):

$$\left(\frac{T_{1/2}^{0\nu\beta\beta} \cdot \alpha}{ln2 \cdot N_A}\right) = \frac{M_{norm}}{B_I}, \tag{53}$$

where:

$$B_I = \frac{b}{(M\epsilon\eta \cdot t/m_{iso}) \cdot \mathrm{ROI}}, \tag{54}$$

is the redefined background index and

$$M_{norm} = \frac{M\epsilon\eta \cdot t}{ROI \cdot M_{isotope}} \tag{55}$$

is the normalized detector exposure. From the computation of these variables, given the background events in the ROI as per Fig. 36, assuming a run time of 20 yr and an exposure of 1000 t yr, the discovery potential of DarkNoon is as stated in Fig. 38. The values used for DarkNoon comes from the background simulation of $0\nu\beta\beta$ with the fiducial cut at 30 cm in a ROI of 34.4 keV, for which I obtained a fiducial exposure of 346 t yr of ^{136}Xe, a projected background for the whole exposure of 6.4 events and a detection efficiency of 68 %. For completeness the point corresponding to DARWIN experiment comes from [124], from which it was considered an exposure of ^{136}Xe of 534 kg yr, a projected background of 138 events, a detection efficiency of 90 % in the region between 2385 keV and 2533 keV.

From this result we can see that with the hypothetical background budget of DarkNoon we can reach a sensitivity of for $T_{1/2}^{0\nu\beta\beta}$ in excess of 10^{29} yr. For comparison with the nEXO previsions it will reach a much lower sensitivity at 9.2×10^{27} yr following a 18 t yr exposure in a 10 yr run [118]. The proposed JUNO extensions with the addition of a central vessel loaded with ^{136}Xe also reach a lower sensitivity [83].

VI.F. Probing Cherenkov effect as background strategy

The result reported in Fig. 37 shows that, apart the limiting background given by the ^{8}B neutrinos electron scattering, another important source of background is due to the single electron of double beta decay of ^{136}Xe in the ROI since electrons have short (few mm) range in LAr and LXe a single recoil electron background results in a single detectable interaction site just as the neutrinoless double beta decay does. For this reason, a site multiplicity cut cannot distinguish between this background and the signal. This source of background could be further reduced, and the sensitivity improved, by leveraging the differences

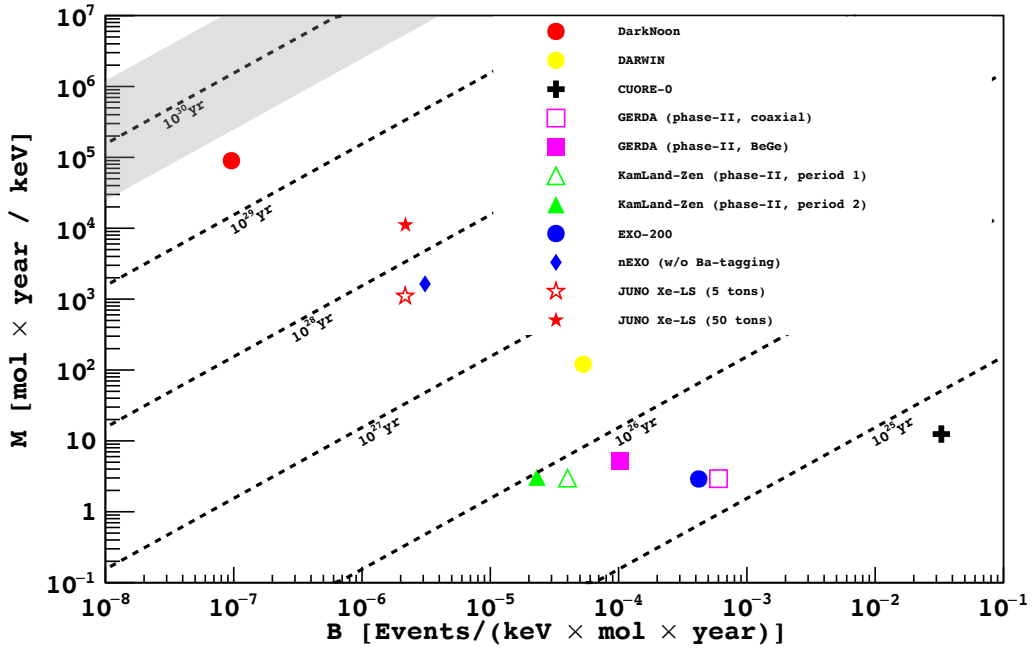

FIG. 38. Exposure, background index, and discovery potential for DarkNoon compared with other experiments already completed or planned. The dashed lines are the contours of different sensitivities.

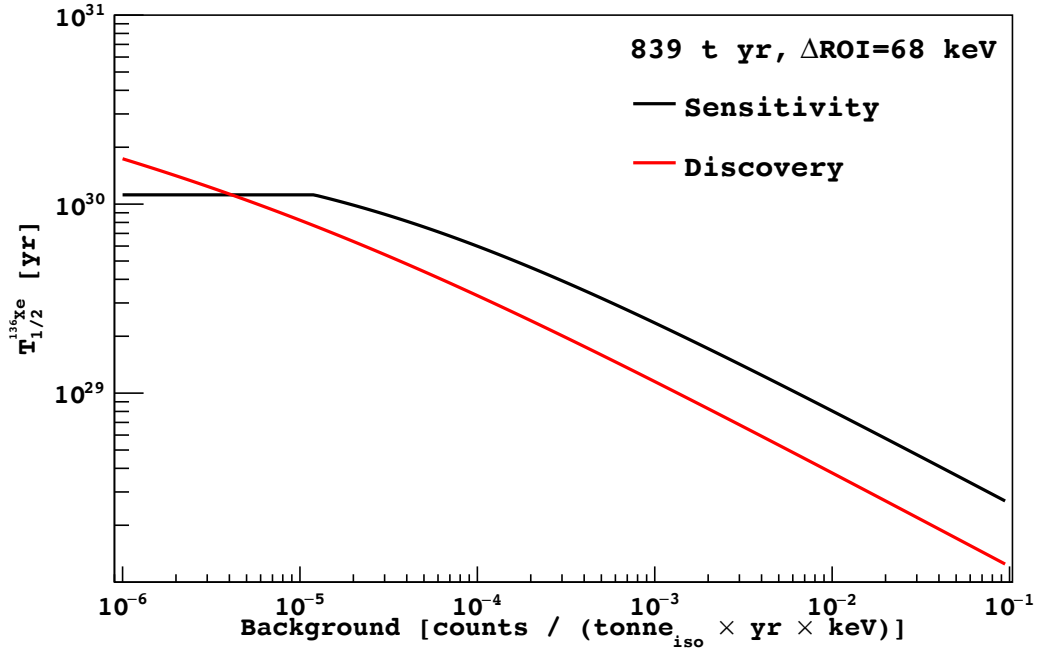

FIG. 39. Sensitivity and discovery power for DarkNoon as a function of exposure.

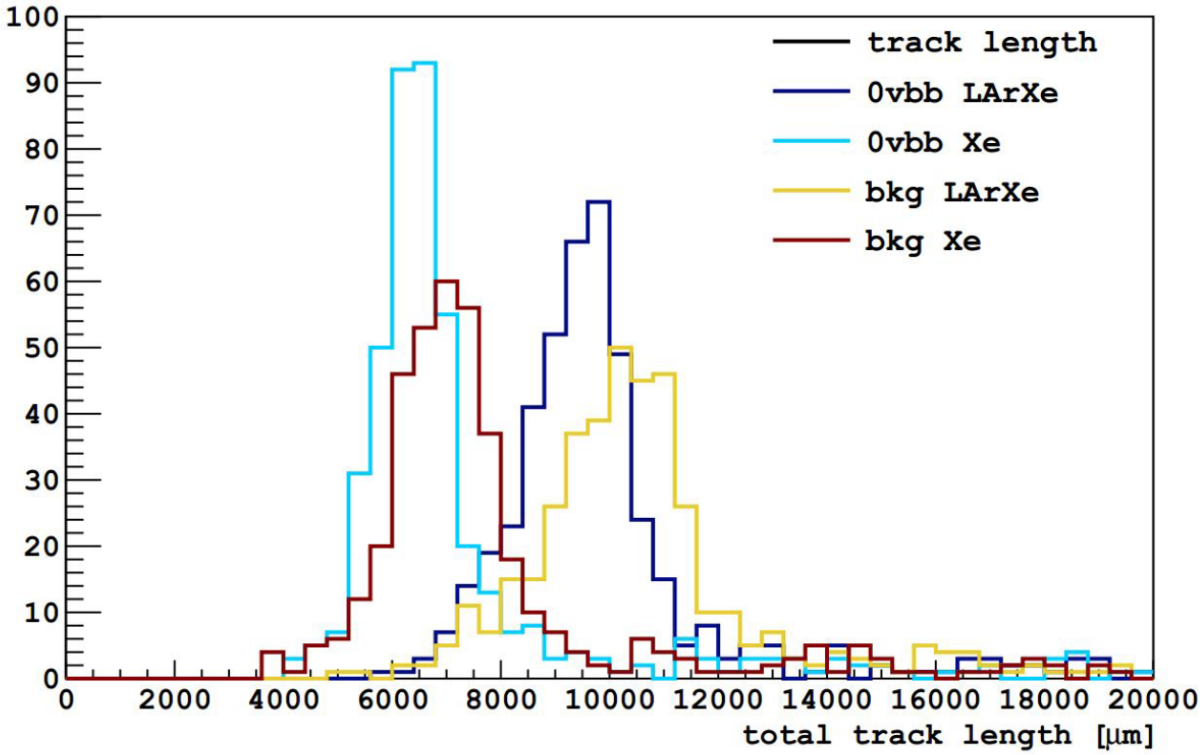

FIG. 40. Track length of single beta and double beta events with energy equal to $Q_{\beta\beta}$

in the Cherenkov photons produced between background and $0\nu\beta\beta$ events. The number and directional distribution of Cherenkov photons depends on the type of event, allowing for background discrimination and sensitivity improvement. In order to test the sensitivity achievable from the detection of Cherenkov γ-rays we can use a toy MonteCarlo simulation, using the geometry illustrated in Sec. VI.B. The simulation will consist of mainly 2 steps: in the first one single beta events of energy of 2.5 MeV and $0\nu\beta\beta$ of ^{136}Xe are produced both in the mixture of LAr-LXe, in the ratio 80 % and 20 % molar mass, and in pure Xe. Once completed this first step it is useful to record the tracks of beta events. The result of the procedure is represented in Fig. 40.

The figure shows that the track length of single and double beta particles in pure LXe is shorter than in the mixture of LAr-LXe.

The second step of simulation consists in producing Cherenkov photons according the Eq. (56), starting from the previous generated electrons.

$$\frac{d^2E}{dxd\omega} = \frac{q^2}{4\pi}\mu(\omega)\omega\left(1 - \frac{c^2}{v^2n^2(\omega)}\right) \tag{56}$$

From Eq. (56), where ω is the frequency of the radiation, $\mu(\omega)$ and $n(\omega)$ are the permeability and the index refraction of the material the charge particle moves through respectively and v is the speed of the particle, is clear that the number and spectrum of Cherenkov photons produced in LXe and LAr depends on their indices of refraction, which are wavelength-dependent. A functional form of the indices of refraction of LAr and LXe as function of wavelength is described in [125]. The dependence of index of refraction on wavelength in LAr and LXe is reported in Fig. 41 and Fig. 42 respectively.

In this first approach in the simulation we assume that the refractive index of the mixture is a constant from 200 nm to 800 nm; the resulting Cherenkov yield from electrons is reported in Fig. 43. The cut on the wavelength is due to the fact that we want to exclude from analysis the photons coming from the ionization of Xe atoms, that is at 147 nm, [125].

Comparing Fig. 40 and Fig. 43 results is clear that the LAr-LXe mixture gives better discrimination in terms of produced photon yield.

These results are very preliminary, a feasibility study of the use of Cherenkov light as background discriminator is carried on in Princeton, where an experimental setup is installed to measure the stability of the LAr-LXe mixture and the Cherenkov light recorded at different Xe concentration. A first plot of background

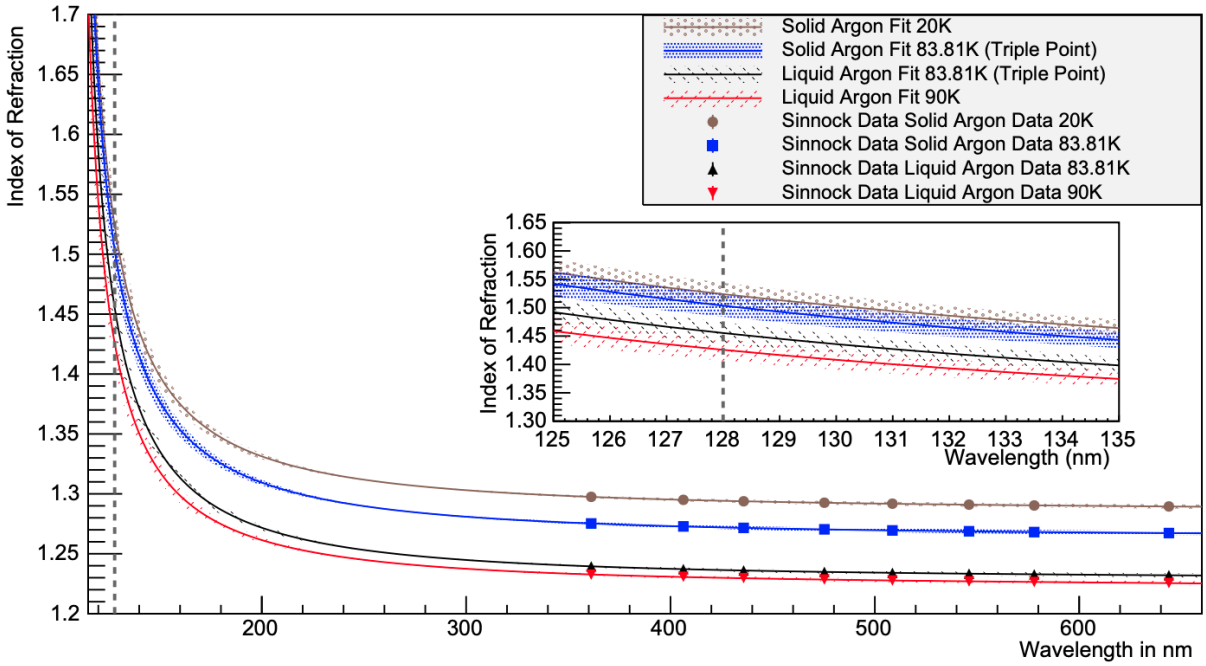

FIG. 41. Calculated index of refraction as function of wavelength (nm) for solid and liquid argon. Credit Ref. [125]

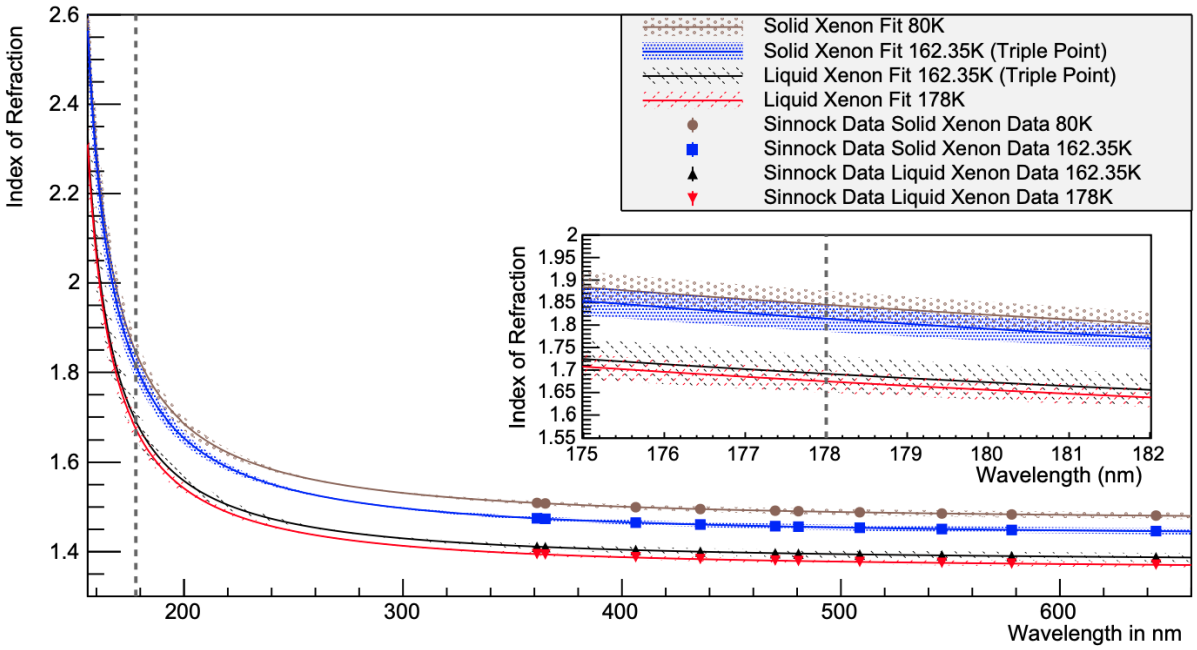

FIG. 42. Calculated index of refraction as function of wavelength (nm) for solid and liquid xenon. Credit Ref. [125]

rejection efficiency with Cherenkov effect at different concentration of Xe in LAr-LXe mixture is reported in Fig. 44

The last plot shows that with a 5 % concentration of Xe in the LAr-LXe mixture performs the best background rejection and signal efficiency. At this point one could cross the efficiency of the Cherenkov cut and the sensitivity achieved using the Eq. (52); the result is shown in Fig. 45

With the new sensitivity reached, molar mass of Xe of 1000 t and a reduced background after the Cherenkov cut, we can plot the new values for the background index and normalized detector exposure, Fig. 46

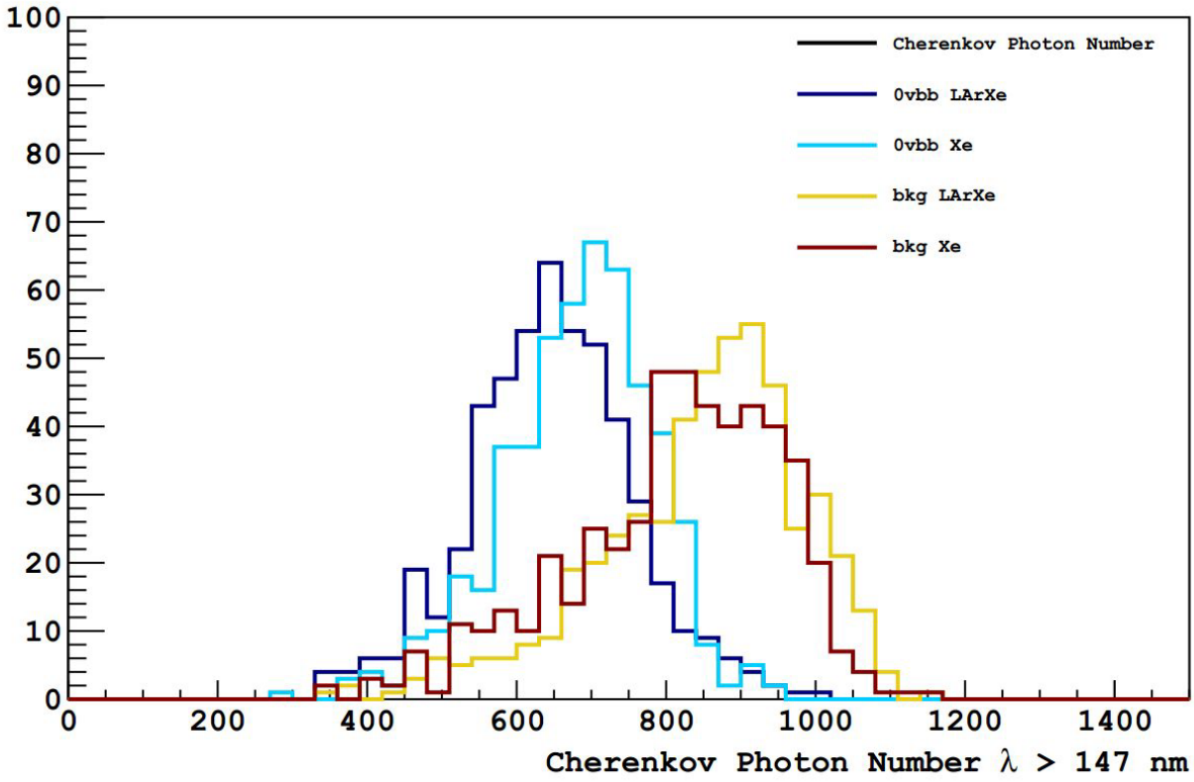

FIG. 43. Cherenkov photon yield for beta particles with energy equal to $Q_{\beta\beta}$

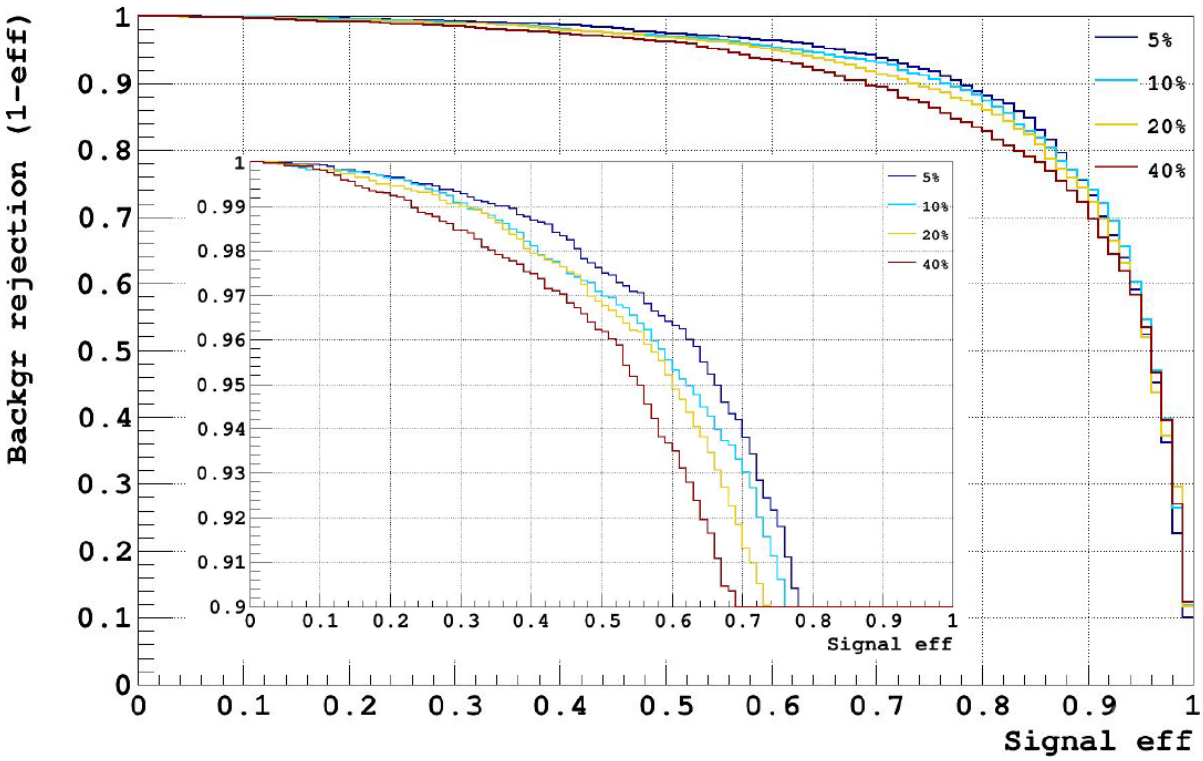

FIG. 44. The performance of several Xe concentration is evaluated. From the plot one can see the 5 % of Xe concentration performed the best signal efficiency and background rejection simultaneously.

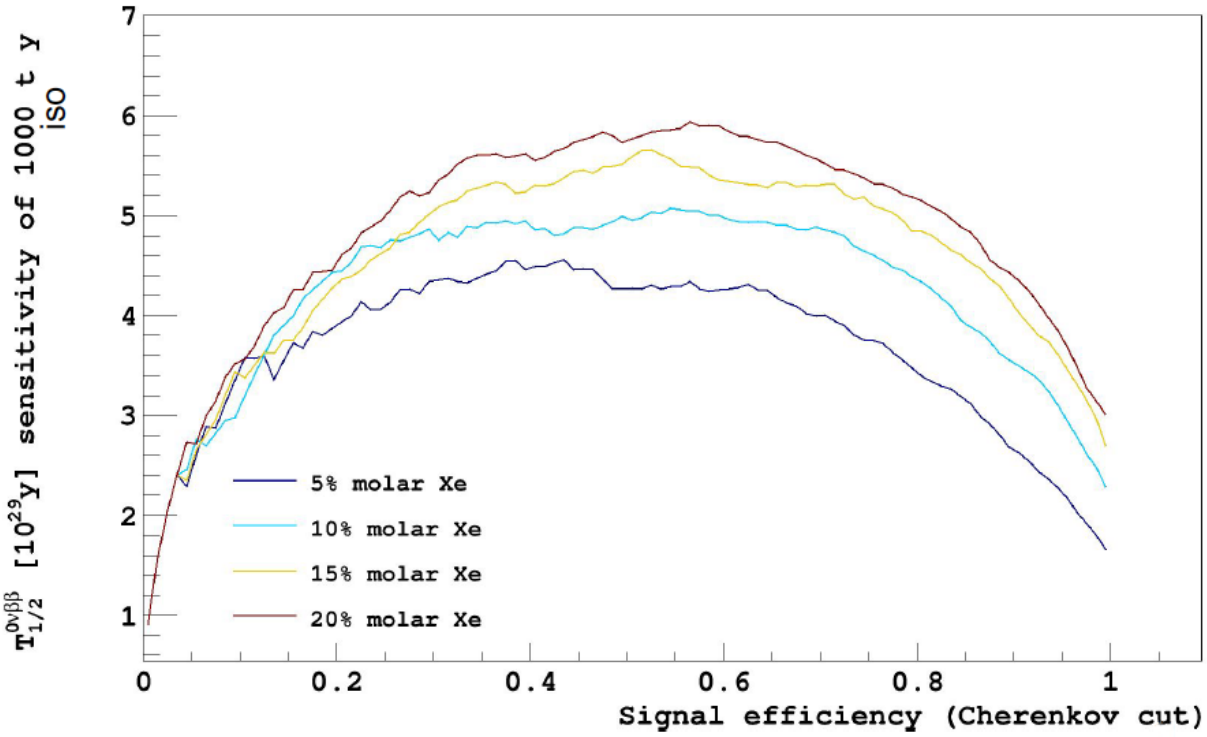

FIG. 45. Sensitivity reached for $0\nu\beta\beta$ as function of efficiency of Cherenkov cut. The plot shows the sensitivity achievable as function of the efficiency of Cherenkov cut for different concentration of Xe. The maximum sensitivity is with 20 % molar mass of Xe.

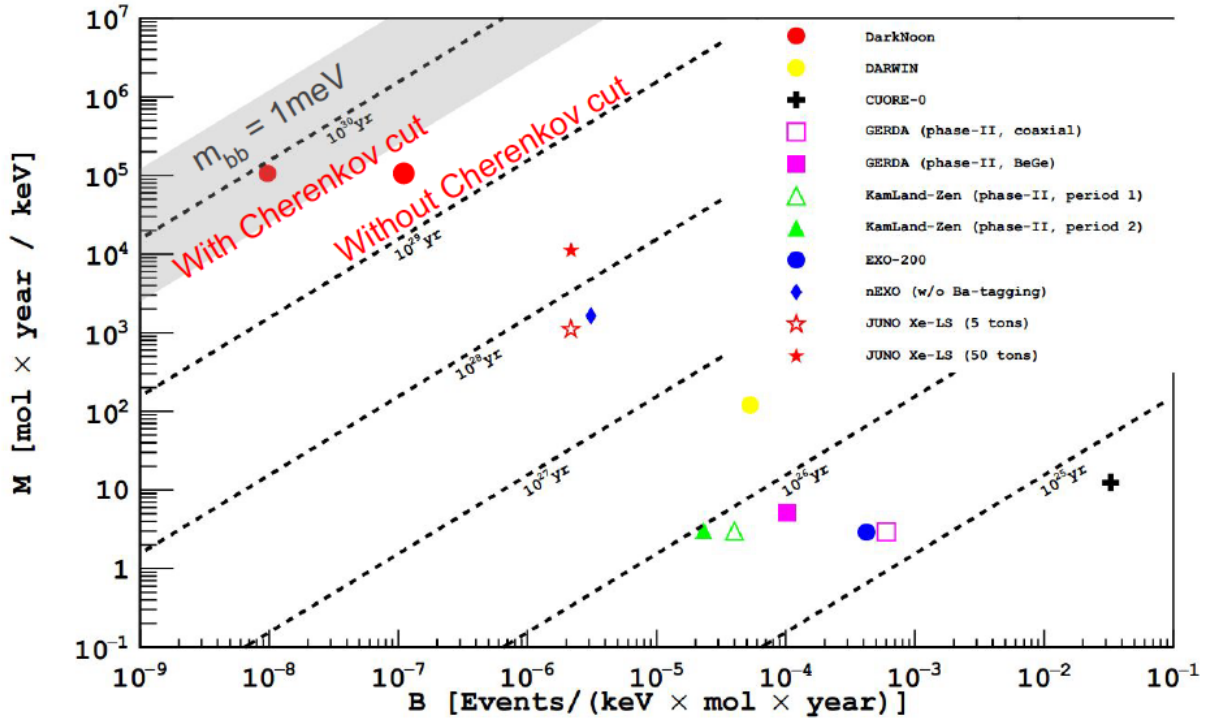

FIG. 46. Exposure, background index, and discovery potential for DarkNoon with Chrenkov cut compared with other experiments. The dashed lines are the contours of different sensitivities.

VII. CONCLUSIONS

The DarkSide program has set a high standard among dark matter detectors setting several best records for control of background sources. Today it holds the best sensitivity for low-mass dark matter. The main characteristic of the program is the use of ultra-low radioactivity argon highly suppressed in the ^{39}Ar contaminating the argon in the atmosphere. Another defining characteristic of the DarkSide program is the ongoing development of ultra-low background photodetector modules, based on large-area assemblies of silicon photomultipliers, especially designed to operate at the normal boiling point of liquid argon.

The main goal of the DarkSide program is the construction of two leading experiments for the discovery of high-mass dark matter. The sequence of DarkSide-20k, with its target of a few tens of tonnes, and Argo, with a target of a few hundred tonnes, is expected to lead the searches for high-mass dark matter since the start of the data taking with DarkSide-20k.

I have explored the feasibility of utilizing the DarkSide technology to attack two equally important and crucial open problems in astroparticle physics.

My findings indicate that the DarkSide technology can be tweaked to develop a world-leading low-mass dark matter search, DarkSide-LowMass, able to completely sweep the region for a possible discovery for masses below $10\,\mathrm{GeV}/c^2$. This line of research would build upon the search for ultra-low energy events, characterized by the near absence of the S1 signal and the presence of a still robust S2 signal, initiated with DarkSide-50.

I also found that the DarkSide technology can be adapted for operation of a LXe-LAr solution ("the soup") near the LAr normal temperature. A large scale experiment with this technology would be able to achieve an exceptional suppression of background from radon while operating the silicon photomultipliers in a regime where their dark noise is minimized. An experiment with this technology operating with a 50 t fiducial mass of ^{136}Xe for a run of 20 yr would produce the best sensitivity and discovery power of any experiment on the books, and would come tantalizingly close to definitive experiment able to demonstrate or rule out the presence of Majorana neutrinos.

[1] F. Zwicky, Ap. J. **86**, 217 (1937).
[2] F. Zwicky, Helv. Phys. Acta **6**, 110 (1933).
[3] V. C. Rubin and W. K. J. Ford, Ap. J. **159**, 379 (1970).
[4] V. C. Rubin, N. Thonnard, and W. K. J. Ford, Ap. J. **225**, L107 (1978).
[5] D. Clowe, A. Gonzalez, and M. Markevitch, Ap. J. **604**, 596 (2004).
[6] D. Clowe et al., Ap. J. **648**, L109 (2006).
[7] M. Markevitch et al., Ap. J. **606**, 819 (2004).
[8] K. Griest, Ap. J. **366**, 412 (1991).
[9] B. Paczynski, Ap. J. **304**, 1 (1986).
[10] M. Bradač et al., Ap. J. **687**, 959 (2008).
[11] A. A. Penzias and R. W. Wilson, Ap. J. **142**, 419 (1965).
[12] D. J. Fixsen, Ap. J. **707**, 916 (2009).
[13] P. A. R. Ade et al. (The Planck Collaboration), Astro. & Ap. **594**, A13 (2016).
[14] K. Garrett and G. Duda, Advances in Astronomy **2011**, 968283 (2011).
[15] J. D. Lewin and P. F. Smith, Astropart. Phys. **6**, 87 (1996).
[16] A. Giuliani, Physica B: Condensed Matter **280**, 501 (2000).
[17] J. Angle et al. (The XENON Collaboration), Phys. Rev. Lett. **100**, 1459 (2008).
[18] P. Benetti et al. (The WArP Collaboration), Astropart. Phys. **28**, 495 (2008).
[19] J. Chadwick, Verhandl. Deut. Physik. Ges. **16**, 383 (1914).
[20] W. Pauli, Phys. Today **31N9**, 1 (1930).
[21] E. Fermi, Nuovo Cim. **11**, 1 (1934).
[22] J. Chadwick, Nature **129**, 312 (1932).
[23] J. Chadwick, Proc. Royal Soc. London A: Math. Phys. Eng. Sci. **136**, 692 (1932).
[24] F. Reines and C. L. Cowan, Phys. Rev. **92**, 830 (1953).
[25] M. Goldhaber, L. Grodzins, and A. W. Sunyar, Phys. Rev. **106**, 826 (1957).
[26] R. Davis, Phys. Rev. Lett. **12**, 303 (1964).
[27] J. N. Bahcall, W. A. Fowler, I. J. Iben, and R. L. Sears, Ap. J. **137**, 344 (1963).
[28] B. Pontecorvo, JETP **33**, 549 (1958).
[29] Q. R. Ahmad et al. (The SNO Collaboration), Phys. Rev. Lett. **87**, 505 (2001).
[30] K. Eguchi et al. (The KamLAND Collaboration), Phys. Rev. Lett. **90**, 171 (2003).
[31] Y. Fukuda et al. (The Super-Kamiokande Collaboration), Phys. Rev. Lett. **81**, 1562 (1998).
[32] M. H. Ahn et al., Phys. Rev. D **74**, 260 (2006).
[33] R. N. Mohapatra and G. Senjanović, Phys. Rev. Lett. **44**, 912 (1980).
[34] M. Goeppert-Mayer, Phys. Rev. **48**, 512 (1935).
[35] E. Majorana, Nuovo Cim. **14**, 171 (1937).
[36] G. Racah, Nuovo Cim. **14**, 322 (1937).
[37] W. H. Furry, Phys. Rev. **56**, 1184 (1939).
[38] F. T. Avignone, S. R. Elliott, and J. Engel, Rev. Mod. Phys. **80**, 481 (2008).
[39] L. Winslow and R. Simpson, JINST **7**, P07010 (2012).
[40] Y. Sakai, H. Böttcher, and W. F. Schmidt, Journal of Electrostatics **12**, 89 (1982).
[41] S. Kubota, M. Hishida, M. Suzuki, and J.-z. Ruan Gen, Nucl. Inst. Meth. **196**, 101 (1982).
[42] A. Hitachi et al., Phys. Rev. B **27**, 5279 (1983).
[43] M. G. Boulay and A. Hime, Astropart. Phys. **25**, 179 (2006).
[44] P. A. Amaudruz et al. (The DEAP-3600 Collaboration), Phys. Rev. Lett. **121**, 071801 (2018).
[45] S. Himi, T. Takahashi, J.-z. Ruan Gen, and S. Kubota, Nucl. Inst. Meth. **203**, 153 (1982).
[46] A. Hitachi, T. Doke, and A. Mozumder, Phys. Rev. B **46**, 11463 (1992).
[47] A. Hitachi, J. A. LaVerne, and T. Doke, Phys. Rev. B **46**, 540 (1992).
[48] P. Benetti et al. (The ICARUS Collaboration), Nucl. Inst. Meth. A **327**, 173 (1993).
[49] D. B. Cline, Nucl. Inst. Meth. A **327**, 178 (1993).
[50] J. Angle et al., Phys. Rev. Lett. **107**, 650 (2011).
[51] E. Aprile et al. (The XENON Collaboration), Phys. Rev. D **94**, 122001 (2016).
[52] D. S. Akerib et al. (The LUX Collaboration), Phys. Rev. Lett. **118**, 021303 (2017).
[53] E. Aprile et al. (The XENON Collaboration), Phys. Rev. Lett. **121**, 111302 (2018).
[54] P. Agnes et al. (The DarkSide Collaboration), Phys. Lett. B **743**, 456 (2015).
[55] P. Agnes et al. (The DarkSide Collaboration), Phys. Rev. D **93**, 081101 (2016).
[56] P. Agnes et al. (The DarkSide Collaboration), Phys. Rev. D **98**, 102006 (2018).
[57] D. Acosta-Kane et al., Nucl. Inst. Meth. A **587**, 46 (2008).
[58] J. Xu et al., Astropart. Phys. **66**, 53 (2015).
[59] H. O. Back et al., arXiv:1204.6024v2 (2012).
[60] X. Cui et al. (The PandaX-II Collaboration), Phys. Rev. Lett. **119**, 181302 (2017).
[61] P. Agnes et al. (The DarkSide Collaboration), Phys. Rev. Lett. **121**, 081307 (2018).
[62] C. E. Aalseth et al. (The DarkSide Collaboration), Eur. Phys. J. Plus **133**, 131 (2018).
[63] B. Abi et al. (The DUNE Collaboration), arXiv:1706.07081v2 (2017).
[64] R. Acciarri et al. (The DUNE Collaboration), arXiv:1601.05471v1 (2016).
[65] G. Angloher et al. (The CRESST Collaboration), Eur. Phys. J. C **72**, 1971 (2012).

[66] T. A. Collaboration, CERN Doc. Serv. (2018).
[67] H. Nelson (For The LZ Collaboration), Presentation at DM 2014 (2014).
[68] V. A. Kudryavtsev (The LZ Collaboration), AIP Conf. Proc. **1672**, 060003 (2015).
[69] E. Aprile (For The XENON Collaboration), Presentation at LNGS Sci. Comm. Apr. 2015 (2015).
[70] M. G. Boulay (For the DarkSide Collaboration), Presentation at New Ideas DM 2017 (2017).
[71] R. Agnese et al. (The SuperCDMS Collaboration), Phys. Rev. D **95**, 215 (2017).
[72] J. Billard, E. Figueroa-Feliciano, and L. Strigari, Phys. Rev. D **89**, 023524 (2014).
[73] D. Abercrombie et al., arXiv:1507.00966v1 (2015).
[74] R. B. Firestone, C. M. Baglin, and S. Y. F. Chu, *Table of isotopes*, Wiley-Interscience (1999).
[75] P. Agnes et al. (The DarkSide Collaboration), JINST **12**, P10015 (2017).
[76] S. Kubota et al., Phys. Rev. B **13**, 1649 (1976).
[77] T. Doke et al., Jpn. J. Appl. Phys. **41**, 1538 (2002).
[78] J. Thomas and D. A. Imel, Phys. Rev. A **36**, 614 (1987).
[79] P. Agnes et al. (The DarkSide Collaboration), Phys. Rev. Lett. **121**, 111303 (2018).
[80] P. Sorensen, arXiv:1702.04805v1 (2017).
[81] P. Agnes et al. (The DarkSide collaboration), JINST **11**, P03016 (2016).
[82] M. D'Incecco et al., IEEE Trans. Nucl. Sci. **65**, 591 (2018).
[83] F. An et al., J. Phys. G **43**, 030401 (2016).
[84] T. Alexander et al. (The SCENE Collaboration), Phys. Rev. D **88**, 092006 (2013).
[85] H. Cao et al. (The SCENE Collaboration), Phys. Rev. D **91**, 092007 (2015).
[86] T. H. Joshi et al., Phys. Rev. Lett. **112**, 171303 (2014).
[87] P. Agnes et al. (The ARIS Collaboration), Phys. Rev. D **97**, 10 (2018).
[88] F. Bezrukov, F. Kahlhoefer, and M. Lindner, Astropart. Phys. **35**, 119 (2011).
[89] G. Cowan, K. Cranmer, E. Gross, and O. Vitells, Eur. Phys. J. C **71**, 1 (2011).
[90] W. Verkerke and D. Kirkby, Proc. PHYSTAT05 **1**, 186 (2006).
[91] E. Aprile et al. (The XENON Collaboration), Phys. Rev. D **94**, 092001 (2016).
[92] R. Agnese et al. (The SuperCDMS Collaboration), Phys. Rev. Lett. **112**, 041302 (2014).
[93] R. Agnese et al. (The SuperCDMS Collaboration), Phys. Rev. Lett. **112**, 241302 (2014).
[94] G. Angloher et al. (The CRESST Collaboration), Eur. Phys. J. C **76**, 25 (2016).
[95] W. Zhao et al. (The CDEX Collaboration), Phys. Rev. D **93**, 092003 (2016).
[96] A. Aguilar-Arevalo et al. (The DAMIC Collaboration), Phys. Rev. D **94**, 082006 (2016).
[97] A. Tan et al. (The PandaX-II Collaboration), Phys. Rev. Lett. **117**, 121303 (2016).
[98] L. Hehn et al. (The EDELWEISS Collaboration), Eur. Phys. J. C **76**, 548 (2016).
[99] C. Amole et al. (The PICO Collaboration), Phys. Rev. Lett. **118**, 251301 (2017).
[100] E. Aprile et al. (The XENON Collaboration), Phys. Rev. Lett. **119**, 181301 (2017).
[101] H. Jiang et al. (The CDEX Collaboration), Phys. Rev. Lett. **120**, 241301 (2018).
[102] Q. Arnaud et al. (The NEWS-G Collaboration), Astropart. Phys. **97**, 54 (2018).
[103] E. Behnke et al. (The PICASSO Collaboration), Astropart. Phys. **90**, 85 (2017).
[104] R. Agnese et al. (The SuperCDMS Collaboration), Phys. Rev. D **97**, 215 (2018).
[105] F. Petricca et al. (The CRESST Collaboration), arXiv:1711.07692v1 (2017).
[106] R. Agnese et al. (The CDMS Collaboration), Phys. Rev. Lett. **111**, 251301 (2013).
[107] C. E. Aalseth et al. (The CoGeNT Collaboration), Phys. Rev. D **88**, 012002 (2013).
[108] C. Savage, G. Gelmini, P. Gondolo, and K. Freese, JCAP **2009**, 010 (2009).
[109] F. Ruppin, J. Billard, E. Figueroa-Feliciano, and L. Strigari, Phys. Rev. D **90**, 083510 (2014).
[110] A. F. Borghesani et al., Physics Letters A **178**, 407 (1993).
[111] M. Suzuki, M. Hishida, J. Ruan Gen, and S. Kubota, Nucl. Inst. Meth. A **327**, 67 (1993).
[112] S. Kubota et al., Nucl. Inst. Meth. A **327**, 71 (1993).
[113] E. Conti, G. Carugno, and A. Intravaia, Nucl. Inst. Meth. A **382**, 475 (1996).
[114] A. F. Borghesani, D. Iannuzzi, and G. Carugno, J. Phys. Condens. Matter **9**, 5057 (1999).
[115] C. G. Wahl et al., JINST **9**, P06013 (2014).
[116] P. Peiffer et al., JINST **3**, P08007 (2008).
[117] M. D'Incecco et al., IEEE Trans. Nucl. Sci. **65**, 1005 (2018).
[118] J. B. Albert et al. (The nEXO Collaboration), Phys. Rev. C **97**, 065503 (2018).
[119] D. Franco et al., JCAP **2016**, 017 (2016).
[120] C. Galbiati et al., Phys. Rev. C **71**, 055805 (2005).
[121] J. B. Albert et al. (The EXO-200 Collaboration), Nature **510**, 229 (2014).
[122] M. Agostini, G. Benato, and J. A. Detwiler, Phys. Rev. D **96**, 074 (2017).
[123] J. Zhao, L.-J. Wen, Y.-F. Wang, and J. Cao, Chin. Phys. C **41**, 053001 (2017).
[124] L. Baudis et al., JCAP **2014**, 044 (2014).
[125] E. Grace, A. Butcher, J. Monroe, and J. A. Nikkel, Nucl. Inst. Meth. A **867**, 204 (2017).